January 2016

HIGH EFFICIENCY EDGE COUPLER, NOVEL NONLINEAR OPTICAL POLYMERS WITH LARGE KERR-COEFFICIENT AND AUTOMATIC LAYOUT GENERATION IN SILICON PHOTONICS

Ben Niu
Purdue University

Graduate School Form
30 Updated 12/26/2015

PURDUE UNIVERSITY
GRADUATE SCHOOL
Thesis/Dissertation Acceptance

This is to certify that the thesis/dissertation prepared

By Ben Niu

Entitled

HIGH EFFICIENCY EDGE COUPLER, NOVEL NONLINEAR OPTICAL POLYMERS WITH LARGE KERR-COEFFICIENT AND AUTOMATIC LAYOUT GENERATION IN SILICON PHOTONICS

For the degree of Doctor of Philosophy

Is approved by the final examining committee:

Minghao Qi
Chair

Vladimir Shalaev

Xianfan Xu

Yi Xuan

To the best of my knowledge and as understood by the student in the Thesis/Dissertation Agreement, Publication Delay, and Certification Disclaimer (Graduate School Form 32), this thesis/dissertation adheres to the provisions of Purdue University's "Policy of Integrity in Research" and the use of copyright material.

Approved by Major Professor(s): Minghao Qi

Approved by: Venkataramanan Balakrishnan 12/9/2016

Head of the Departmental Graduate Program Date

HIGH EFFICIENCY EDGE COUPLER, NOVEL NONLINEAR OPTICAL POLYMERS WITH LARGE KERR-COEFFICIENT AND AUTOMATIC LAYOUT GENERATION IN SILICON PHOTONICS

A Dissertation

Submitted to the Faculty

of

Purdue University

by

Ben Niu

In Partial Fulfillment of the

Requirements for the Degree

of

Doctor of Philosophy

December 2016

Purdue University

West Lafayette, Indiana

ACKNOWLEDGMENTS

First and foremost, I would like to take this opportunity to thank my advisor, Professor Minghao Qi for letting me into this emerging and exciting field of silicon photonics. All these years of my graduate life have made me appreciate his knowledge, wisdom, personality and integrity deeply. He has always been patient and kind, even when I struggled from time to time. Also thanks to him, I got the opportunity to work in Shanghai Institute of Systems and Infomation Technology (SIMIT), Chinese Academy of Science as well as collaborate with Huawei USA.

Second, I would like to thank many of my colleagues. Professor Yi Xuan, Dr. Leo Tom Varghese and Dr. Li Fan have instructed me greatly on semiconductor process. I appreciate Kyunghun Han and Min Teng for their help in my work as well as their friendship. I am also fortunate to work with Dr. Jian Wang who has deep insight and knowledge in the field. In addition, I am thankful to have the chance to work with Justin Wirth, Sangsik Kim, Yunjo Lee and many others. I will always remember Birck Nanotechnology Center, where I spent many years as a PhD student.

Third, I will always cherish my colleagues and friends in SIMIT and Beihang University during the year I spent in China, including Professor Fuwan Gan, Professor Zheng Zheng, Dr. Jing Wang, Dr. Yufeng Jiang and Dr. Xin Zhao, just to name a few.

Finally, I want to dedicate this dissertation to my father, for his teaching and discipline in my early years laid the foundation for me to become who I am today. I am forever in debt to him.

TABLE OF CONTENTS

Page

Page

LIST OF TABLES

LIST OF FIGURES

Figure Page

ABSTRACT

Niu, Ben Ph.D., Purdue University, December 2016. High Efficiency Edge Coupler, Novel Nonlinear Optical Polymers with Large Kerr-Coefficient and Automatic Layout Generation in Silicon Photonics. Major Professor: Minghao Qi.

The potential of on-chip photonics is limited by the difficulty in coupling light from optical fibers to on-chip waveguides. Specifically, 3rd-order nonlinear on-chip photonics usually requires high optical power. Hence the first major focus of this research is to design high-efficiency edge couplers. To achieve this goal, loss mechanisms of basic inverse taper couplers are analyzed and experimentally verified. Then a cantilever-encapsulated inverse taper is demonstrated to further lower coupling loss compared to basic inverse tapers. Nonetheless, both couplers are designed to couple with lensed fibers. Hence for flat fibers with larger mode-field-diameter (MFD), a novel sub-wavelength grating based edge coupler is proposed and experimentally demonstrated to have 1.9dB/facet loss. Eventually a silicon multi-section taper with intermediate SU-8 waveguide cladding is proposed for flat fibers with even larger MFD and experimentally verified. Based on the result several suggestions are proposed for further improvement.

Since high optical power is necessary for 3rd-order nonlinear applications, silicon is not the material choice due to its intrinsic two-photon-absorption(TPA). Thus the second focus of this research is to explore a novel nonlinear optical polymer termed PolyDDMEBT. Both its linear and nonlinear optical properties are charaterized. The measurement shows that the material has a real part refractive index of 1.68 and negligible absorption in 1550nm. Also, the polymer possesses negative thermo-optical coefficient. In addition, Z-scan measurement shows large Kerr-coefficient and no

presence of TPA in this polymer. As a result, PolyDDMEBT may be useful for 3rd-order optical nonlinear applications.

The third focus of this research is regarding automatic layout generation of on-chip photonics. This tool developed by the author is proven capable of generating both simple and complex on-chip photonic layouts. And it is especially efficient in large numbers of parameter sweepings.

1. INTRODUCTION TO ON-CHIP PHOTONICS

1.1 Fundamentals of On-chip Photonics

The world of electronics has come a long way. In the beginning was vacuum tubes, bulky and power hungry. Then solid state transistors greatly reduced the size and power consumption of various electrical components. Finally since its birth in the late 1950s, integrated circuits (IC) has squeezed the entire electronic system onto chip platform. Consequently, microelectronics has grown exponentially in integration and unit cost has drastically declined, following Moore's Law [1]. Likewise, optics/photonics is evolving with the similar trend. For instance, optics in the 1950s was about light generation from bulky gas laser sources, reflection by mirrors and focus by lenses. Then with the advent of optical fibers, optical components greatly reduced in size such as fiber lasers as light sources. Now motivated by the awesome success of the microelectronics, researchers are pushing to integrated various photonic components on-chip, including laser, modulator, waveguide, photo-diode etc.

Several material platforms have been utilized for on-chip photonics. For example, arrayed-waveguide-grating(AWG) has been demonstrated in silica planar lightwave circuits (PIC) [2–4], where silica waveguides with higher refractive index are buried among silica cladding with lower index. Although it does provide optical confinement, the limited index difference causes large device footprint such as large waveguide bends. For instance, AWGs based on silica platform can be in the range of millimeters or even more. In order to reduce device size and increase integration, on-chip silicon photonics (SiPh) [5–7] has emerged as an attractive solution, where high-index silicon waveguide are buried in low-index silica cladding. Due to the large refractive index contrast, SiPh enables strong optical mode confinement, thus greatly reducing the device footprint. For instance, the size of AWGs based on silicon waveguides can

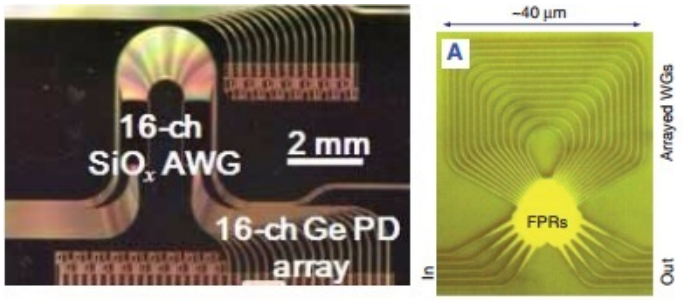

Fig. 1.1.: . The size comparison between a silica-waveguide-based AWG(left) [4] versus a silicon-waveguide-based AWG(right) [9]

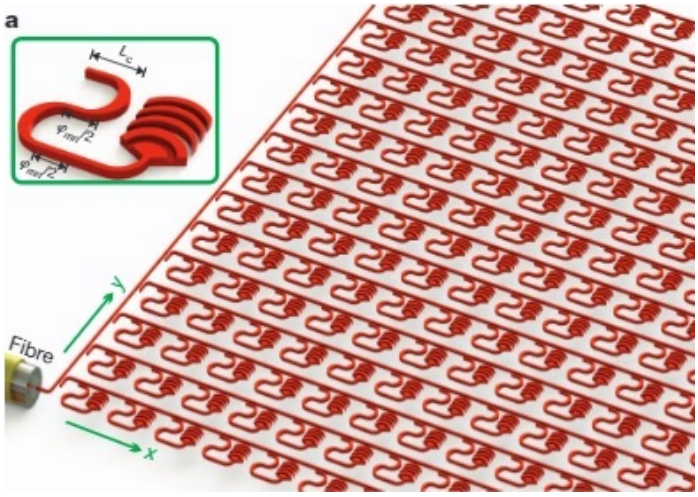

Fig. 1.2.: . Illustration of optical phase array [10]

be reduced to tens of micrometers [8, 9]. Fig.1.1 shows the size comparison between silica-based and silicon-based AWGs.

1.2 On-Chip Photonics By Academia, Industry and Governments

A number of academic institutions have devoted a great deal of research into on-chip photonics. For instance, a MIT group demonstrated on-chip optical phased array with 4096 optical components [10]. A group at Berkeley has demonstrated nanolasers

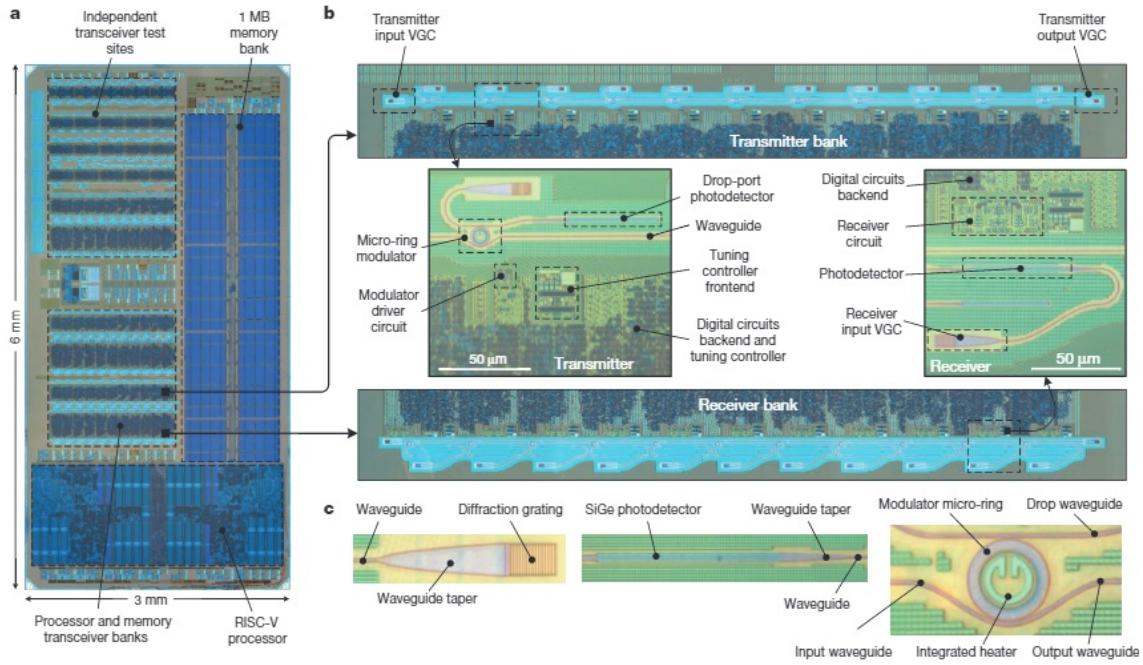

Fig. 1.3.: . Optical photo of a microprocessor communicating directly in light [10]

grown on silicon [11]. Moreover, another group at Cornell has demonstrated one of the first micro-ring based silicon modulator [12],etc just to name a few.

Beyond academia, many industrial companies have also invested in the field. For instance, IBM is developing cost efficient packaging method for on-chip photonics [13]. Intel has demonstrated 100G CWDM (Coarse Wavelength-Division Multiplexing) optical transceiver [14]. Others such as Cisco, Huawei, Google and Facebook etc are actively involved in this field. Besides these well-established industrial giants, a number of new companies specializing in SiPh have also emerged, including Infinera, Luxtera, Kotura, Caliopa, Aurrion etc. Due to its importance in national security, various governments have shown strong support towards on-chip photonics. Specifically, United States government has pledged to invest 100 million USD in a public-private partnership termed "The American Institute for Manufacturing Integrated Photonics (AIM Photonics)" [15], aiming to become the leading nation in the field. Similarly, European Union has its own version called "ICS-STREAMS" project [16], where 50 million USD is promised in the research of silicon photonics. Likewise, China has

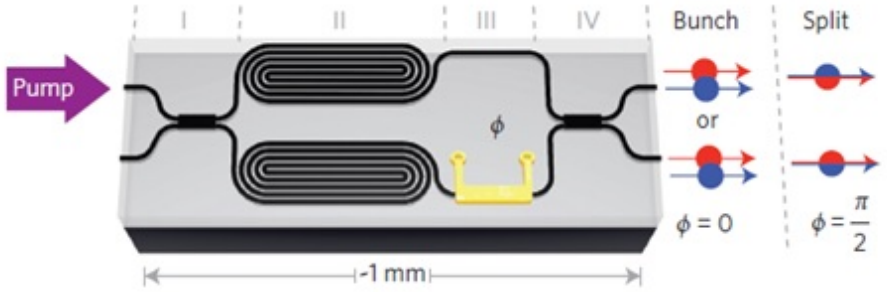

Fig. 1.4.: . Illustration of a silicon photonic chip for quantum photonics [24]

also proposed 37 million USD funding in "Large-Scale Integrated Photonics Chips" project.

The academic research universities, industry as well as national labs often collaborate together to attempt major technological breakthroughs. For instance, researchers from UC Berkeley, MIT, University of Colorado, together with those from IBM and National Institute for Standards and Technology (NIST) have successfully demonstrated for the first time a single-chip microprocessor that communicate directly with light [17], which integrates the microelectronics and SiPh together onto the same chip. The SiPh part contains numerous grating couplers, micro-ring modulators, waveguides, photodiodes etc, as show in Fig.1.3.

1.3 Explorations of New Science with On-chip Photonics

On-chip photonics has provided a potent platform for exploring new science and future technologies. For instance, it has been used to study light-matter interactions [18, 19], high-Q(quality factor) micro-resonators based optical frequency combs [20–22], compact platform for quantum photonics [23–25] as well as optical trapping [26], just to name a few. An illustration of a silicon photonic chip platform for quantum photonics is shown in Fig.1.4.

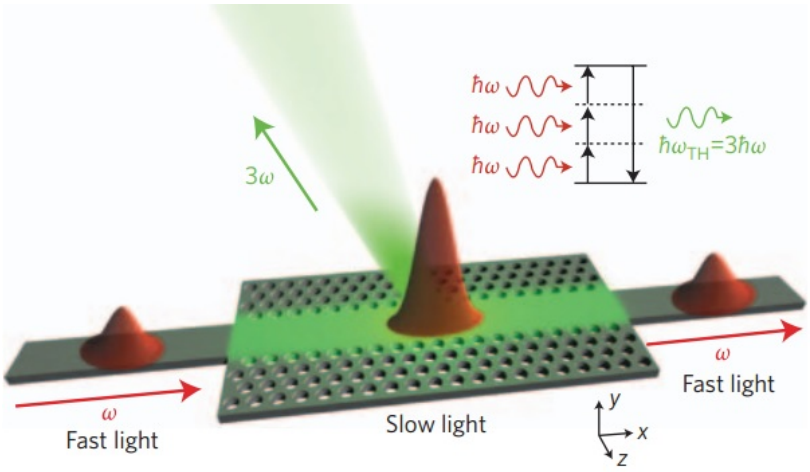

Fig. 1.5.: . Illustration of THG of green light in a silicon slow-light waveguide [29]

1.4 Challenges of Nonlinear On-Chip Photonics

Nonlinear Optics [27] is an important branch of optics and it usually requires high optical power and large material optical nonlinearity to generate observable nonlinear signals. Efforts have been made to generate nonlinear optical phenomena using on-chip platform [28]. For instance, Fig.1.5 shows third-harmonic generation(THG) of green light in a silicon slow-light waveguide [29]. However, there are two major challenges with on-chip nonlinear photonics. First, coupling between optical fibers and on-chip devices usually causes significant insertion loss. Unlike fiber-based EDFA, on-chip optical signal amplification is quite difficult. Second, most of the usual CMOS-compatible dielectrics including silicon possesses small 3rd-order nonlinearity, which further increases the power demand. Therefore, this work focuses on these two areas: reducing fiber-to-chip coupling loss and explore new material with large 3rd-order optical nonlinearity.

2. HIGH EFFICIENCY FIBER-TO-CHIP EDGE COUPLERS

2.1 Overview of Fiber-to-Chip Coupling

In SiPh, optical fibers are generally used to couple light into and out of on-chip integrated photonic devices. However, modes supported in optical fibers have drastically larger mode file diameter(MFD) than those in on-chip waveguides, as shown in Fig. 2.1. This mismatch causes significant coupling loss between optical fiber and chip.

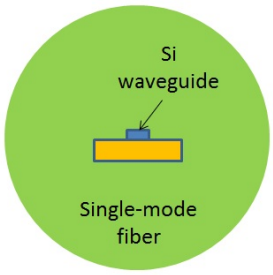

Fig. 2.1.: Mode mismatch between optical fiber core and on-chip waveguide

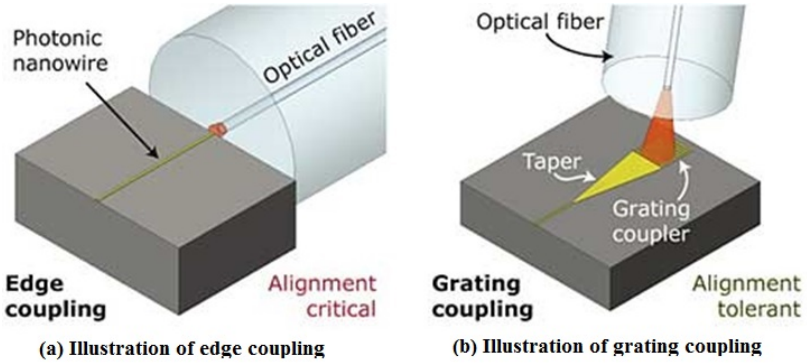

Fig. 2.2.: Illustration of edge coupling and grating coupling [30]

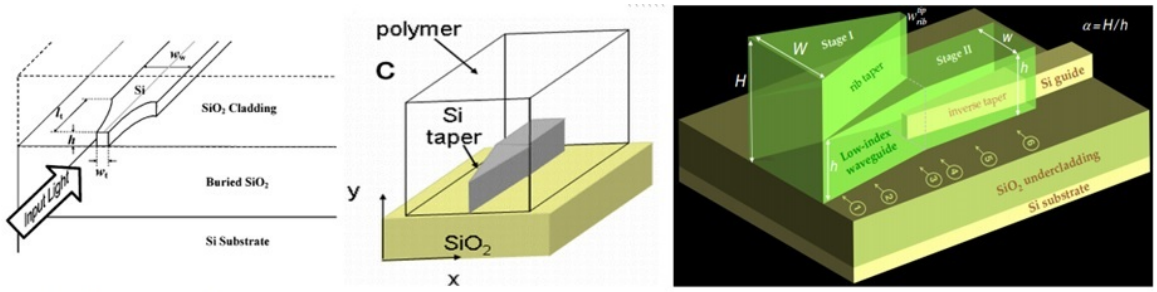

(a) Illustration of a basic inverse taper

(b) Illustration of a basic inverse taper cladded with a polymer waveguide

(c) Illustration of a basic inverse taper with two-stage low-index cladding

Fig. 2.3.: Brief historical development of edge couplers

To reduce this undesirable loss, one of the solutions is to introduce fiber-to-chip couplers. Currently there are two main categories: edge couplers and grating couplers, shown in Fig.2.2. Each has its own advantages and shortcomings. For example, edge coupling possesses broadband transmission but suffers from limited alignment tolerance. Grating coupling enables dense device integration on chip and is more alignment tolerant. Yet it suffers from limited bandwidth.

Since the high speed applications such as wavelength-division multiplexing (WDM) require certain bandwidth, industry in general favors edge couplers. In addition, industry prefers cheap flat optical fibers to relatively expensive lensed fibers used in the research labs. Hence the ultimate goal is to couple light from flat fibers into and out of edge couplers with high efficiency.

The brief historical development of edge couplers is shown in Fig.2.3. The first attempt to achieve high efficiency edge coupling is accomplished by using basic inverse tapers as the interface between waveguides and optical fibers [31]. The fiber mode first is coupled to the taper tip mode and then is gradually converted to waveguide mode. The taper tip supports a larger fundamental mode than silicon waveguide, hence mitigating the mode mismatch and reducing coupling loss. However, it relies on coupling with 2.5μm-MFD lensed fibers and suffers large coupling loss of 3.3dB/facet. Then, an intermediate cladding waveguide is proposed on top of the inverse taper [32]. This additional stage supports a much larger fundamental mode and enables the

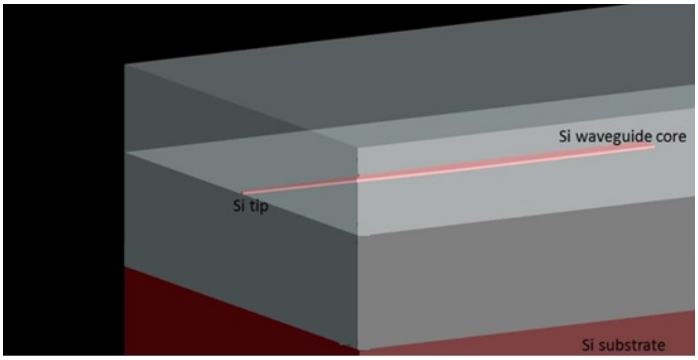

Fig. 2.4.: Illustration of the structure of an inverse taper

fiber mode to be better coupled into the cladding waveguide. Nonetheless, it is still designed for lensed fibers. Later, a new multi-stage design is proposed [33], which adds a rib taper on top of the intermediate cladding layer. This design can couple with flat optical fiber. The added benefit is that the rib taper compresses the flat fiber mode before feeding it into the lower stage, thus further improving efficiency. However, its fabrication poses a serious challenge. So far the performance of edge couplers fabricated with standard CMOS process coupling to flat fibers is not up to industry demand. Hence there is a need to design a high coupling efficiency edge coupler for flat fibers.

2.2 Inverse Taper Power Loss Mechanism

In order to increase coupling efficiency, the loss mechanism needs to be understood. In a typical SOI inverse taper shown in Fig.2.4, several competing factors affect its power coupling efficiency.

1. A = power coupled to the guided mode of the taper tip
2. B = power coupled to expanded taper along propagation
3. C = mode transition loss (scales down with taper length)
4. D = scattering loss due to roughness (scales up with taper length)

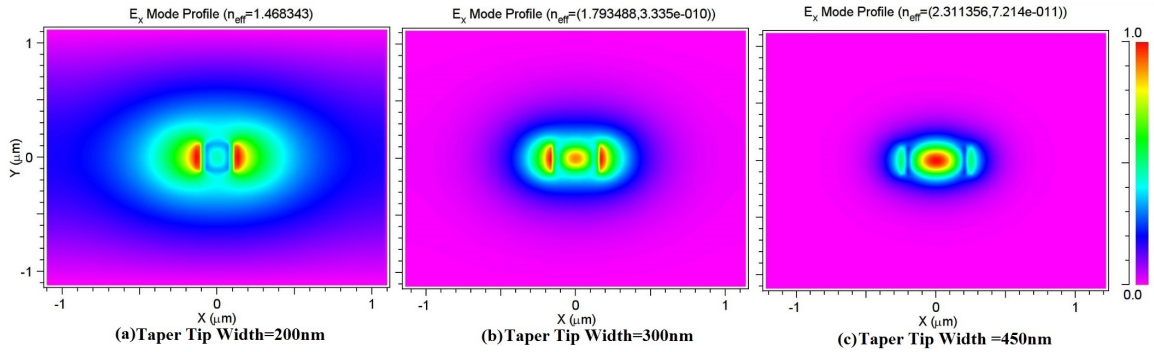

Fig. 2.5.: Fundamental TE mode profiles of inverse taper tips with different tip widths

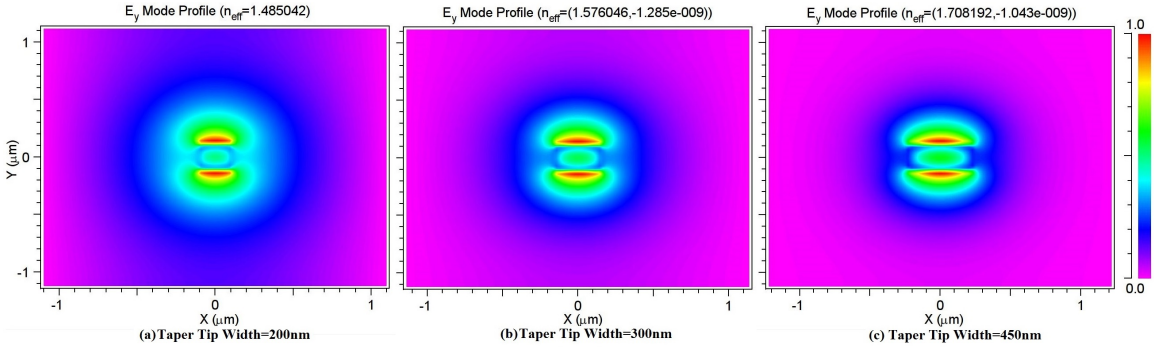

Fig. 2.6.: Fundamental TM mode profiles of inverse taper tips with different tip widths

Total power coupling = A + B - C - D

2.2.1 Power Coupled to the Guided Mode of the Taper Tip(A)

The power coupled to the guided mode of the taper tip depends on the mode overlapping between fiber mode and taper tip mode. Fig.2.5 shows the simulated fundamental TE modes of a taper tip with different widths. The height of the taper tip is fixed at 220nm, equal to the top silicon layer thickness of usual SOI wafers.

Ideally a good mode-matching requires the coupled mode to be of similar shape, size and intensity distribution with input fiber mode, which is Gaussian mode with

a circular cross-section and maximum intensity in the center. As shown in Fig.2.5, if the taper tip is very narrow, its guided fundamental TE mode is very elliptically-shaped. Hence mode-matching is poor and the power coupled into the taper is small. On the other hand, if the taper tip is very wide, its guided fundamental TE mode is well confined in the center of the taper. Hence its mode size is drastic smaller than that of input fiber mode and the power coupled into the taper is small. Therefore, an optimum taper tip width exists to maximize mode matching and power coupling between the fiber mode and the taper tip mode. In other words, this optimum taper tip should support a fundamental mode that has the maximum mode-matching with the input fiber mode. Likewise, TM modes exhibit the same trend, as shown in Fig.2.6.

2.2.2 Power Coupled to the Expanded Taper(B) and Mode Transition Loss(C)

Since not all of the input fiber power can be coupled into the taper tip, part of the input power propagates outside the taper. Some of this power close to the taper surface may still be coupled into the taper as it expands in width. To study this effect, beam propagation method(BPM) simulation is performed on inverse tapers with difference lengths (25μm, 50μm and 100μm) and tip widths (40nm and 200nm). Fig.2.7 shows the power transmission of these six inverse tapers with different geometry.

The conventional wisdom says that in order to reduce mode transition loss, the taper needs to be long enough. The simulation results show that at 200nm tip width, longer taper does lead to higher transmission, confirming the conventional wisdom. However, at 40nm tip width the trend is reversed as shorter taper has higher transmission.

With the same taper tip width and end width (equal to waveguide width), the shorter the taper, the faster it expands in width. This width expansion is even more rapid with small tip width and short taper length. The more rapidly-expanding taper

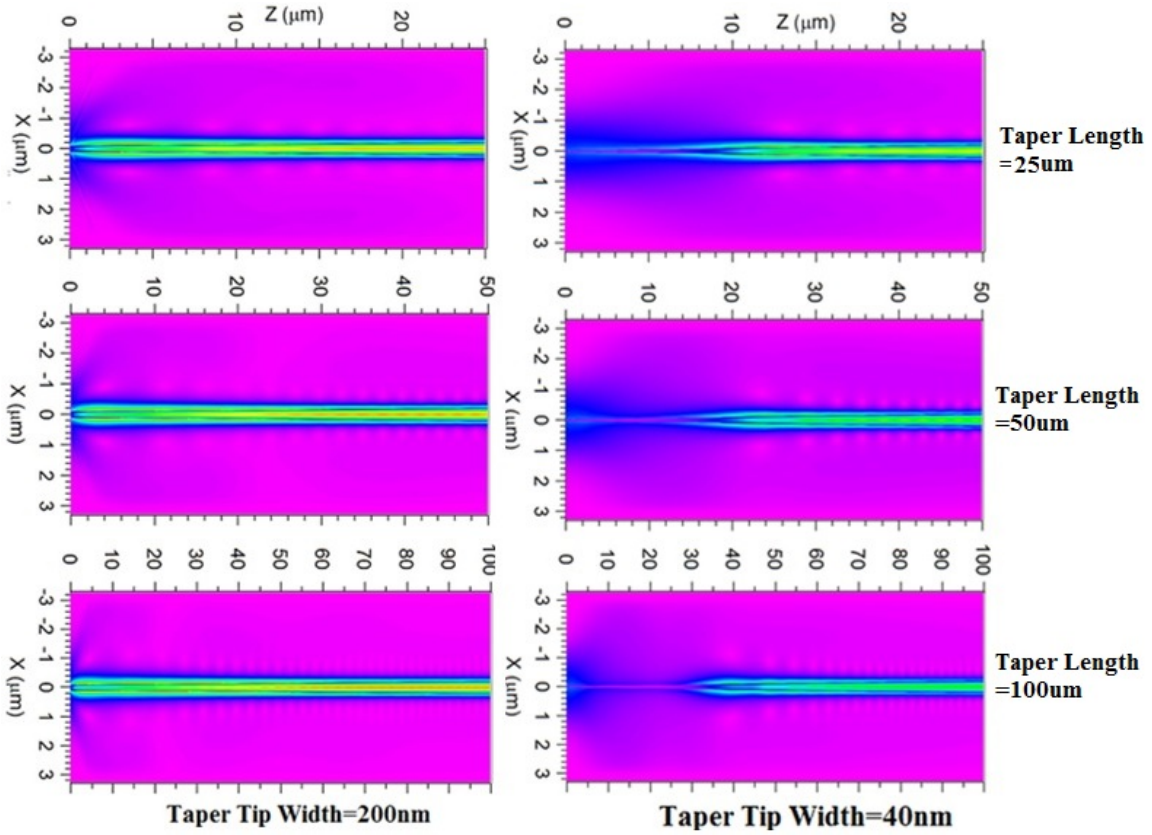

Fig. 2.7.: Transmission of inverse tapers with same tip width but different lengths

absorbs more power adjacent to the taper sidewall. Thus shorter taper with small tip width exhibits higher coupling efficiency than longer taper with the same tip width. On the other hand, with large tip width, the width expansion of the taper is much more gradual and the difference in the power adjecent to the tape sidewall absorbed into the taper is negligible.

As taper expands or shrinks in its width, its cross -section changes and its supported fundamental modes changes as a result. Therefore, when optical beam travels in the taper, mode conversion takes place. The loss associated with this process is termed mode transition loss. The longer the taper, the slower its cross-section changes and the less mode transition loss [34] [35] it has.

Combining the effects of taper width expansion and mode transition loss, shorter taper with small tip width exhibits higher coupling efficiency than longer taper with

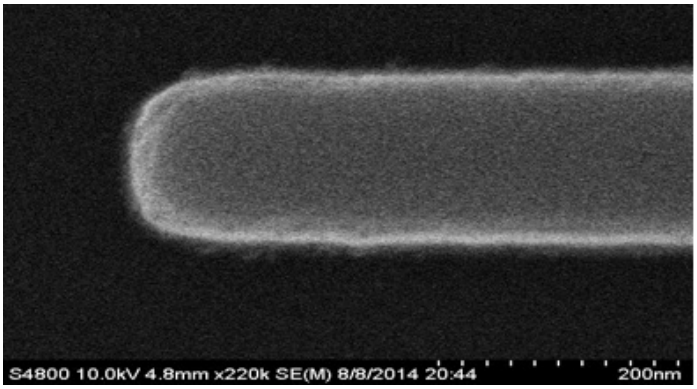

Fig. 2.8.: Scanning-Electron-Microscopic (SEM) photo showing surface roughness of an inverse taper

the same small tip width, while longer taper with large tip width exhibits higher coupling efficiency than shorter taper with the same large tip width.

2.2.3 Scattering loss due to Surface Roughness(D)

The aforementioned analysis does not take into account surface roughness of the inverse taper. Yet it is inevitable in fabrication, as shown in Fig.2.8. Surface roughness acts like tiny scattering and radiation centers. Optical fields passing through these centers are scattered or radiated away, causing additional loss. Scattering loss goes up with increasing level of roughness and the taper length.

2.3 Fabrication of Waveguides, Edge Couplers and U-shaped Grooves

The fabrication process of edge couplers with U-shaped grooves(U-grooves) is shown in Fig.2.9 and contains several steps:

1. Starting with silicon-on-insulator(SOI) wafer with 220nm top silicon. Cut the wafer into appropriate-sized sample using diamond pen and clean the sample surface with piranha solution(hydrogen peroxide:98% sulfuric acid=1:3).

2. Apply e-beam resist hydrogen silsesquioxane (HSQ) on top and write the patterns of waveguides and edge couplers to the HSQ layer with a dose of $2500\mu C/cm^2$. Then develop HSQ in tetramethylammonium hydroxide (TMAH).

3. Dry etch the top silicon layer using exposed HSQ as a mask with chlorine based gas to transfer the pattern from HSQ layer to the silicon layer. Then remove HSQ with diluted hydrogen fluoride(HF) solution.

4. Clad the exposed top silicon layer with 2um thick low-temperature-oxide(LTO silicon dioxide) at 400C.

5. Anneal the sample at 900C in nitrogen gas for 1 hour.

6. Apply SU-8 e-beam resist on top of the LTO cladding and write the U-groove patterns to the SU-8 layer with a dose of $5\mu C/cm^2$. Then develop SU-8 in SU-8 developer. Deep dry etch 65 to $70\mu m$ into the substrate to form U-grooves. Then remove the remaining SU-8.

2.4 Measurement of Coupling Efficiency of Inverse Taper

2.4.1 The Effect of Ugrooves

Lensed fibers with $2.5\mu m$ mode-field-diameter(MFD) are used to measure basic inverse tapers. Direct coupling between lensed fiber and inverse taper can be challenging, since the coupling is extremely sensitive to misalignment and fiber tip vibration, especially in high power measurement. Hence U-grooves are etched on the chip to assist the coupling. During the actual measurement, lensed fibers sit tightly in the U-grooves, reducing much of the undesirable tip vibration along with coupling time, as shown in Fig2.10.

U-grooves are especially important in high power coupling, as shown in Fig2.11. High power increases the lensed fiber tip vibration, making direct coupling practically impossible. However, with the help of U-grooves, the measured output power

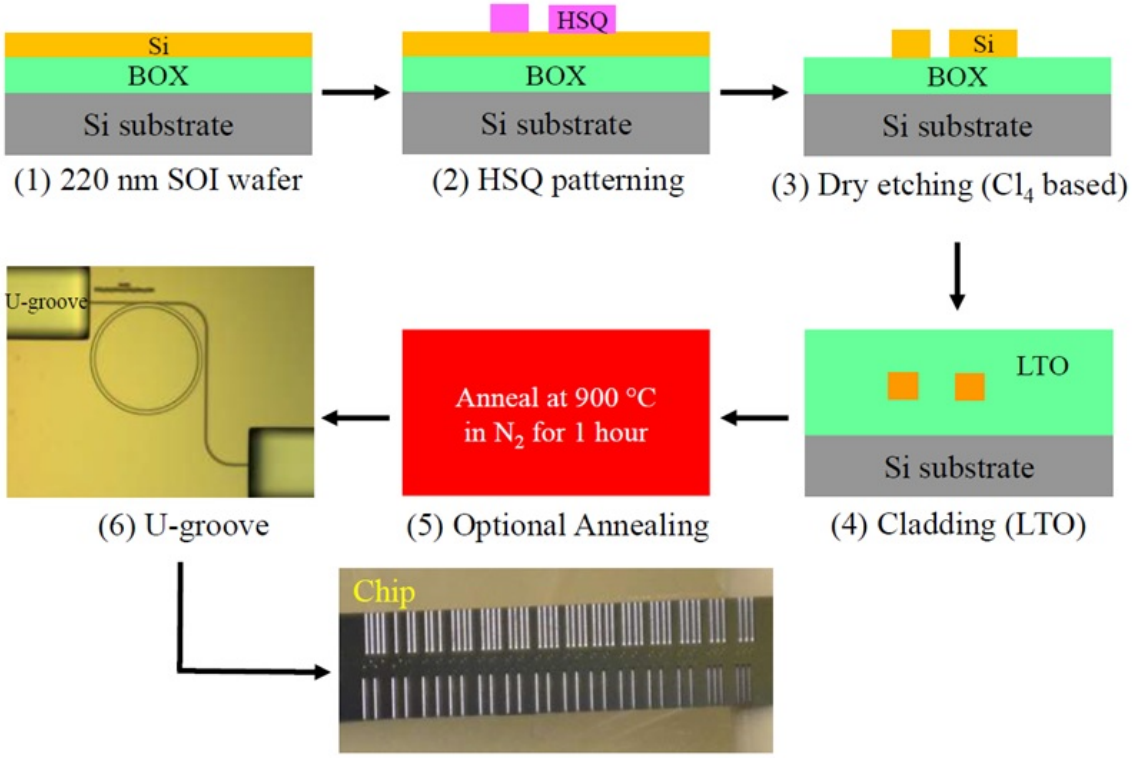

Fig. 2.9.: The fabrication process of edge couplers with U-shaped grooves

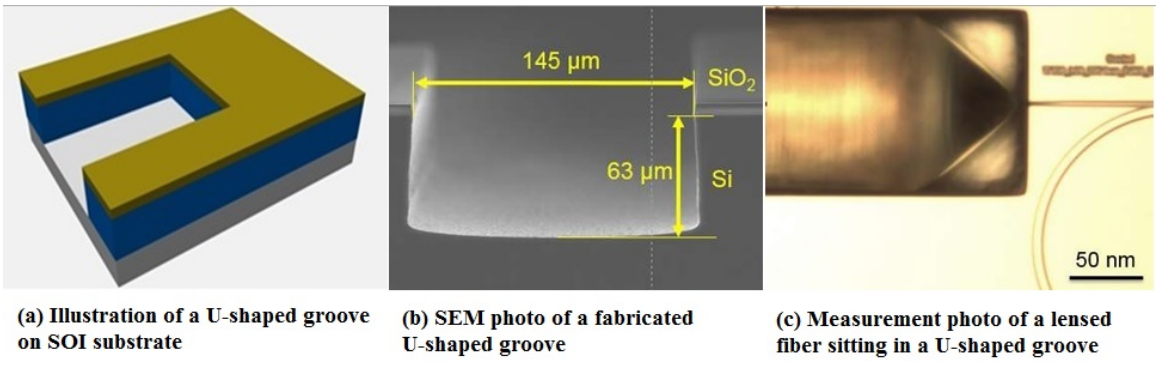

Fig. 2.10.: Schematic and SEM photo of a U-shaped groove as well as optical photo of a lense fiber sitting in one during measurement

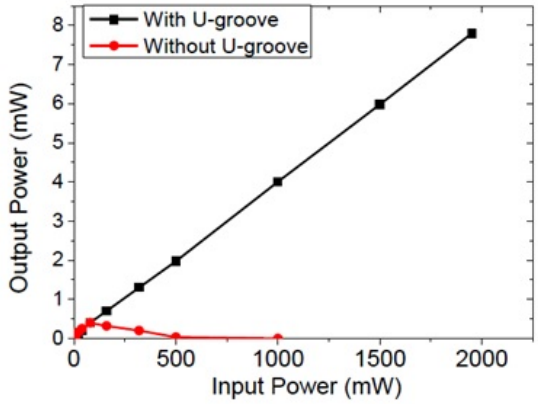

Fig. 2.11.: Measured output power as a function of input power with and without U-shaped grooves

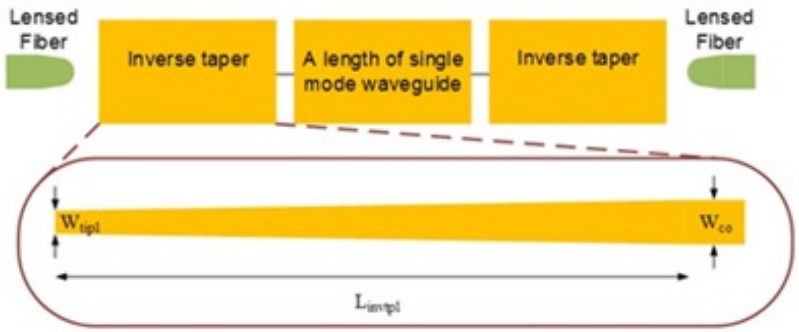

Fig. 2.12.: Measurement setup of inverse tapers

is proportional to the input power. This indicates the coupling loss is constant, independent of input power. This proves the lensed fibers sitting in the U-grooves are stable even with high power.

2.4.2 Measurement Setup

The measurement setup is shown in Fig2.12. Two inverse tapers are usually connected to the two ends of a waveguide. The measured total fiber-to-fiber insertion loss contains both taper coupling loss and waveguide propagation loss. In order to separate them, spiral waveguides with the same inverse tapers but different lengths

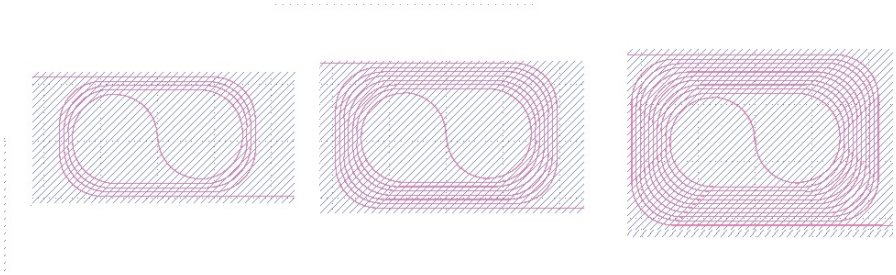

Fig. 2.13.: Spiral waveguides with different lengths

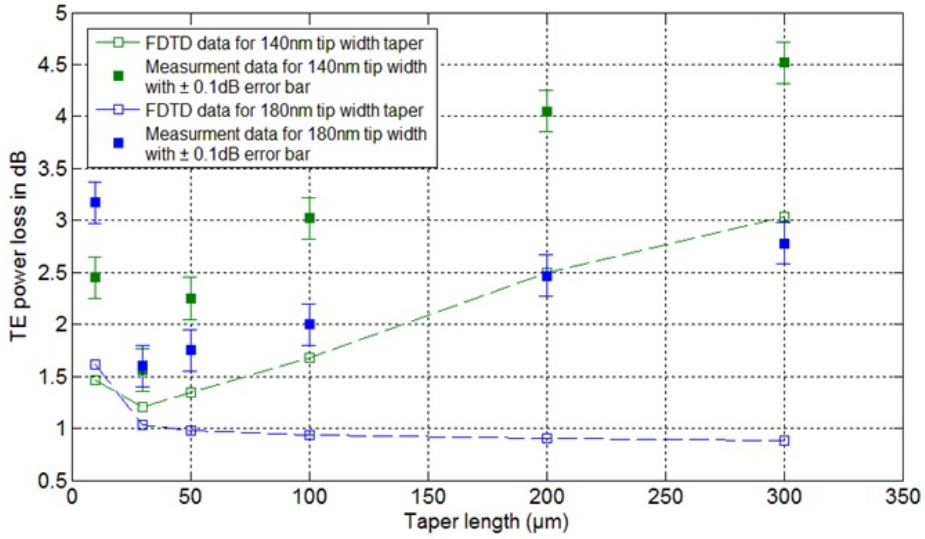

Fig. 2.14.: FDTD simulation without surface roughness compared to experimental results

are measured, as shown in Fig.2.13. This method enables taper coupling loss and waveguide propagation loss to be extracted separately.

2.4.3 Measurement Result Analysis

FDTD simulation is performed on inverse tapers with tip widths of 140nm and 180nm respectively without surface roughness and the result is plotted in dashed lines in Fig.2.14. The results show that without surface roughness, at 140nm tip width, 30μm taper length has the lowest coupling loss. For 180nm tip width though,

longer taper exhibits less loss. This confirms the aforementioned loss mechanisms of basic inverse tapers: with small tip width(140nm), the competing factors of A, B and C result in an optimum taper length(30μm). However, for large tip width(180nm), longer taper exhibits less loss because process C dominates.

The measurement data of real devices with surface roughness plotted in dots shows different trend. In both tip widths, the measured loss is significantly higher that simulation data. Besides,for 180nm tip width, the measurement data also shows 30μm taper length has lowest coupling loss, which is in contrast with the simulation data. This can also be explained by the aforementioned loss mechanisms of basic inverse tapers: in reality both A, B, C and D factors play a role with the presence of surface roughness. Thus in longer taper length surface roughness caused loss goes up.

2.5 Cantilever-Encapsulated Inverse Taper

The loss analysis on inverse tapers shows that the mode mismatch between fiber mode and waveguide mode is an important loss factor. One way to mitigate this loss is to use a cantilever-encapsulated inverse taper (cantilever taper for short). The cantilever structure in cladding material acts as a low-index waveguide with larger fundamental mode, thus reducing the mode mismatch. Cantilever taper has been demonstrated to achieve less than 1dB/facet loss [36]. However, these results are achieved with with tapered fibers instead of common lensed fibers in labs, as shown in Fig.2.15.

In Fig.2.16, cantilever taper capable of coupling with 2.5μm-MFD lensed fiber is fabricated and the measurement result is shown in Fig2.17. With normal lensed fiber, the cantilever taper has minimum loss of 0.9dB/facet at 1550nm in one polarization and 1.3dB/facet in the other polarization. Both results are broadband. Hence the cantilever taper does have higher coupling efficiency than basic inverse taper.

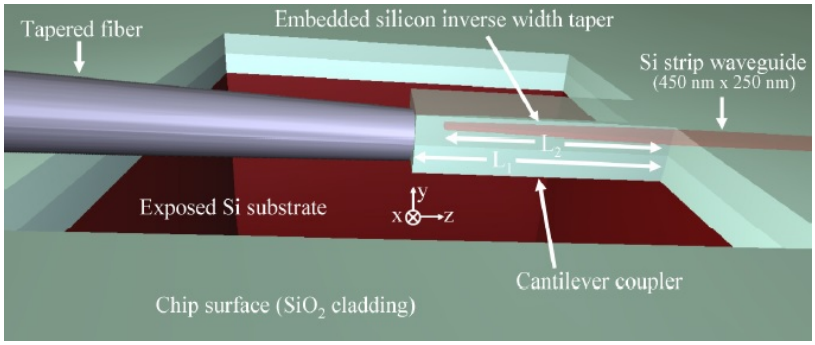

Fig. 2.15.: Illustration of a cantilever taper coupling with a tapered fiber [36]

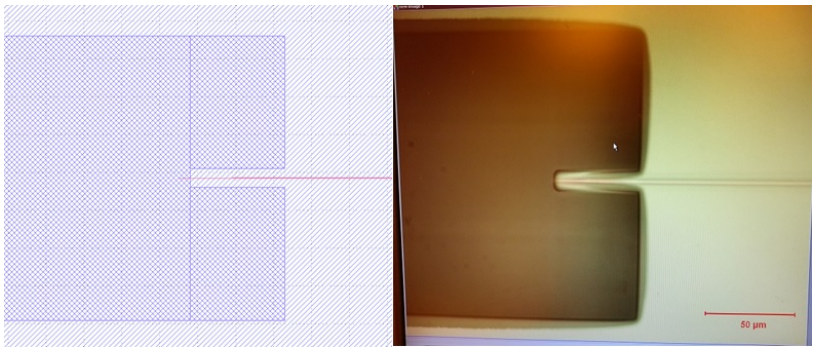

Fig. 2.16.: The design and photo of a fabricated cantilever taper

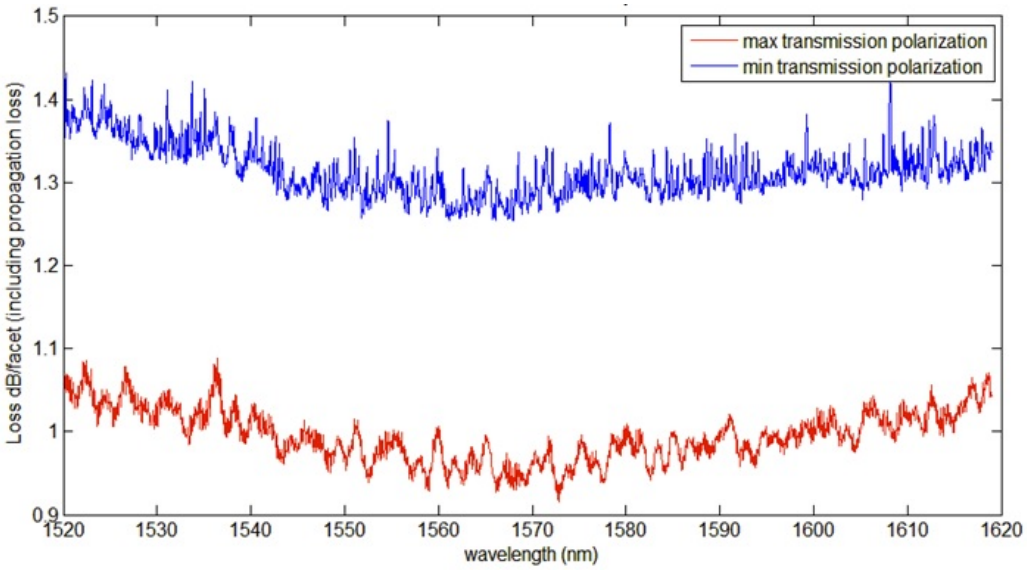

Fig. 2.17.: The measured loss of a cantilever taper

The advantages of cantilever tapers include using the buried oxide(BOX) and upper-cladding to form a low-index waveguide so the deposition of additional material is not required. Also, it does not add to the process steps used to fabricate basic inverse tapers with U-grooves since the cantilever can be formed during the etching of U-grooves by undercutting the cantilever bottom. Nonetheless, it does suffer from several disadvantages. First, the height of the cantilever is limited by the total thickness of the BOX and upper-cladding and therefore not freely adjustable. Second, the stress in the cantilever structure may bend it out of horizontal plane, increasing the difficulty in fiber coupling. Third, the cantilever is susceptible to mechanical vibration and damage, making it less reliable in repetitive measurement. Fourth, it is still designed for lensed fibers, not flat fibers with larger MFD.

2.6 Meta-Trident Edge Coupler

2.6.1 Trident Edge Coupler

Another way to increase the fundamental mode size on edge coupler tip is to use a trident-shaped coupler (trident taper in short) [37]. As shown in Fig.2.18, the trident taper has a distinct three-branch structure. The outer two branches start from the coupling edge and gradually increase in width. After certain length, their width stops increasing and at the same position a third center branch emerges. The outer two branches maintain their width for certain length but eventually shrink in width and taper out. Meanwhile, the center branch continues to increase in its width until it connects to a waveguide, resembling a basic inverse taper. This structure functions in the following way: on the coupling edge, the two outer taper tips support a larger fundamental mode, thus reducing mode mismatch with input fiber mode. Fig.2.19 shows the fundamental TE and TM modes of the trident taper with taper tip width of 200nm each. It shows a much larger mode profile than that of single tip in the basic inverse taper case. As light propagates, the outer two branches increase in width thus the fundamental mode increases in effective index and shrink in size. More

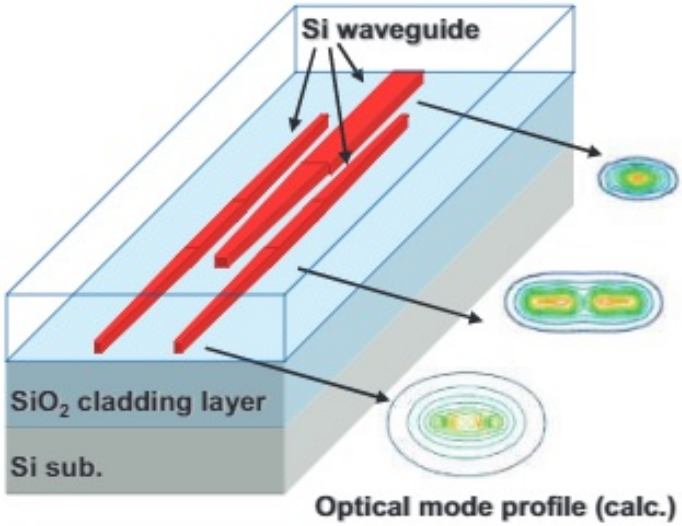

Fig. 2.18.: The structure of a trident taper [37].

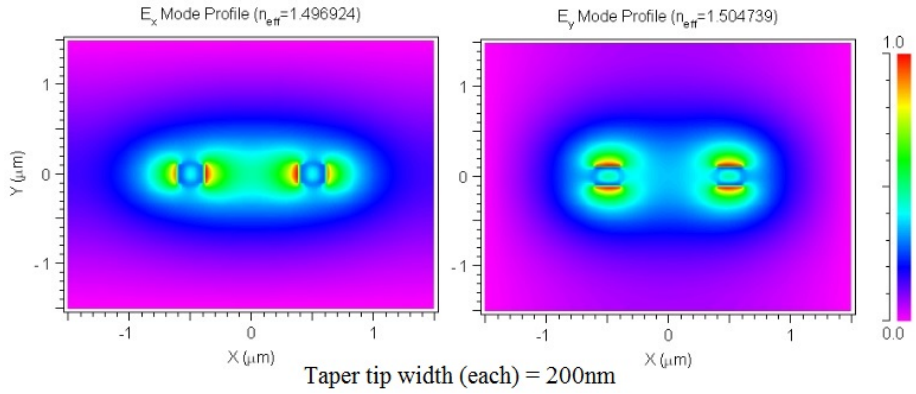

Fig. 2.19.: The fundamental TE and TM mode of trident taper tip

and more mode is gradually absorbed into the silicon part. When the center branch emerges, the fundamental mode is further confined into silicon until it evolves into the strongly confined waveguide fundamental mode. Compared to basic inverse tapers, the trident structure enjoys several advantages. First, the larger fundamental mode size at the dual-tip mitigates mode mismatch. Second, it requires the same fabrication steps with basic inverse taper. Nonetheless, it still suffers from relatively high loss at 2.3dB/facet.

Fig. 2.20.: The structure of a Subwavelength Grating Waveguide (SGW) Taper [38]

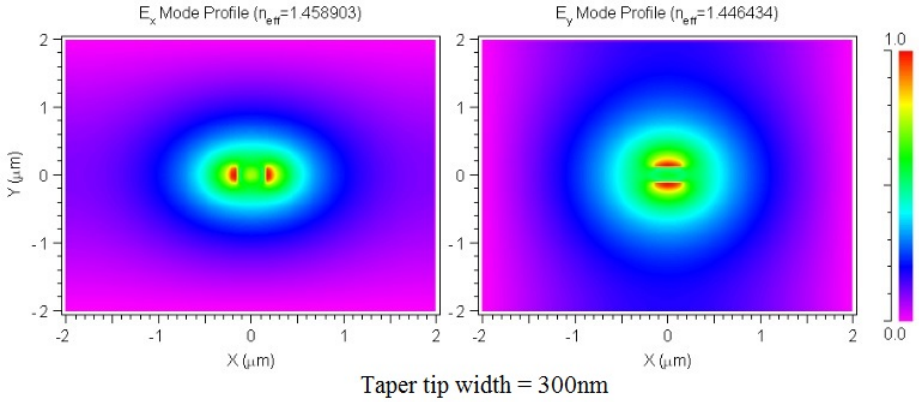

Fig. 2.21.: The fundamental TE and TM mode of subwavelength grating taper

2.6.2 Subwavelength Grating Waveguide Edge Coupler

The concept behind inverse tapers and trident tapers is to alter the effective refractive index from fiber/cladding(silica) to waveguide (silicon) gradually. Hence theoretically the taper tip width should start from zero. Yet in reality due to the limit of fabrication, the tip width has a lower limit, thus preventing the further tuning down of the effective index. Recently a new method termed subwavelength grating waveguide(SGW) coupler is proposed to overcome this hurdle [38]. As shown in Fig.reffig:EdgCup-Subwavelength-Grating, the SWG structure is composed of a series of gratings. Initially these gratings have small width. Gradually they expand in width. At certain length, an additional inverse taper emerges from the center until the entire structure connects with a waveguide. All these delicate structural changes are to guarantee gradual modification of effective refractive index. In other words, SWG tapers are capable of altering effective refractive index of the fundamental mode

much more gradually than basic inverse tapers, thus reducing coupling loss. Fig.2.21 shows the fundamental TE and TM modes of a 300nm-wide SWG taper tip, which are much larger than those of the single tip in the basic inverse taper.

SWG tapers also enjoy the benefit of only one lithography step, same with basic inverse tapers and trident tapers. However, these SWG tapers are still designed to couple with lensed fibers with 2um MFD or polarization maintaining fibers with 3μm MFD. Thus, there is still a need to design an edge coupler that does not increase fabrication steps yet can couple with flat fibers with larger MFD.

2.6.3 Meta-Trident Edge Coupler

A new edge coupler combining the advantages of both trident and SGW couplers is proposed in this work, termed meta- trident edge coupler. There are two types and their structures are shown in Fig.2.22. They both have three branches, similar to the trident taper. However, instead of continuous taper the entire outer two branches are composed of SWG structures. Additionally, one of them has the beginning of the center branch also composed of SWG structures. Fig.2.23 shows the fundamental TE and TM modes of meta-trident taper with taper tip width of 200nm each. Compared to the results shown in Fig.2.19, the fundamental mode of the meta-trident tapers are not only large in size but also much closer to a circular shape. Therefore, it enjoys higher coupling efficiency. Rigorous 3D FDTD simulation is usually required to simulate the performance of SWG related structures. However, in this case, an approximation method can be used for faster calculation. SWG with 50% duty cycle can be equated as a continuous structure with the average index between the low-index cladding and high-index waveguide. Then the entire structure can be simulated using less resource- intensive method such as beam-propagation method or eigenmode-expansion method. Fig.2.24 shows the transmission of meta-trident edge coupler without center buffer using this approximation method. The one with center buffer can be simulated in the same way.

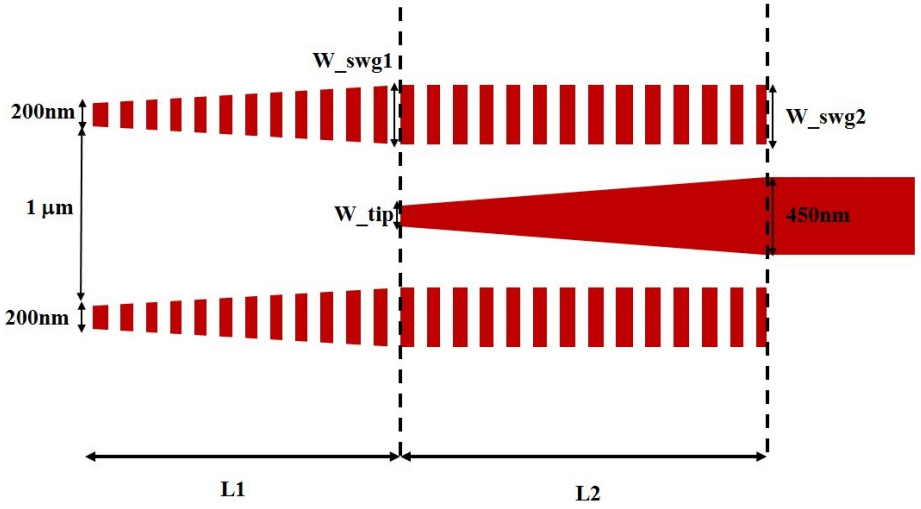

(a) Illustration of a meta-trident taper without center SWG buffer

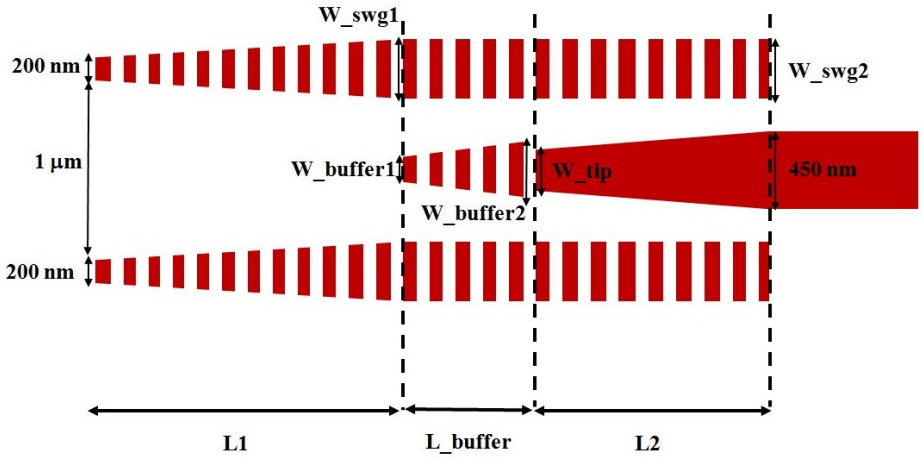

(b) Illustration of a meta-trident taper with center SWG buffer

Fig. 2.22.: Illustration of meta-trident edge couplers without and with center SWG buffer

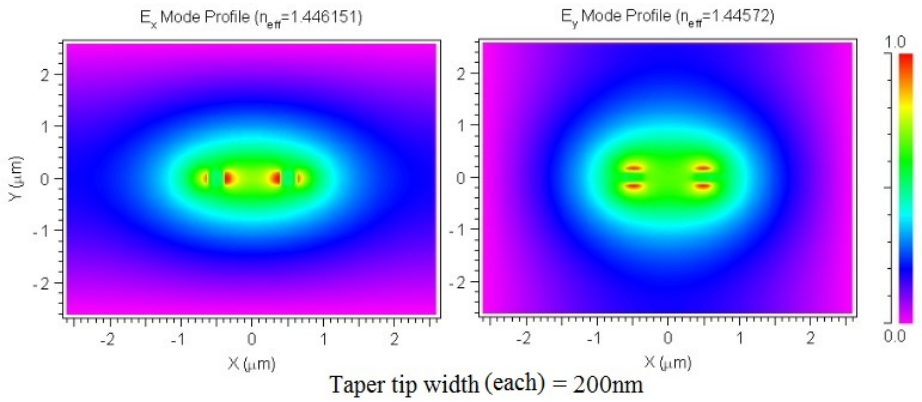

Fig. 2.23.: The fundamental TE and TM mode of meta-trident edge coupler

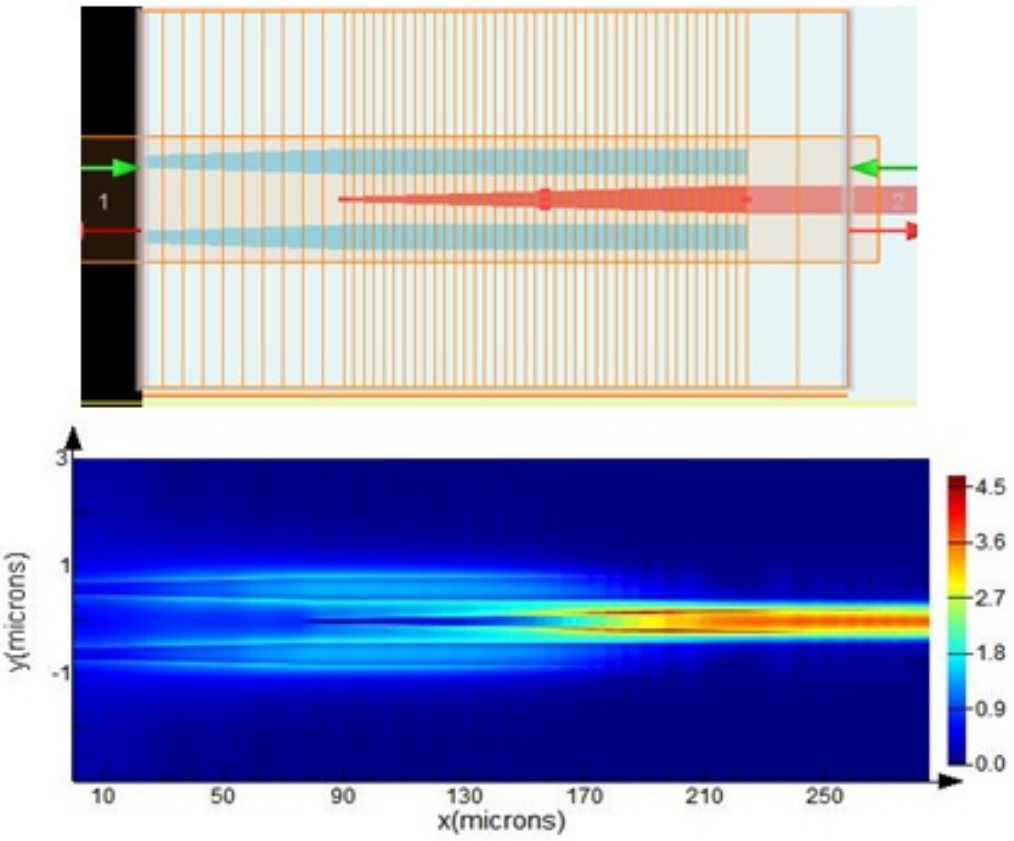

Fig. 2.24.: Simulation of the performance of meta-trident edge coupler

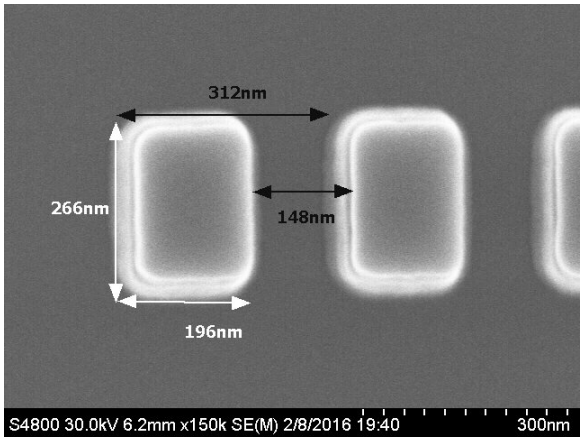

Fig. 2.25.: SEM photo of fabricated subwavelength grating

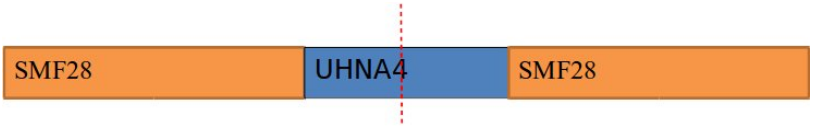

Fig. 2.26.: Illustration of a high-numerical-aperture(UHNA4) fiber spliced with single-mode fibers (SMF)

Meta-trident tapers are fabricated via almost the same process steps with basic inverse tapers except for the low-temperature-oxide(LTO). Due to the small gap size in the SWG structure, LTO may not fully fill up the gap, leaving air bubbles inside. This is highly undesirable as air bubbles can significantly alter the effective refractive index and degrade meta-trident taper coupling efficiency. Instead, 300nm thick HSQ is spun onto the surface and the liquid HSQ fully fills the gap. Then the sample is annealed in high temperature to convert HSQ into silicon dioxide. Afterwards LTO is deposited to form the upper-cladding. Fig.2.25 is a SEM photo of a fabricated SWG structure. High-numerical-aperture fiber with 4μm MFD(UHNA4) fibers are used to couple with meta-trident couplers. They need to be spliced with common single-mode fiber (SMF28) with 10μm MFD. The sudden change in the core diameter inevitably causes additional loss in the fiber splicing position, which needs to be measured. To characterize fiber coupling loss, first measure the output power without any UHNA

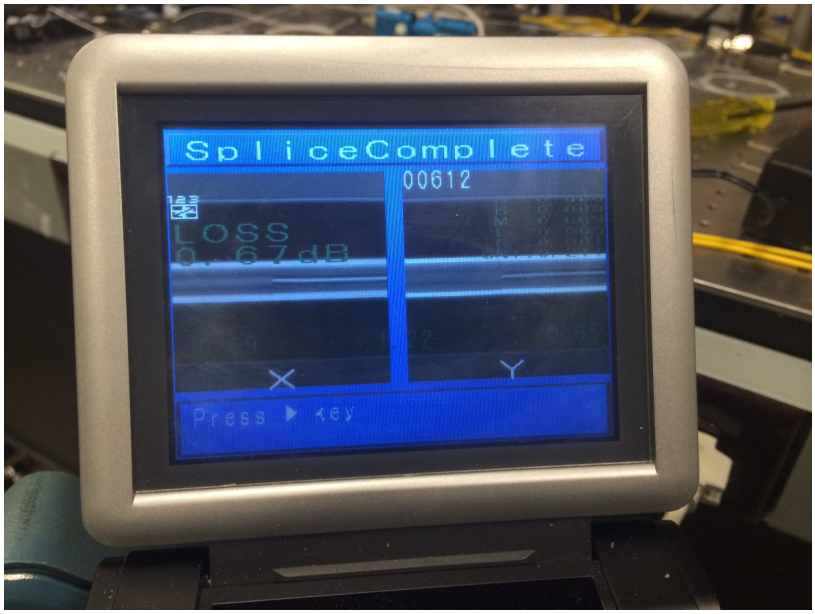

Fig. 2.27.: The actual fiber splicing process

fibers. Then splice the UHNA fiber with two SMF28 on both ends and measure output power again. The output power reduction is due to the two fiber coupling sections. Thus the loss of each fiber coupling section can be calculated. Fig.2.27 shows the actual fiber splicing process and the final result is illustrated in Fig.2.26. U-grooves can assist coupling with both lensed fibers and flat fibers,as shown in Fig.2.28. For lensed fibers, there is an optimum distance between fiber tip and waveguide edge. For flat fibers, the fiber tips should be pressed as close to the waveguide edge as possible to achieve maximum coupling. However, U-groove does have its own shortcomings. The width of U-grooves is designed around 135μm. Its large size limits the on-chip device density. Since flat fibers have larger MFD than lensed fibers, their less spacial sensitivity may enable power coupling without U-grooves. One solution is instead of individual U-grooves for each device, one 65nm deep "step" is etched for all the devices, as shown in Fig.2.29. This method has been experimentally proven to work well with flat fibers and increase device density on-chip.

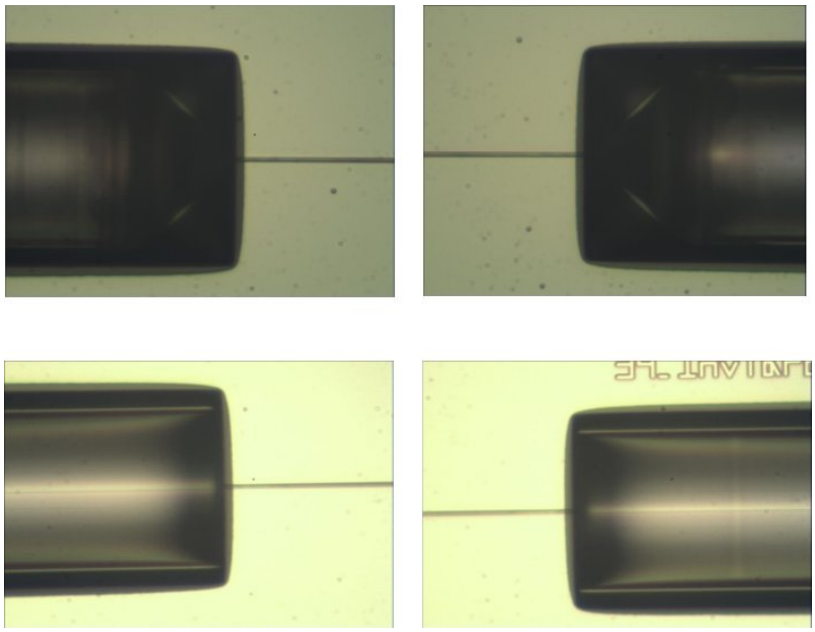

Fig. 2.28.: Lensed fiber coupling vs flat fiber coupling in U-grooves

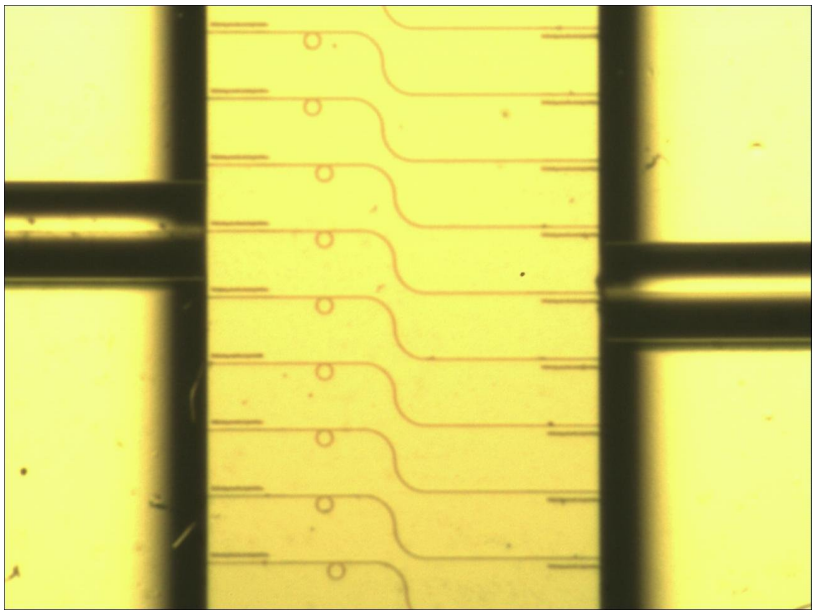

Fig. 2.29.: Flat fiber coupling without U-grooves

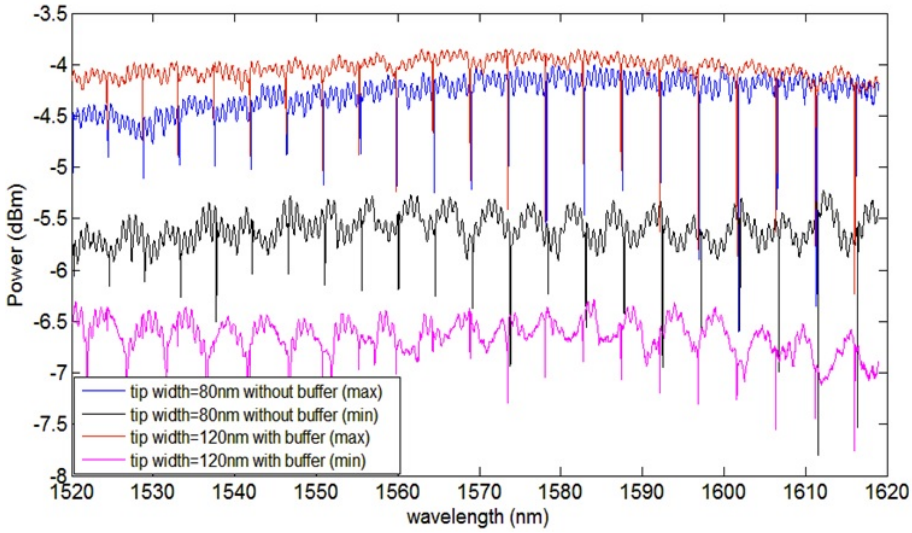

Fig. 2.30.: Measurement result of meta-trident edge couplers with and without center buffers.

The measurement results of both meta-trident edge couplers with and without center buffers using 4μm-MFD flat fiber is shown in Fig.2.30. The input power is normalized to 0dBm. At the polarization for maximum transmission, meta-trident taper with 120nm tip width and buffer shows the highest transmission, higher even than one with 80nm tip width but without buffer. This clearly demonstrates the performance advantage of SWG structure: at the same tip width, SWG can support a larger more circular mode, reducing mode-mismatch. The highest transmission for 0dBm input power is -3.8dBm, translating to 1.9dB/facet loss. Both meta-trident taper designs show broadband performance. It should be noted that meta-trident tapers may potentially be designed using different geometrical parameters to couple with lensed fibers as well.

2.7 Multi-section Inverse Taper with Intermediate cladding

Despite its optimized structures, the meta-trident couplers can still only couple with 4μm MFD HNA flat fibers. The 2μm thick BOX of SOI wafers dictates that

any edge couplers based on a single 220nm silicon layer cannot support fundamentals modes larger than 4μm. Otherwise, the substrate leakage will become an important loss factor. One solution is to add an intermediate cladding low-index waveguide on top of silicon taper. Although there has been previous examples of intermediate cladding, they are either designed for lense fiber [36], or require multi-stages [33], which is challenging to fabricate.

In this work, SU-8 waveguide is formed on top of silicon taper as intermediate cladding. SU-8 not only supports high aspect-ratio structures but also is a low-dose e-beam resist, perfect for exposure of large areas. In this structure, input fiber mode first couples to the large fundamental mode of SU-8 waveguide. During propagation within SU-8, as silicon taper expands in width, the fundamental mode increases in effective refractive index and shrink in size and is gradually converted to silicon waveguide mode. However, for complete conversion, a basic inverse taper should have a length of several millimeters. Such a large device footprint would not only be wasteful but also inevitably increase scattering loss due to surface roughness. Hence the taper length should be limited.

In order to achieve shorten the taper length without compromising its performance, the mode transition is scrutinized. Fig2.31 plots the mode field area of a simple inverse taper as a function of its taper width. It can be seen that the mode area does not change linearly with taper width. Instead, most of the mode area transition takes place in a small window of taper width variation (termed mode transition window). On the other hand, it barely changes during the rest of taper width variation. The phenomena is true for both TE and TM polarizations. The reason for this drastic change in a small window is the effect of mode coupling. Thus the key to balance between mode transition and taper length is to maintain certain taper length within the mode transition window while squeeze its length outside the window. Therefore, a novel multi-section inverse taper(SU-8-Si taper for short) is proposed here and its geometry is shown in Fig.2.32. It has a long section in the middle corresponding to the mode transition window and two short sections at both ends

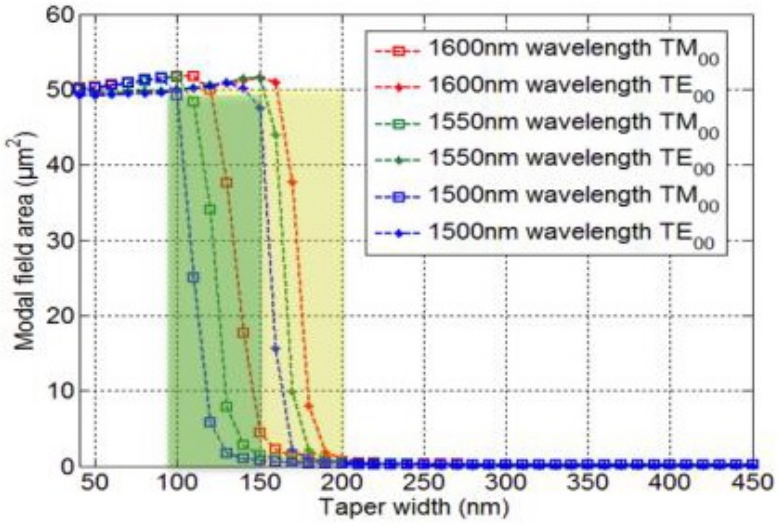

Fig. 2.31.: The mode field area transition in an inverse taper (courtesy of Min Teng)

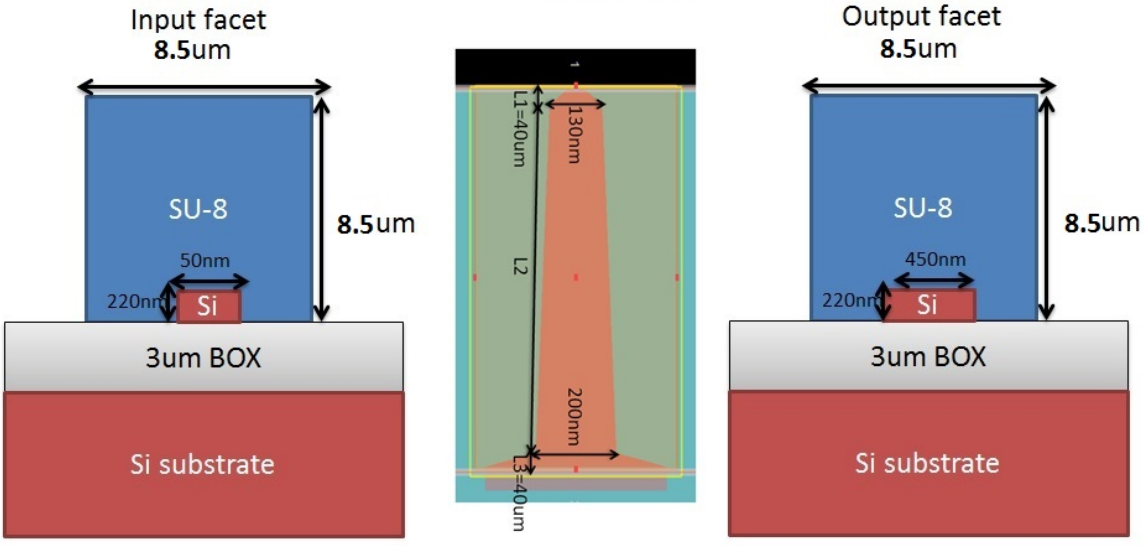

Fig. 2.32.: Top and cross-section view of a multi-section edge coupler

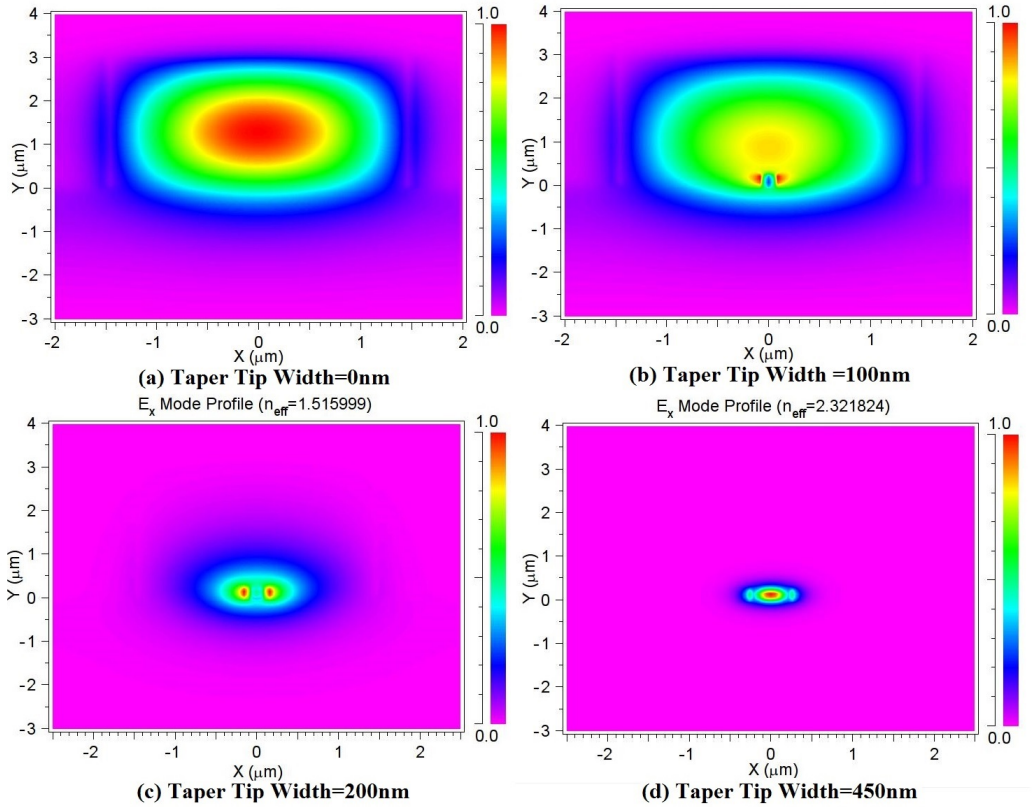

Fig. 2.33.: The TE mode transition in a multi-section edge coupler

corresponding to the regime outside the window. On top of it is a SU-8 low-index intermediate waveguide structure.

The simulation of TE and TM mode transition in the SU-8-Si taper is shown in Fig.2.33 and Fig.2.34 respectively. It can be seen that in both polarizations, the input fiber mode first couples to a relatively large fundamental mode in SU-8 waveguide. As the beam propagates, gradually the mode shrinks in size and its power is transferred into silicon taper until eventually it converts into a silicon waveguide fundamental mode.

Simulation is done on both basic inverse taper cladded with SU-8 waveguide as well as multi-section taper cladded with SU-8 waveguide. The result is shown in Fig.2.35. It can be seen that multi-section taper does enjoy higher transmission than basic inverse taper.

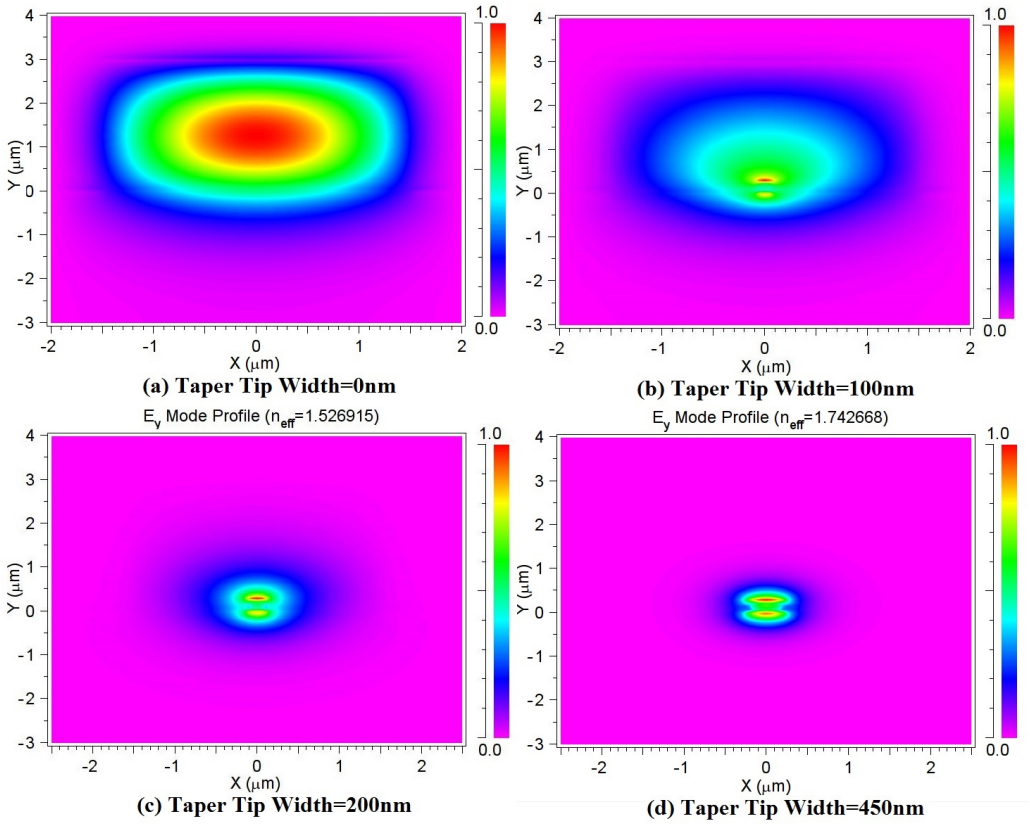

Fig. 2.34.: The TM mode transition in a multi-section edge coupler

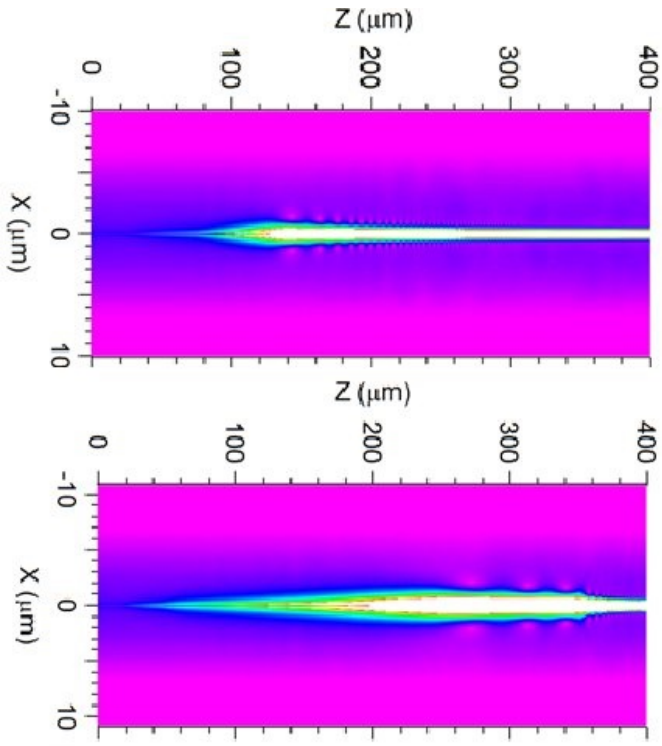

Fig. 2.35.: Comparison between simple inverse taper cladded with SU-8 waveguide and multi-section taper cladded with SU-8 waveguide

The fabrication process of SU-8-Si taper is shown in Fig.2.36. It requires two lithography steps. The first several steps to pattern top silicon layer is the same. Afterwards, instead of LTO depostion, SU-8 is spun on top, exposed and developed into SU-8 waveguide. The SU-8 waveguides do not extend all the way to the edge of the chip. Hence in order to achieve edge coupling, the chip is cleaved on both sides to cut into SU-8 waveguides. The fabricated SU-8 waveguide is shown in Fig.2.37. Its cross-section has dimension of roughly 8.5$\mu\mu$m by 8.5μm, supporting 6μm MFD mode.

This process differs from the previous one for inverse tapers in several aspects. First, LTO is no longer required since SU-8 cannot survive in deposition temperatures. Also, due to the large size of the fundamental mode of SU-8 waveguide (6μm MFD), neither U-grooves nor step etching is necessary. Only an edge cleaving is required to

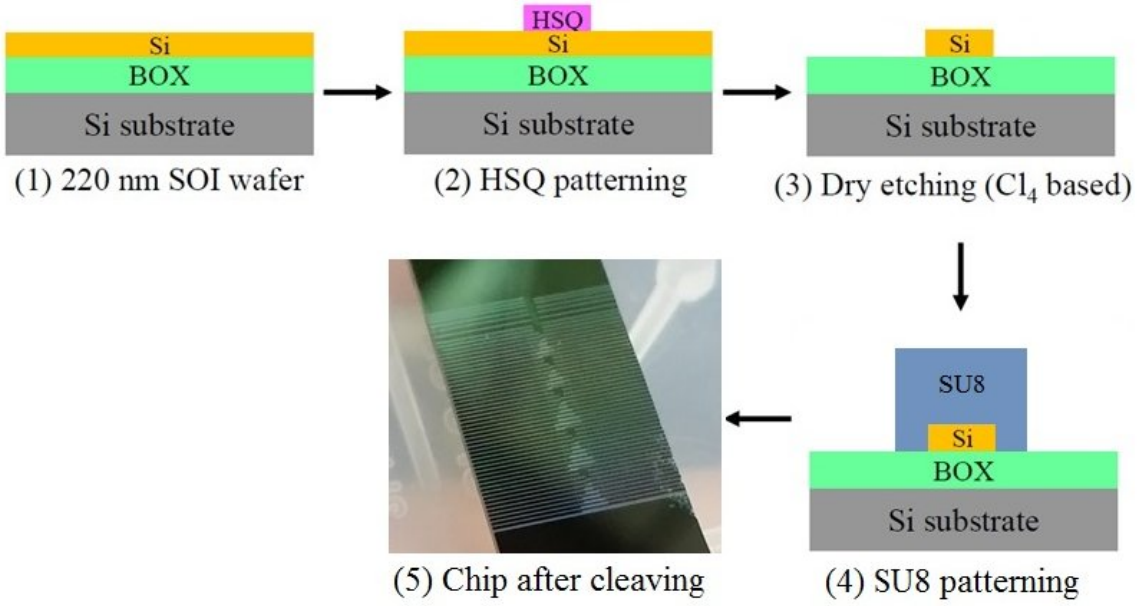

Fig. 2.36.: The fabrication steps of silicon edge coupler cladded with SU-8 waveguide

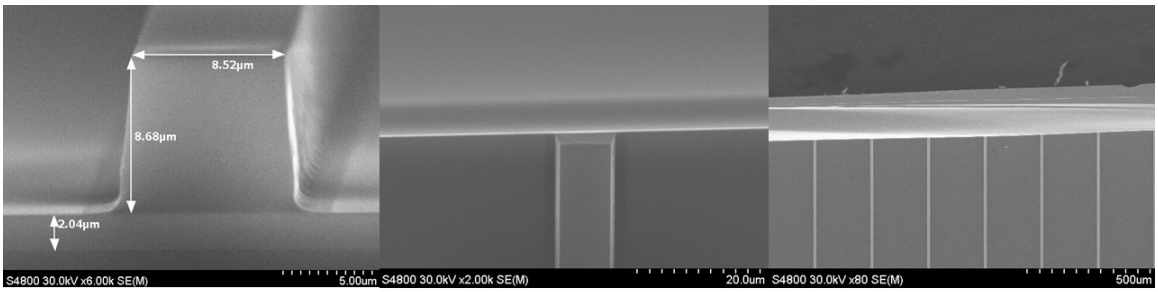

(a) Cross-section of SU-8 waveguide (b) Top-view of SU-8 waveguide (c)Zoomout view of SU-8 waveguides

Fig. 2.37.: The SEM photos of SU-8 waveguides

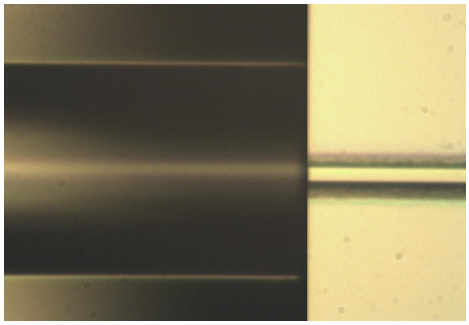

Fig. 2.38.: Fiber coupling to SU8 waveguide.

expose the coupling edge. Here UHNA fibers with 6μm MFD are used to measure the coupler, as shown in Fig.2.38. Since each device still contains several millimeters of SU-8 waveguide and silicon waveguide even after cleaving, their propagation loss should be excluded from the calculation of coupler loss.

To characterize the propagation loss of SU-8 waveguide, three straight waveguides with different lengths are fabricated and measured. The result is plotted in Fig.2.39. It can be seen that the transmission spectra show significant oscillation. The reason is to be further investigated. From the data the SU-8 waveguide propagation loss can be estimated as 2-3dB/cm. This value is in line with previously reported result [39]. Since overestimating SU-8 waveguide loss may lead to underestimating coupler loss, SU-8 waveguide loss is chosen as 2dB/cm. To characterize the propagation loss of silicon waveguide, the aforementioned spiral waveguides with different lengths are introduced again. The extracted silicon waveguide loss is 0.52dB/mm.

The measured transmission spectrum of SU-8-Si taper is shown in Fig.2.40. The laser output power, maximum transmission and other loss mechanisms are listed in Table2.1. Based on the data the coupler loss can be calculated as: $[4.6dBm - (-3.8dBm) - 1.2dB - 3.2\times(0.52)dB - 0.9\times 2dB]/2 = 1.87dB/facet$. The transmission spectrum also shows large swing but between 1535nm to 1555nm the spectrum is relatively flat. The coupler also shows small polarization sensitivity due to its almost square cross-section.

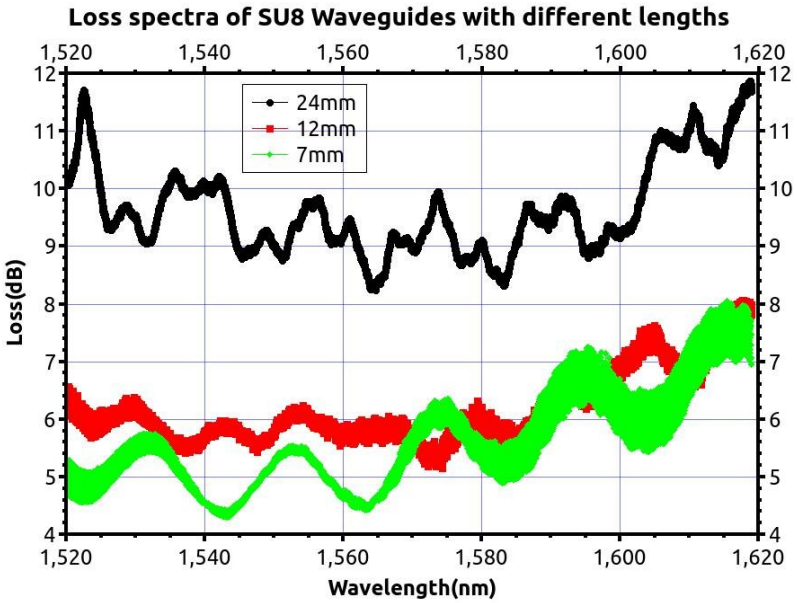

Fig. 2.39.: Propagation loss of SU-8 waveguides with different lengths

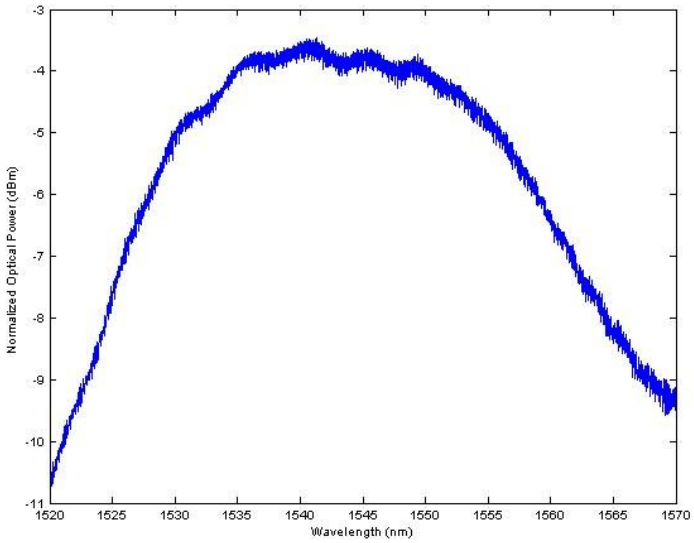

Fig. 2.40.: Measured transmission spectrum of device with silicon taper with SU-8 intermediate cladding

Table 2.1: Different loss mechanisms in SU-8-Si Coupler

Laser Output	4.6dBm
Max Transmission	-3.8dBm
Fiber Splicing Loss	1.2dB
Si Waveguide Loss	0.52dB/mm × 3.2mm
SU8 Waveguide Loss	2dB/cm × 0.9cm

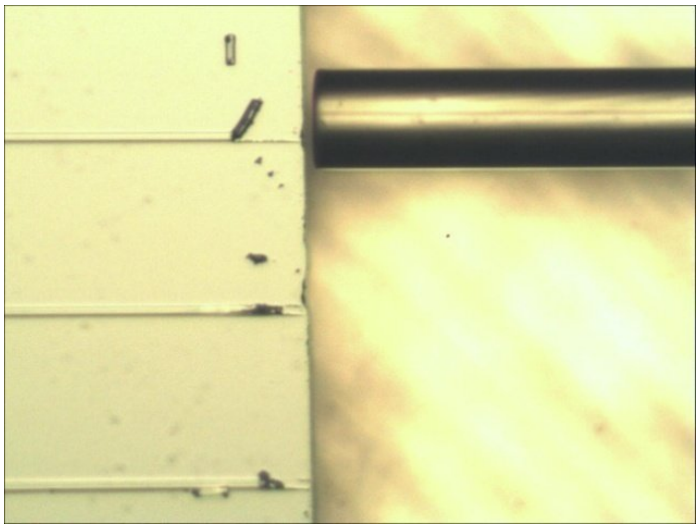

Fig. 2.41.: Damage of SU-8 waveguides by optical fiber

2.7.1 Future Work on Edge Coupler with Intermediate Cladding

At the moment the result of SU-8-Si taper shows large swing in transmission spectrum. In addition, SU-8 is susceptible to damage by fibers during the measurement, as shown in Fig2.41. These issues need to be addressed in the future. If successful, the next step is explore the possibility of SU-8 waveguide on multi-branch trident-shaped tapers. Eventually the goal is to fabricate edge couplers with larger SU-8 cross-section to couple with common SMF with 10μm MFD.

2.8 Other Participated Edge Coupler Work

In addition to the aforementioned edge coupler work, the author also played an auxiliary role in an edge coupler based on double-tip taper and multimode interferometer(MMI) proposed by Jing Wang [40]. Fig.2.42 illustrates the structure of this coupler, which incorporates two-branch, two-stage basic inverse tapers connected to a MMI on one side and another basic inverse taper connected on the other side. Fig.2.43 explains its working principle. On the edge, the double-tip supports a large, round- shaped fundamental mode. As the branches expand in width, the fundamental shrink in size and increase in its effective index. Eventually it becomes two waveguide fundamental modes, which can be fed into a MMI and treated as a high-order mode and converted into the MMI fundamental mode in the output. An output taper may be needed to convert it into a waveguide fundamental mode.

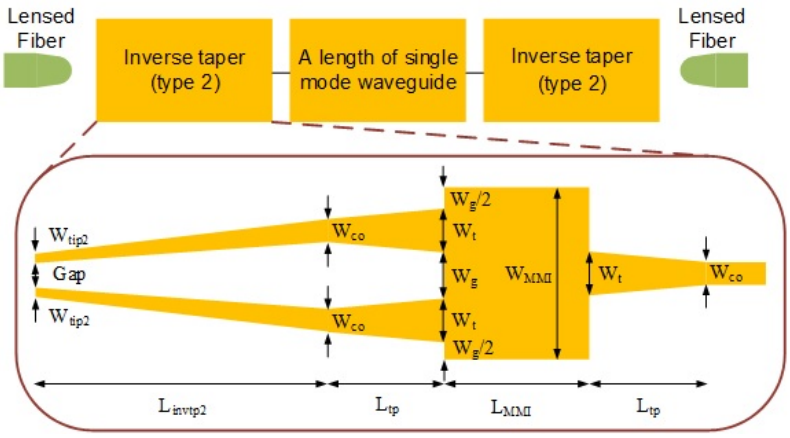

Fig. 2.42.: Mode evolution of an edge coupler based on double-tip taper and MMI [40]

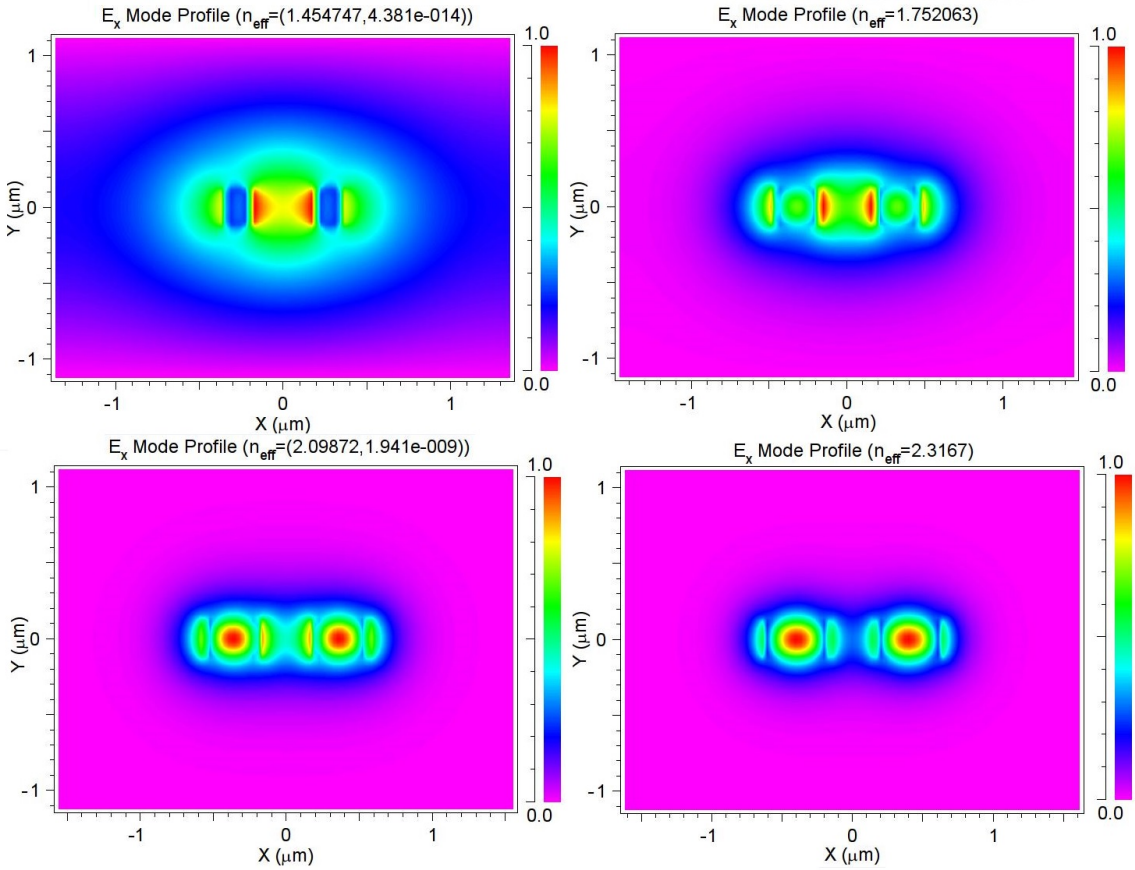

Fig. 2.43.: Mode evolution of an edge coupler based on double-tip taper and MMI [40]

3. THIRD-ORDER OPTICAL NONLINEAR POLYMER WITH LARGE KERR-COEFFICIENT AND NO TWO-PHOTON-ABSORPTION

3.1 A Brief Introduction to Nonlinear Optics

Optics/Electromagnetics is governed by Maxwell's Equations:

$$\nabla \cdot \mathbf{D} = \rho \tag{3.1a}$$

$$\nabla \cdot \mathbf{B} = 0 \tag{3.1b}$$

$$\nabla \times \mathbf{E} = -\frac{\partial \mathbf{B}}{\partial t} \tag{3.1c}$$

$$\nabla \times \mathbf{H} = \mathbf{J} + \frac{\partial \mathbf{D}}{\partial t} \tag{3.1d}$$

$$\mathbf{D} = \epsilon_0 \mathbf{E} + \mathbf{P} \tag{3.1e}$$

$$\mathbf{B} = \mu_0 \mathbf{H} + \mathbf{M} \tag{3.1f}$$

where $\mathbf{D}$, $\mathbf{E}$, $\mathbf{B}$, $\mathbf{H}$, $\mathbf{P}$, $\mathbf{M}$, ρ, $\mathbf{J}$ are termed electric displacement field, electric field, magnetic flux density, magnetic field, polarization field, magnetization field, charge density and current density, respectively. $\epsilon_0 = 8.85 \times 10^{-12}\ F \cdot m^{-1}$ and $\mu_0 = 4\pi \times 10^{-7}\ H \cdot m^{-1}$ are called vacuum permittivity and vacuum permeability.

With low optical intensity, polarization is approximately linear to the incident electric field.

$$\mathbf{P} = \epsilon_0 \chi^{(1)} \mathbf{E} \tag{3.2}$$

where $\chi^{(1)}$ is termed linear optical susceptibility.

With high optical intensity, this linear relation 3.2 no longer holds. Instead, polarization is expressed by a Taylor series.

$$\mathbf{P} = \epsilon_0 (\chi^{(1)} \mathbf{E} + \chi^{(2)} \mathbf{E}^2 + \chi^{(3)} \mathbf{E}^3 + \cdots) \tag{3.3}$$

where $\chi^{(2)}$ and $\chi^{(3)}$ are termed 2nd- and 3rd-order nonlinear optical susceptibility, respectively.

Suppose an optical field has two frequency components:

$$\mathbf{E} = \mathbf{E_1} e^{j\omega_1 t} + \mathbf{E_2} e^{j\omega_2 t} \tag{3.4}$$

Due to the existence of second order susceptibility, its contribution to the polarization field is:

$$\mathbf{P}^{(2)} = \epsilon_0 \chi^{(2)} \mathbf{E}^2 \tag{3.5a}$$

$$= \epsilon_0 \chi^{(2)} (\mathbf{E_1} e^{j\omega_1 t} + \mathbf{E_2} e^{j\omega_2 t})^2 \tag{3.5b}$$

$$= \epsilon_0 \chi^{(2)} (\mathbf{E_1^2} e^{j2\omega_1 t} + \mathbf{E_2^2} e^{j2\omega_2 t} + 2\mathbf{E_1}\mathbf{E_2} e^{j(\omega_1+\omega_2)t}) \tag{3.5c}$$

In Equ.3.5c it can be seen that nonlinear optical effects produce new optical frequencies. The first and third terms represent second-harmonic-generation(SHG) and sum-frequency generation(SFG), both of which are examples of 2nd order nonlinear optical phenomena. In the similar way, 3rd order nonlinear optical phenomena such as third-harmonic-generation(THG) can be derived as in Equ.3.6c.

$$\mathbf{P}^{(3)} = \epsilon_0 \chi^{(3)} \mathbf{E}^3 \tag{3.6a}$$

$$= \epsilon_0 \chi^{(3)} (\mathbf{E_1} e^{j\omega_1 t} + \mathbf{E_2} e^{j\omega_2 t})^3 \tag{3.6b}$$

$$= \epsilon_0 \chi^{(3)} (\mathbf{E_1^3} e^{j3\omega_1 t} + \mathbf{E_2^3} e^{j3\omega_2 t} + 3\mathbf{E_1^2}\mathbf{E_2} e^{j(2\omega_1+\omega_2)t} + 3\mathbf{E_1}\mathbf{E_2^2} e^{j(\omega_1+2\omega_2)t}) \tag{3.6c}$$

3.2 Brief Introduction to Four-Wave-Mixing

One of the most important 3rd-order nonlinear effects is four-wave-mixing(FWM) [41]: In the process, two pump photons interact and both are annihilated. As a result, an signal photon and an idler photon are generated. If two pump photons have different frequency, the process is called non-degenerated four-wave-mixing. Otherwise if the two pump photons have the same frequency, it is called degenerated four-wave-mixing. Applications of FWM include on-chip broad-band optical parametric gain [42], high-speed wavelength conversion [43], micro-resonator based optical frequecy comb(OFC) [21], etc.

3.3 Brief Introduction to Conjugated Polymers

2nd-order optical nonlinearity effect requires materials with ordered crystal lattice without centro-symmetry while 3rd-order optical nonlinearity effect has no special requirement on molecular structures of materials. Hence, polymers, being amorphous, intrinsically do not possess $\chi^{(2)}$ effect but may exhibit $\chi^{(3)}$ effect. Specifically, one type of polymers called conjugated polymers [44] may possess large optical nonlinearities. Conjugated polymers are polymers containing at least one carbon backbone chain of alternating single and double bonds. In this carbon chain, each carbon atom has one unbonded electron perpendicular to the molecular plane called π-electron. The π-electron can move along the carbon backbone under electric field from light, making conjugated polymers potentially optical nonlinear materials.

Both the 2nd and 3rd-order optical nonlinearity of conjugated polymers have played a role in high speed applications. For instance, despite being amorphous,conjugated polymers after electric poling may exhibit eletro-optical effect, a 2nd-order nonlinearity. Indeed electrically poled polymer has been used in high speed, high data rate modulators [45] [46]. In addition, 3rd-order nonlinear polymer is also used in high speed applications using FWM effect [47].

3.4 Platforms to Integrate Polymers On-Chip

There are several ways to integrate polymers on-chip, as shown in Fig.3.1 [28].

1. Thick strip waveguide with fundamental TE mode. The majority of the field is well confined inside the waveguide. Pro: Low propagation loss as the field is far away from the waveguide edge. Con: Mostly silicon nonliearity instead of polymer nonlinearity thus two-photon-absorption (TPA) effect in silicon.

2. Thin strip waveguide with fundamental TM mode. Fundamental TM mode is intrinsically less confined than fundamental TE mode, with a larger portion of the field outside the waveguide, especially in thin waveguides. Pro: More

polymer nonlinearity than TE mode. Con: Larger propagation loss due to a greater part of the field located close to the waveguide edge and still TPA effect in silicon.

3. Slot waveguide with slot mode. The majority of the field is concentrated outside the waveguide between the slot sidewalls. Pro: Field intensity in the slot is much greater than both TE and TM configurations. Polymer nonlinearity dominates. Con: Larger propagation loss due to the majority of the field close to waveguide sidewalls and greater fabrication difficulty than strip waveguide.

4. Photonic crystal Slot waveguide with slot mode at slow speed. Pro: Increased group index and slowing group velocity in PhC waveguide enhances nonlinear effects, reducing the required waveguide length. Con: Challenging to design and fabricate.

Since the goal is to demonstrate nonlinear optical phenomena in polymer and avoid undesirable TPA effect in silicon and since nonlinear optical effects are mostly observable with high optical power, the slot waveguide configuration is adopted in this work. The reason is the slot mode interacts mostly with polymer and the slot waveguide can also be made into micro-resonators.

3.5 Basic Optical Properties of PolyDDMEBT

3.5.1 Molecular Structure of PolyDDMEBT

The specific polymer in this work is termed PolyDDMEBT [48]. Its molecular structure is shown in Fig.3.2 and its formula is $(C_{45}H_{50}N_8O_4)_n$. It can be seen that PolyDDMEBT has alternating single and double bonds, making it conjugated polymer.

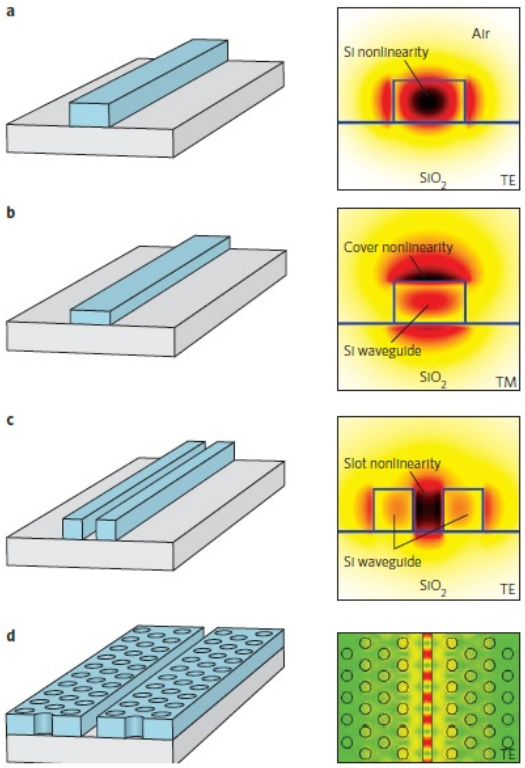

Fig. 3.1.: Four silicon-organic hybrid(SOH) waveguide structures and their electric field distributions [28]

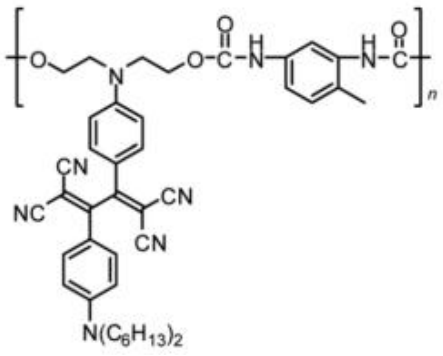

Fig. 3.2.: The molecular structure of PolyDDMEBT

Fig. 3.3.: The surface of spun-on PolyDDMEB thin film on silicon

3.5.2 Spin-Coating of PolyDDMEBT

In bulk form PolyDDMEBT exhibits very dark color, indicating absorption of visible light. It dissolves both in Dichloromethane(CH_2Cl_2) and Tetrahydrofuran(THF, C_4H_8O). 0.05g PolyDDMEBT is dissolved in 1ml THF and the solution shows dark red color. The solution is spun on silicon substrate at 800rpm to form 550nm thin film. Also the solution can be spun on glass substrate at 500rpm to form 450nm thin film. The surface is smooth and free of cracks, as shown in Fig.3.3.

3.5.3 Refractive Index of PolyDDMEBT

The refractive index(both real part n and imaginary part k, $N = n - ik$) of PolyDDMEBT is measured via elliposometry and the result from the wavelength of 700nm to 2500nm is shown in Fig.3.4. Specifically at 1550nm, $n = 1.678$ and $k = 0.0006$.

3.5.4 The Absorbance Spectrum of PolyDDMEBT

The absorbance of PolyDDMEBT is measured using both ellipsometer and spectrometer. The results are shown in Fig3.5. The two measurements agree with each

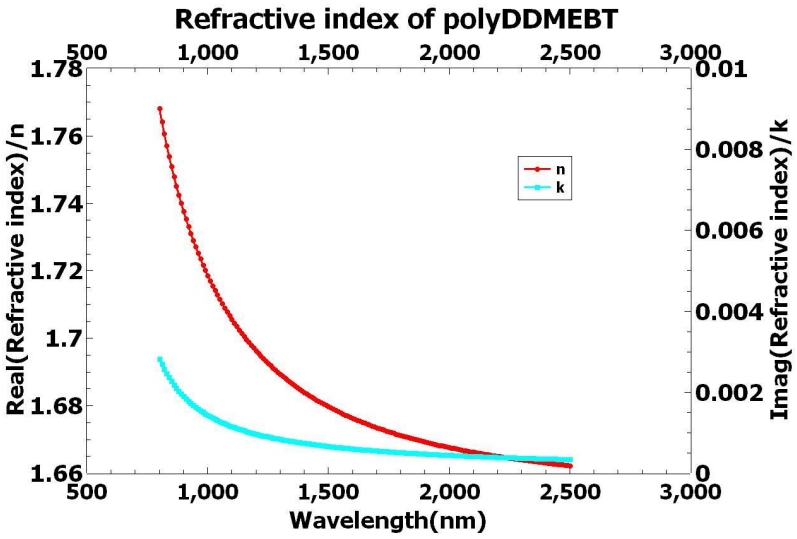

Fig. 3.4.: The refractive index of PolyDDMEBT

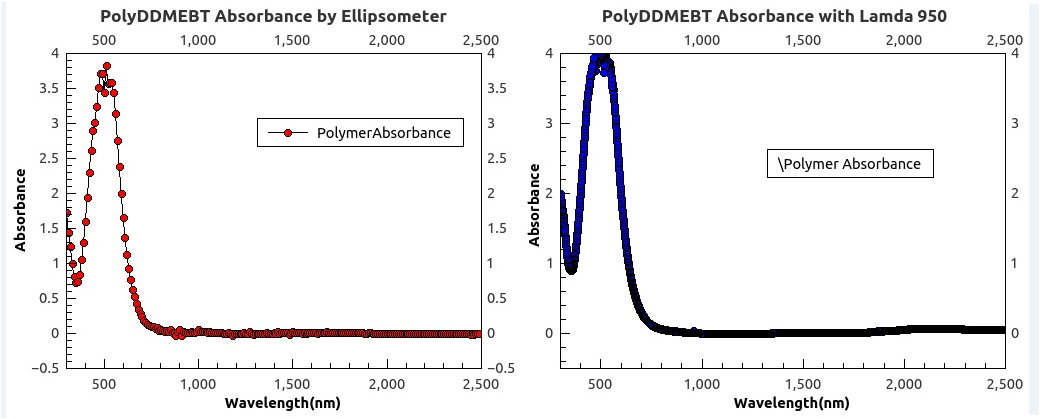

Fig. 3.5.: The absorbance of PolyDDMEBT measured by ellisometer and spectrometer

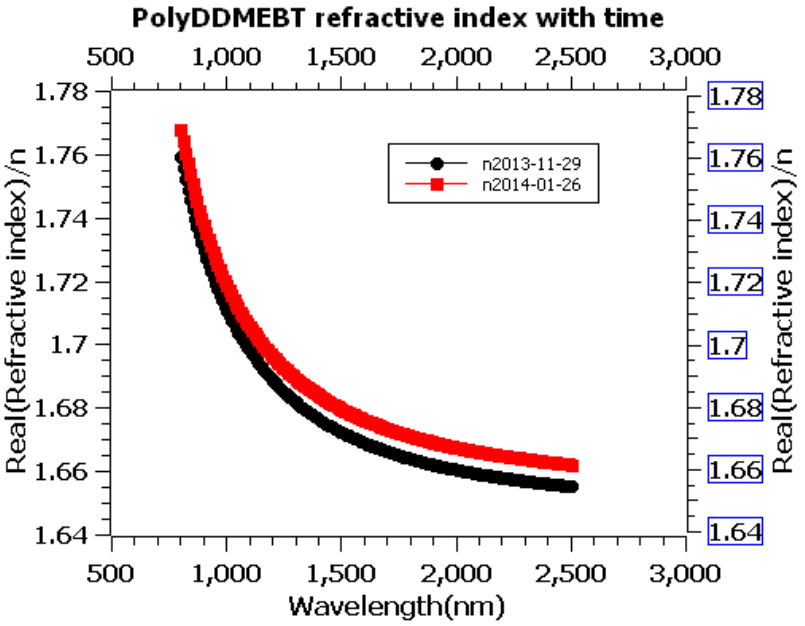

Fig. 3.6.: The temporal stability of PolyDDMEBT

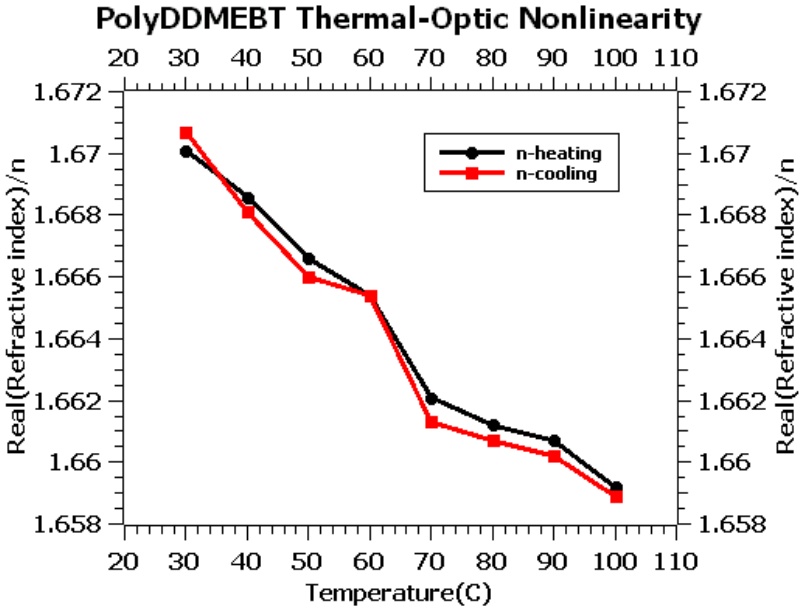

Fig. 3.7.: The Thermal-Optic Nonlinearity of PolyDDMEBT

other very well. It can be seen that according to both results, PolyDDMEBT has absorption in the visible spectrum with a strong absorption peak around 500nm. On the other hand, for wavelength longer than 900nm, PolyDDMEBT has little absorption and is almost transparent. This explains its dark color.

3.5.5 Temporal Stability of PolyDDMEBT

The temporal stability of a material is crucial to its reliability in practical applications. The refractive index of PolyDDMEBT is measured in the span of two months and they show only 0.4% change, as plotted in Fig.3.6. This result proves PolyDDMEBT to be a chemically stable polymer in the atmosphere.

3.5.6 Thermal-Optic Nonlinearity of PolyDDMEBT

Many materials including silicon exhibit thermal optical nonlinearity. In other words, their refractive indices alter with temperature. Hence PolyDDMEBT is measured under different temperatures from 30 °C to 100 °C by gradually heating up the substrate and then cooling down with a step of 10 °C. The result is shown in Fig.3.7. The average thermal-optic coefficient from 30 °C to 100 °C is calculated to be -1.56×10^{-4}. In comparison, silicon has a thermal-optic coefficient of 1.86×10^{-4}. It can be seen that the indices of PolyDDMEBT and silicon alter in different direction with the same temperature change. Thererfore, a mixture form of PolyDDMEBT and silicon may achieve net zero thermo-optic coefficient, making its effective refractive index immune to temperature drift.

3.6 Measurement of Optical Nonlinearity of PolyDDMEBT

3.6.1 High Power Pulsed Laser System

In order to produce measurable nonlinear optical signals, high optical power is required. In this work, a Spitfire high power pulsed laser system is used. The system is composed of 4 major components:

1. A diode-pumped seed laser
2. A mode-locking master oscillator
3. A combination of a pulse stretcher,a chirped pulse amplifier and a pulse compressor
4. An optical parametric oscillator(OPO)

The output of this high power pulsed laser system are laser pulses with 0.8-1W power and 1kHz repetition rate.

3.6.2 Z-Scan Measurement of PolyDDMEBT

Laser Z-scan measurement [49] is a technique to characterize both 3rd-order Kerr-coefficient (closed aperture) and TPA effect (open aperture), as shown in Fig.3.8. The typical closed-aperture curve is shown in Fig.3.9, which has a peak-valley shape. For this measurement, PolyDDMEBT is spun on glass substrate. Fig.3.10 shows the measurement setup of Z-scan, which is composed of the following:

1. A wavelength separator(WS). The high power laser system generates both the desired wavelength as well as unwanted ones. a WS is used to purify the laser beam.
2. After a few reflections, laser beam is focused by a lens and hits the polymer-on-glass sample. The beam hits the polymer film first then the glass substrate.

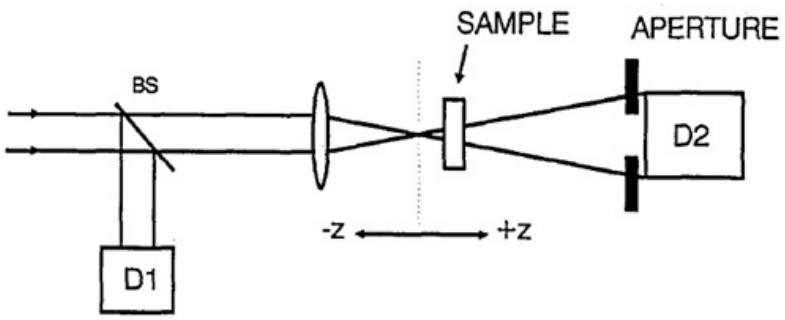

Fig. 3.8.: An illustration of Z-scan measurement setup [49]

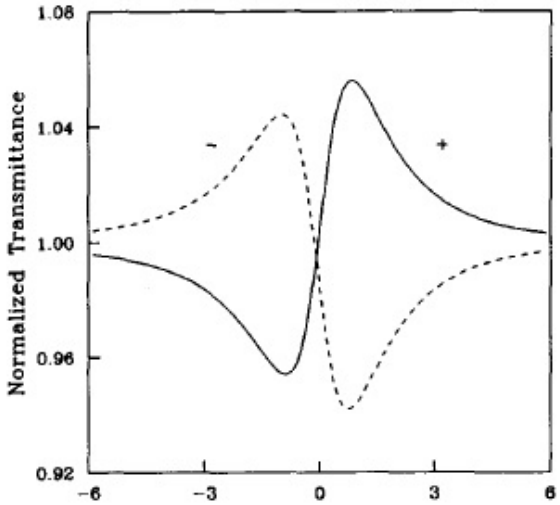

Fig. 3.9.: A typical closed aperture Z-scan curve [49]

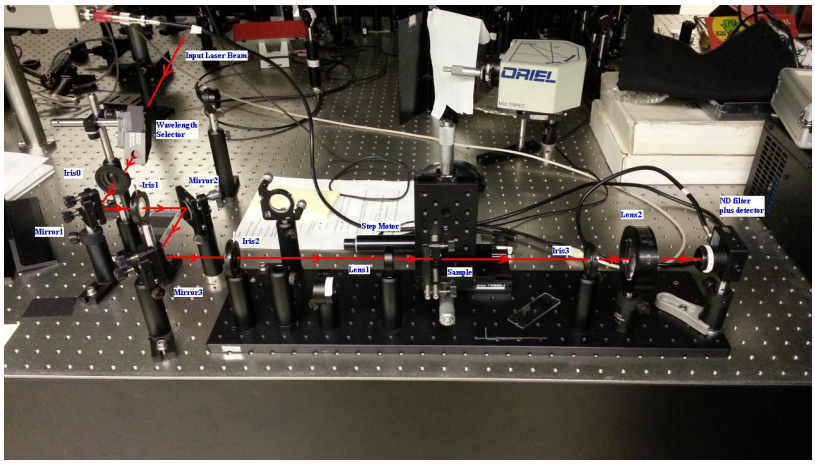

Fig. 3.10.: The real Z-scan measurement setup in this work

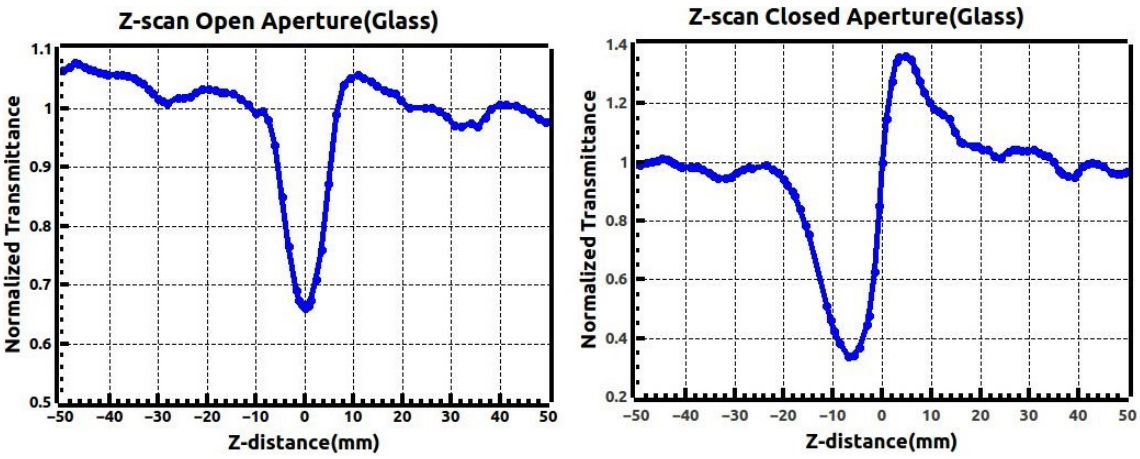

Fig. 3.11.: Z-scan of glass-only sample

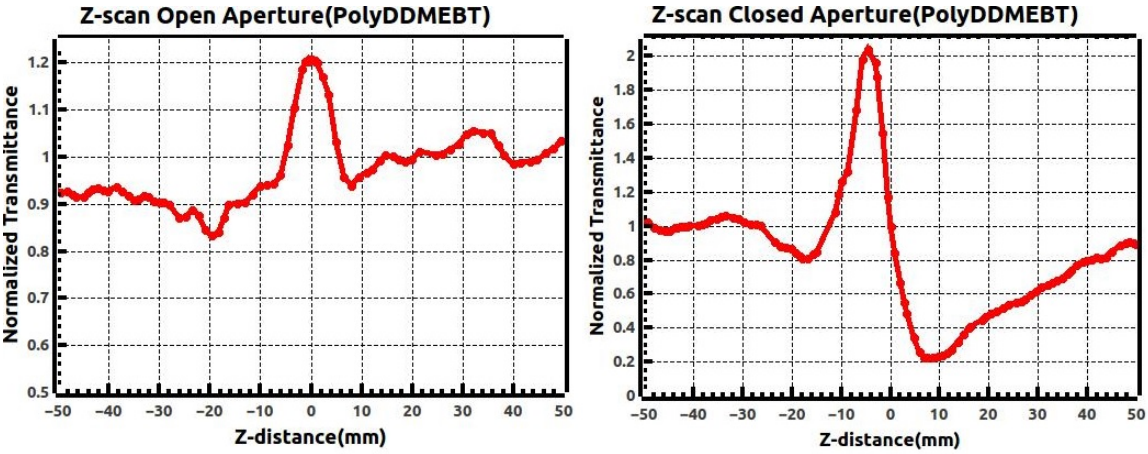

Fig. 3.12.: Z-scan of PolyDDMEBT

At its focal point, the lens creates optical intensity strong enough to generate observable 3rd-order optical nonlinear signal. The sample is mounted on a holder that can move back and forth by a computer-controlled step motor.

3. The beam transmitted from the back of the sample is focused by another lens onto a photo-detector.

3.6.3 Z-scan Measurement Results

Z-scan experiments are conducted at 925nm and Each measurement incorporates both open- and closed-aperture. The results of glass sample is shown in Fig.3.11. The dip in the open-aperture result is a signature of TPA effect and the valley-peak curve indicates glass has 3rd-order Kerr effect. Fig.3.12 shows the results of PolyDDMEBT. The open-aperture result shows a peak instead of a dip, indicating PolyDDMEBT has saturation absorption effect but negligible TPA. The closed-aperture result shows peak-valley curve, meaning PolyDDMEBT has 3rd-order nonlinearity but its Kerr-coefficient has the opposite sign of that of glass.

3.6.4 Z-scan Measurement Result Analysis

According to the theory of Z-scan [50],the transmission difference between the peak and the valley ΔT_{p-v} shown in Fig.3.9 is related to on-axis phase shift $\Delta\Phi_0$ as in Equ.3.7. Equ.3.8 shows that the phase shift $\Delta\Phi_0$ can be expressed by nonlinear refractive index change Δn_0 and linear absorption coefficient α and film thickness L. Δn_0 is directly proportional to the Kerr-coefficient n_2, as shown in Equ.3.9. Beam intensity is the ratio between optical power and beam spot size, as shown in Equ.3.10.

$$\Delta T_{p-v} = 0.405\Delta\Phi_0 \tag{3.7}$$

$$\Delta\Phi_0 = \frac{2\pi}{\lambda}\Delta n_0 \frac{1-e^{-\alpha L}}{\alpha} \tag{3.8}$$

$$\Delta n_0 = n_2 I \tag{3.9}$$

$$I = \frac{P}{\pi r^2} \tag{3.10}$$

From the above equations, the phase shift $\Delta\Phi_0$ can be directly expressed as:

$$\Delta T_{p-v} = 0.405\frac{2\pi}{\lambda}\frac{P}{\pi r^2}\frac{1-e^{-\alpha L}}{\alpha}n_2 \tag{3.11}$$

In the experiment, both glass substrate and PolyDDMEBT are measured. Therefore, Equ.3.11 can be applied to both glass(G) and polymer(P):

$$\Delta T_{p-vG} = 0.405\frac{2\pi}{\lambda}\frac{P}{\pi r^2}\frac{1-e^{-\alpha_G L_G}}{\alpha_G}n_{2G} \tag{3.12}$$

$$\Delta T_{p-vP} = 0.405\frac{2\pi}{\lambda}\frac{P}{\pi r^2}\frac{1-e^{-\alpha_P L_P}}{\alpha_P}n_{2P} \tag{3.13}$$

Divide Equ.3.12 by Equ.3.13:

$$\frac{\Delta T_{p-vG}}{\Delta T_{p-vP}} = \frac{n_{2G}}{n_{2P}}\frac{\alpha_P(1-e^{-\alpha_G L_G})}{\alpha_G(1-e^{-\alpha_P L_P})} \tag{3.14}$$

Note that linear absorption coefficient α is related to the imaginary part of the refractive index k.

$$\alpha = \frac{4\pi k}{\lambda} \tag{3.15}$$

Plug Equ.3.15 into Equ.3.14:

$$\frac{\Delta T_{p-vG}}{\Delta T_{p-vP}} = \frac{n_{2G}}{n_{2P}}\frac{k_P(1-e^{\frac{-4\pi k_G L_G}{\lambda}})}{k_G(1-e^{\frac{-4\pi k_P L_P}{\lambda}})} \tag{3.16}$$

Based on the well-known refractive index information on glass [51],

$$k_G = 9.75 \times 10^{-9}$$

. The Kerr-coefficient and 3rd-order optical susceptibility of glass can be found in [27]:

$$n_{2G} = 3.2 \times 10^{-20} m^2/V$$

$$\chi_G^{(3)} = 2.5 \times 10^{-22} m^2/V^2$$

From the measured dispersion curve of PolyDDMEBT,

$$k_P = 0.0007$$

at

$$\lambda = 925nm$$

. The glass substrate thickness is

$$L_G = 500um$$

and the PolyDDMEBT film thickness is

$$L_P = 450nm$$

.

With all the parameters, it can be derived that

$$n_{2P} \approx -1.2 \times 10^{-16} m^2/W$$

and

$$\chi_P^{(3)} \approx 6 \times 10^{-19} m^2/V^2$$

This value is about 26 times larger than that of crystal silicon [52] and one order of magnitude larger than previously reported DDMEBT [47]. Its Kerr-coefficient is negative because it has opposite sign of that of glass.

3.7 Slot Waveguide and Slot-Micro-Ring Platform

The aforementioned slot waveguide structure is chosen in this work to utilize the strong field intensity in the slot and avoid TPA in silicon. The slot concept can also apply to silicon slot-micro-ring structure in order to further increase the optical power. The brief fabrication process of silicon slot waveguide and slot-micro-ring is as follows:

1. Spin HSQ on a SOI wafer then E-beam lithography and development.

2. RIE etching Si using HSQ as a mask then remove HSQ.

All-pass slot-micro-rings are fabricated and the result is shown in Fig.3.13. The photo shows significant surface roughness on the slot sidewall, which degrades the quality factor of the slot-micro-ring. PolyDDMEBT is spun on top of the slot-micro-ring. Its transmission is measured and the result is plotted in Fig.3.14. Its quality factor is calculated to be 10^3.

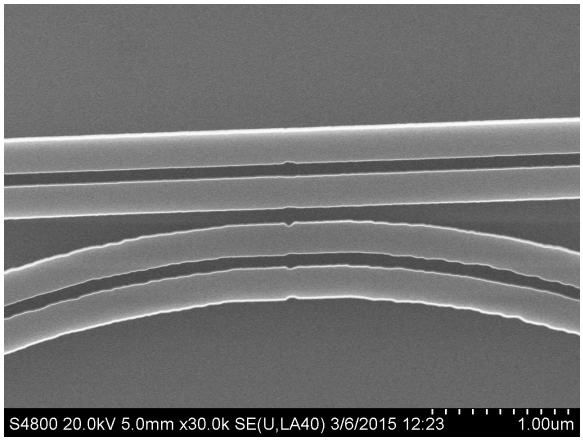

Fig. 3.13.: . SEM photo of a fabricated slot micro-ring coupled to a slot bus waveguide

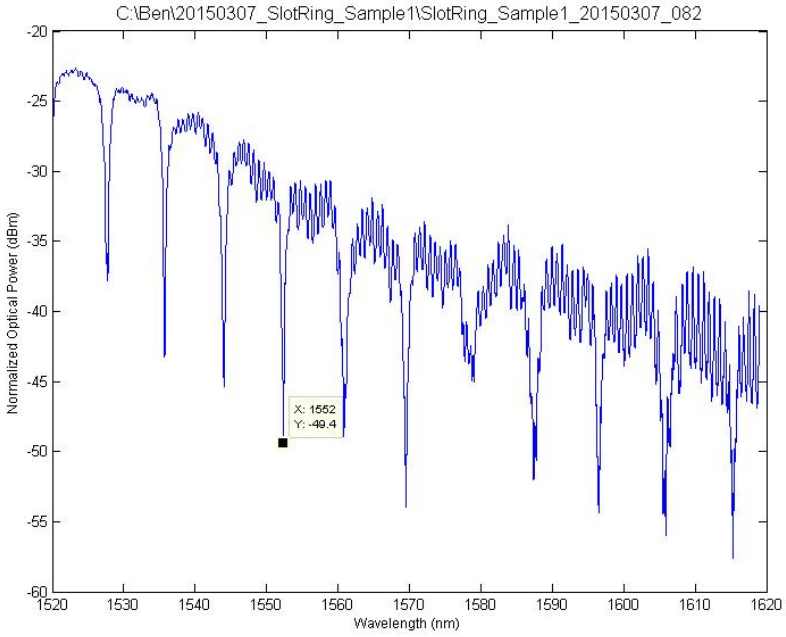

Fig. 3.14.: Transmission Spectrum of Slot Ring

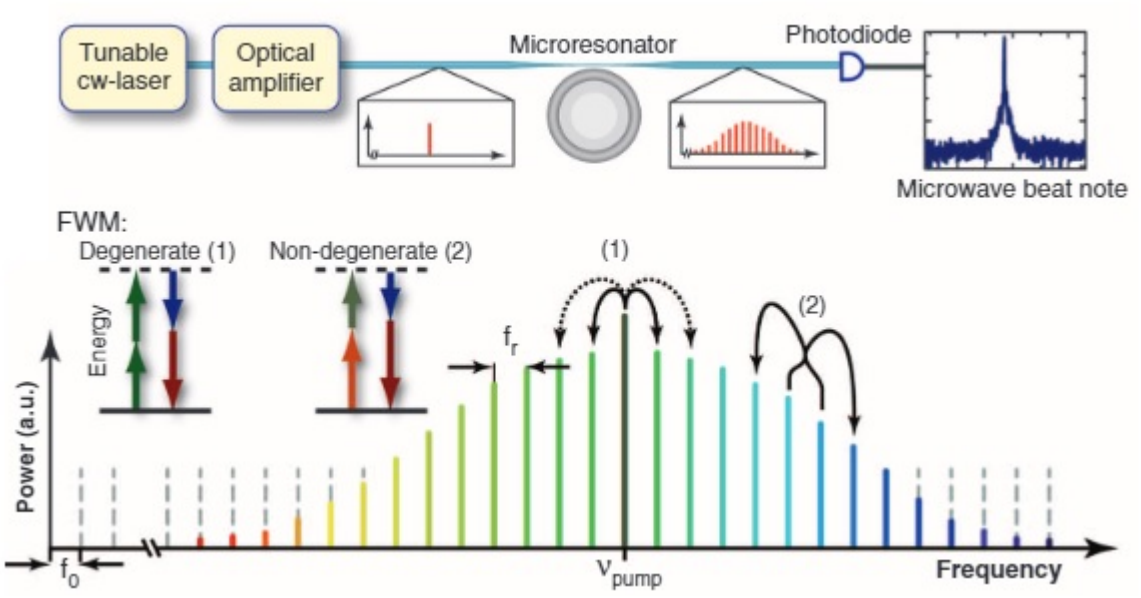

Fig. 3.15.: Illustration of microresonator-based optical frequency combs [21]

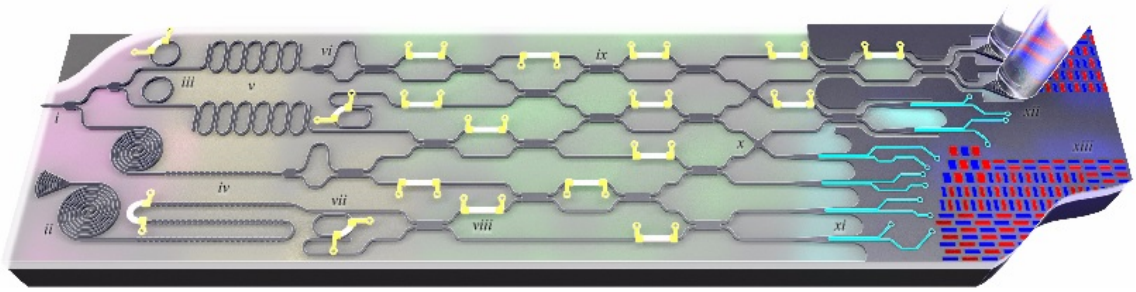

Fig. 3.16.: Illustration of a silicon photonic platform for quantum photonics [53]

3.8 Future Work on the Device Application of PolyDDMEBT

The aforementioned analysis shows that PolyDDMEBT possesses large Kerr-coefficient and negligible TPA effect, making it promising in FWM applications. One of them mentioned in the introduction is called micro-resonator based optical frequency combs(OFC), or Kerr combs [21], as shown in Fig.3.15. Silicon is not a good material for OFC due to its TPA effect. So far, most of the on-chip OFC is achieved either in silicon nitride or fused silica platform [52]. However, these materials suf-

fer from small Kerr-coefficient. To compensate this, micro-resonators with ultra high quality factor must be fabricated to ensure high enough power in the resonator, which is challenging to process. With much larger Kerr-coefficient, PolyDDMEBT potentially may require micro-resonators with much lower quality factor. The best slot-micro-ring has quality factor of 10^4 [54], an order of magnitude higher than the result in this work so far. Therefore, great effort needs to be made to further reduce the surface roughness of the slot sidewall and enhance the Q-factor of the slot-micro-ring.

As mentioned in the introduction, a new field called silicon quantum photonics has emerged as an important FWM application [53]. It relies on coherent photon source generated by spontaneous FWM. Silicon can be used in this case since it usually does not require high power. However the process usually requires long silicon waveguide to produce coherent photons. With larger Kerr-coefficient, PolyDDMEBT may be able to shrink the device footprint.

Since it has negative thermal-optic coefficient, certain structures based on PolyDDMEBT and silicon may potentially achieve close to net zero thermal-optic coefficient, making it almost immune to undesirable thermal drift.

4. AUTOMATIC PHOTONIC LAYOUT GENERATION

4.1 A Brief Introduction to Computer Aided Layout Design

In semiconductor research and industry, layout plays an indispensable bridging role between design and fabrication. Its accuracy is crucial for successful fabrication results. Computer-aided-design(CAD) tools have been widely applied to ensure the efficiency and accuracy of layout designs in modern microelectronics. For instance, Candence supports direct conversion from schematics to layouts. However, CAD tools are still in the early stage and much less potent in on-chip photonics. Manual drawing is still prevalent in many cases, which is slow and susceptible to errors. In this work, a full program-based photonic layout generation tool is developed to generate "Caltech Intermediate Format" (CIF) [55], which can be easily converted into other formats such as "GDSII format" [56] using free software like Klayout. This layout tool is proven capable of not only generating layout for basic photonic structures but also relatively complex devices and circuits.

The fundamental concept of this program is that every on-chip photonic layout design, regardless of its overall complexity, can be decomposed into basic geometric building blocks, such as rectangles, trapezoids, polygons, circles, etc, which are in turn made into functions in the programs. They are then used in structures such as waveguides, tapers, grating couplers, micro-rings etc. These parts in turn can build up more complex structures. In the entire hierarchy, every structure is parameterized, meaning their sizes do not have to be specified until the final layout output. The following are some of the examples. All the codes are written in C-language.

4.2 Program Implementation

4.2.1 Rectangles

In CIF format, each rectangle is defined by its center position (both x and y coordinates), length and width. Thus, the code to implement a rectangle is as follows:

```
void Rect(FILE *fp, double CenX, double CenY, double Len, double Wid)
{/*Rectangle*/
fprintf(fp,"B %d %d %d %d;\n", Round(Len),Round(Wid),Round(CenX),
Round(CenY));
}
```

Since CIF format only accepts integers in nanometers, thus all of the geometric parameters should be rounded. An example can be shown in Fig4.1

4.2.2 Polygons and Regular Polygons

Each polygon is defined by all of its indices (both x and y coordinates), as shown in the following code:

```
void Polygon(FILE *fp, int NumOfVertices, double *Vertices)
{/*Polygon,coodinates(X and Y) saved in Vertices*/
int ii;
fprintf(fp,"P ");
for(ii=0; ii<2*NumOfVertices; ii++)
{ fprintf(fp,"%d ",Round(Vertices[ii])); }
fprintf(fp,"%d %d;\n", Round(Vertices[0]),Round(Vertices[1]));
}
```

One special type of polygons are regular polygons. First the vertices of the regular polygon can be calculated via the following code:

```
void ReguPolyVertices(double CenX, double CenY, double EdgeLen,
int NumOfEdges, double *Vertices)
```

```
{/*calculate the vertices of a regular polygon*/
int ii;
double AngIncre,Ang,Rad;
AngIncre=2*PI/NumOfEdges;
Rad=EdgeLen/2/sin(PI/NumOfEdges);
for(ii=0; ii<NumOfEdges; ii++) /*Angles in radians!*/
{
Ang=ii*AngIncre;
Vertices[2*ii]=CenX+Rad*cos(Ang);
Vertices[2*ii+1]=CenY+Rad*sin(Ang);
}
}
```

Then a regular polygon can be drawn using:

```
void ReguPoly(FILE *fp, double CenX, double CenY, double EdgeLen,
int NumOfEdges, double *Vertices)
{/*Regular Polygon*/ int ii;
ReguPolyVertices(CenX,CenY,EdgeLen,NumOfEdges, Vertices);
fprintf(fp,"P ");
for(ii=0; ii<2*NumOfEdges; ii++)
{ fprintf(fp,"%d ",Round(Vertices[ii])); }
fprintf(fp,"%d %d;\n", Round(Vertices[0]),Round(Vertices[1]));
}
```

4.2.3 Circle

A curve in CIF is always represented by a polygon. Specifically, a circle can be represented by a regular polygon with large enough number of sides, as shown in Fig4.3. Alternatively, CIF allows a circle to be define by its center and radius in the following way:

Fig. 4.1.: The layout of rectangles

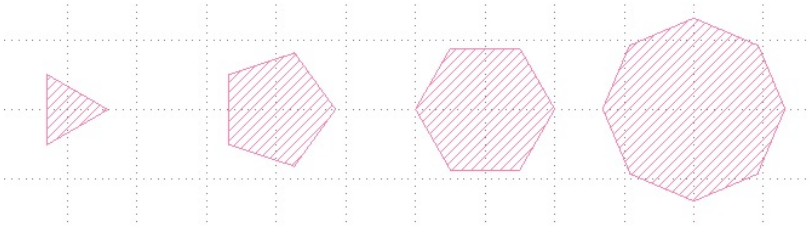

Fig. 4.2.: The layout of regular polygons with different number of edges (3,5,6,8)

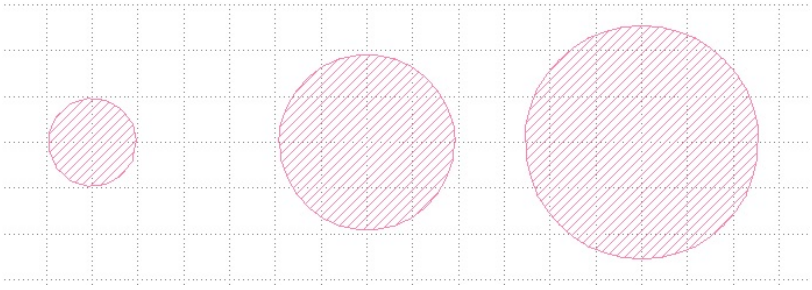

Fig. 4.3.: The layout of circles represented by regular polygons with different number of edges (15,30,40)

```
void Circle0(FILE *fp, double CenX, double CenY, double Rad)
{/*Circle including the inside*/
fprintf(fp,"R %d %d %d;\n",
Round(2*Rad),Round(CenX),Round(CenY));
}
```

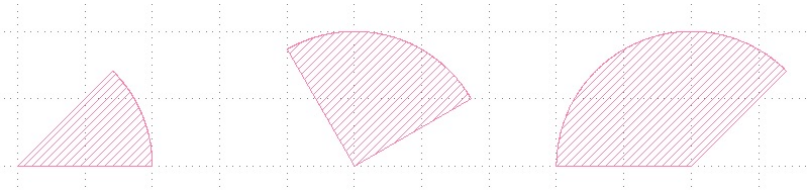

Fig. 4.4.: The layout of circular sectors with different angles

4.2.4 Circular Sector

In many cases, the layout of a circular section is needed such as in grating couplers. It uses a function called CirVertex to calculate all the vertices of a circle:

```
void PartCir_Rad(FILE *fp, double CenX, double CenY, double Rad,
double Start_Ang, double End_Ang)
{/*Partial Circle,0<=Ang_Start,Ang_End<2*PI */
int ii;
double Vertex_X[NumOf_CirVertex], Vertex_Y[NumOf_CirVertex];
CirVertex_Ang(CenX,CenY,Rad,Start_Ang, End_Ang,Vertex_X,Vertex_Y);
fprintf(fp,"P "); /*Polygon Start*/
fprintf(fp,"%d %d ",Round(CenX),Round(CenY));
for(ii=0; ii<NumOf_CirVertex; ii++)
{
fprintf(fp,"%d %d ",Round(Vertex_X[ii]), Round(Vertex_Y[ii]));
}
fprintf(fp,"%d %d;\n", Round(CenX),Round(CenY));
}
```

The result can be shown in Fig4.4.

4.2.5 Rings and Partial Rings

Similar to circular sectors, the partial rings can be expressed as:

```
void PartRing(FILE *fp, double CenX, double CenY, double Rad,
```

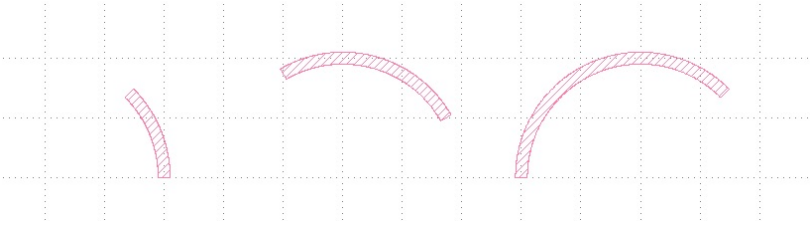

Fig. 4.5.: The layout of partial rings with different angles

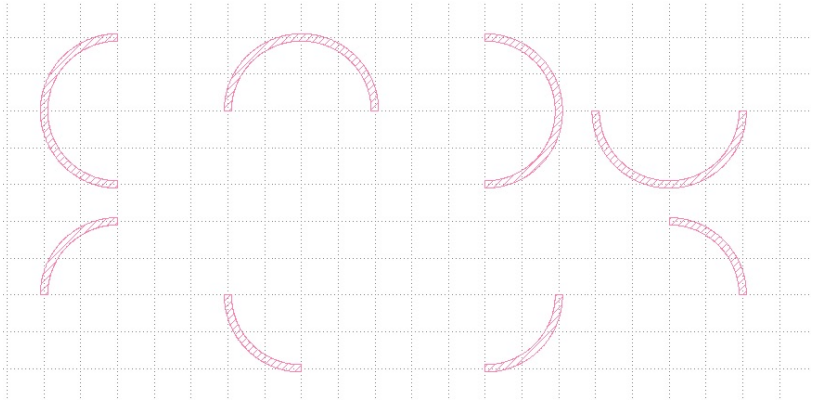

Fig. 4.6.: The layout of waveguide bends of different types

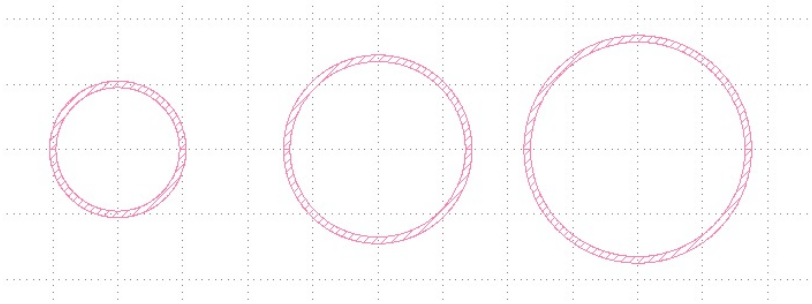

Fig. 4.7.: The layout of rings with different radia

```
double Wid, double Start_Ang, double End_Ang)
{/*Partial Ring in general, Ang in Radians!*/
int ii;
double Rad_In,Rad_Out;
double Vertex_In_X[NumOf_CirVertex], Vertex_In_Y[NumOf_CirVertex],
Vertex_Out_X[NumOf_CirVertex], Vertex_Out_Y[NumOf_CirVertex];
Rad_In=Rad-Wid/2;
Rad_Out=Rad+Wid/2;
CirVertex_Ang(CenX,CenY,Rad_Out,Start_Ang,End_Ang, Vertex_Out_X,
Vertex_Out_Y);
CirVertex_Ang(CenX,CenY,Rad_In,End_Ang,Start_Ang, Vertex_In_X,
Vertex_In_Y);
fprintf(fp,"P "); /*Polygon Start*/
for(ii=0; ii<NumOf_CirVertex; ii++)
{ fprintf(fp,"%d %d ",Round(Vertex_Out_X[ii]), Round(Vertex_Out_Y[ii]));
}
for(ii=0; ii<NumOf_CirVertex; ii++)
{ fprintf(fp,"%d %d ",Round(Vertex_In_X[ii]),
Round(Vertex_In_Y[ii]));
} fprintf(fp,"%d %d;\n", Round(Vertex_Out_X[0]),
Round(Vertex_Out_Y[0]));
}
```

From partial ring function,180 and 90 degrees waveguide bends can be realized.

```
    void HalfRing_L(FILE *fp, double CenX, double CenY, double Rad,
double Wid)
{/*Left Half Ring*/ double Start_Ang,End_Ang;
Start_Ang=PI/2; End_Ang=PI*3/2;
```

```
PartRing_Rad(fp,CenX,CenY,Rad,Wid,Start_Ang, End_Ang);
}
    void QuartRing_UL(FILE *fp, double CenX, double CenY, double Rad,
double Wid)
{/*UpperLeft Quarter Ring*/ double Start_Ang,End_Ang;
Start_Ang=PI/2; End_Ang=PI;
PartRing_Rad(fp,CenX,CenY,Rad,Wid,Start_Ang, End_Ang);
}
    void Ring(FILE *fp, double CenX, double CenY, double Rad,
double Wid)
{/*Ring*/
double Start_Ang,End_Ang;
Start_Ang=0; End_Ang=PI;
PartRing_Rad(fp,CenX,CenY,Rad,Wid,Start_Ang, End_Ang);
PartRing_Rad(fp,CenX,CenY,Rad,Wid,End_Ang, Start_Ang);
}
```

4.3 Simple Photonic Devices

With the basic components ready, more complex devices can be assembled together. The following are some of the examples.

4.3.1 3D Photonic Crystals(PhCs)

PhCs [57–61] are periodic dielectric structures that only allows light of certain wavelengths to propagate, thus creating a photonic bandgap. One example of is the so-called Woodpile structure [62–66] constructed by alternating perpendicular gratings. The program is used to construct woodpile structure shown in Fig4.8 and the result is published in Ref [67]. Another example is based on alternating layers of rods and holes [68–70] which has omni-directional full bandgap. This structure

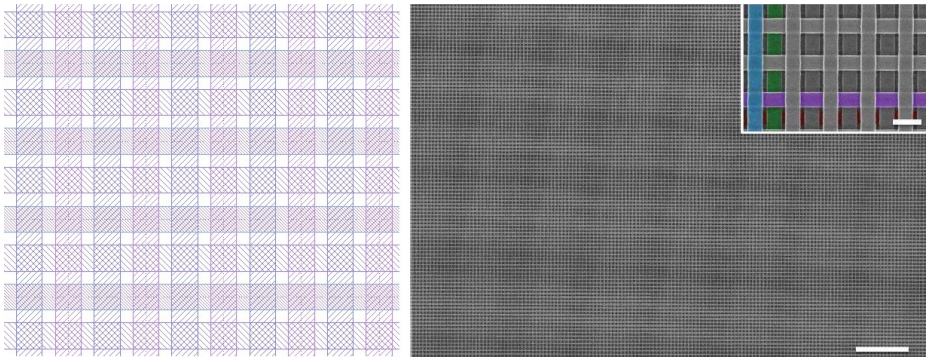

Fig. 4.8.: The layout and SEM photo of a Woodpile photonic crystal [67]

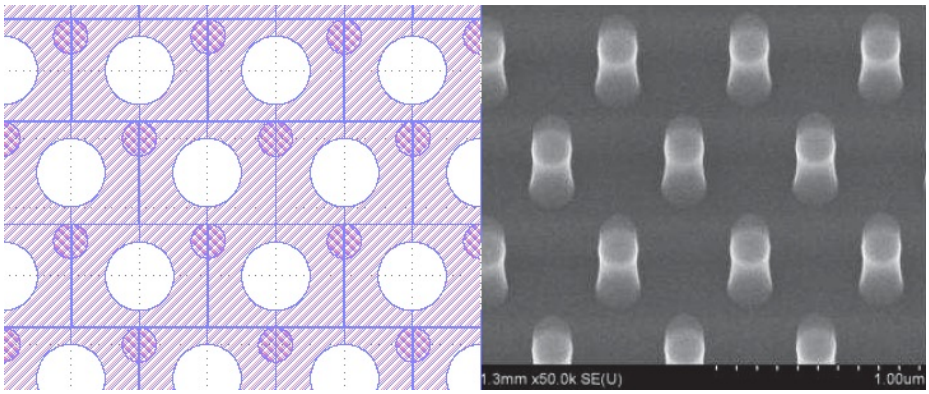

Fig. 4.9.: The layout and SEM photo of a rods-and-holes PhC

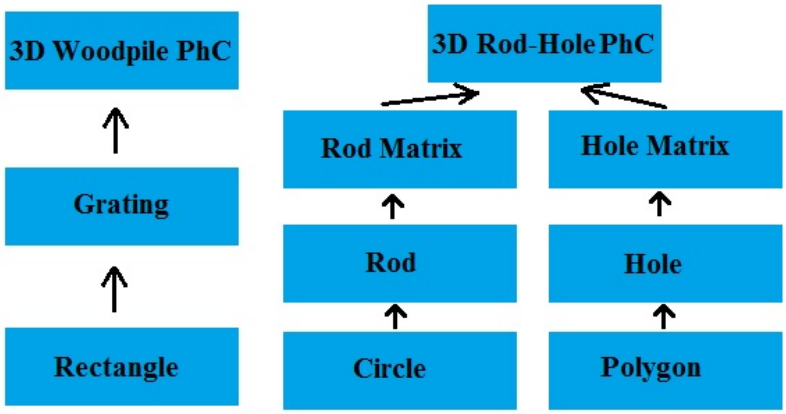

Fig. 4.10.: The program hierarchy for the 3D PhC layouts

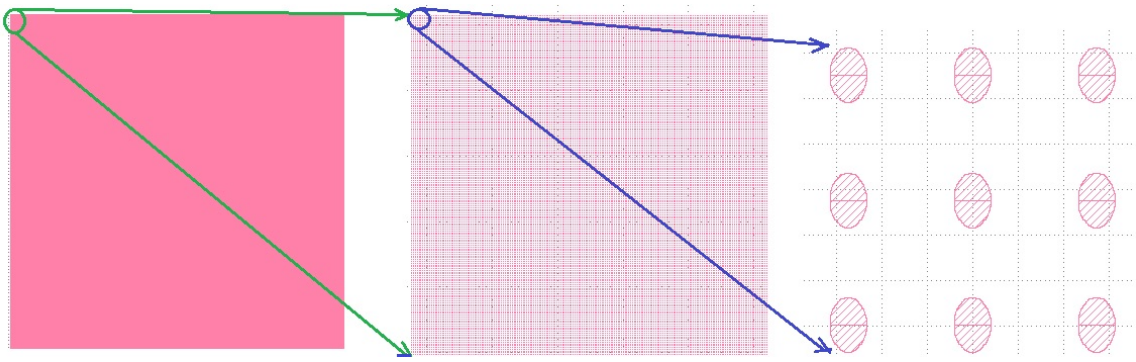

Fig. 4.11.: A layout of large-scale photonic crystal containing 36000×36000 cells of ellipses

generated by the layout program is shown in Fig.4.9. 3D PhC layouts generally can be decomposed into individual layers of 2D PhC, which can be created by a loop of basic unit functions. Their hierarchy in the program can be expressed in Fig.4.10.

A PhC usually contains a great number of unit cells. If each unit is drawn, the total layout can be hundreds of MB or GB especially if each unit is a polygon, circle or ring with numerous vertices, causing difficulty in later viewing and editing. In order to reduce the layout file size, an important feature in CIF format is taken advantage of. CIF allows the same structure to be replicated in both X and Y directions using a simple "T" script instead of specifying the same structures over and over again [55]. For instance, the following program can generate a 36000 × 36000 matrix of ellipses efficiently within a mere 1.2MB layout file in a minute, despite the fact that each ellipse has thousands of vertices. In comparison, if each unit is drawn one by one, the total file size may be in GB and can take up one hour to generate. The layout result is shown in Fig.4.11.

4.3.2 All-Pass Micro-rings with Grating Couplers

Micro-ring based resonators [71] are important on-chip photonic structure used for wavelength filtering [72–74], bio-sensoring [75–77], all-optical control of light [78] even

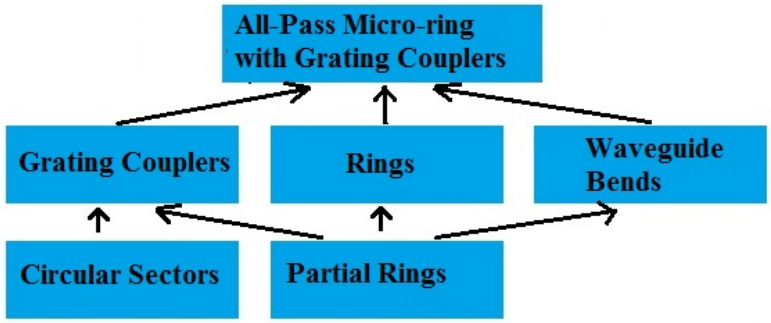

Fig. 4.12.: The program hierarchy for the all-pass micro-ring with grating coupler layouts

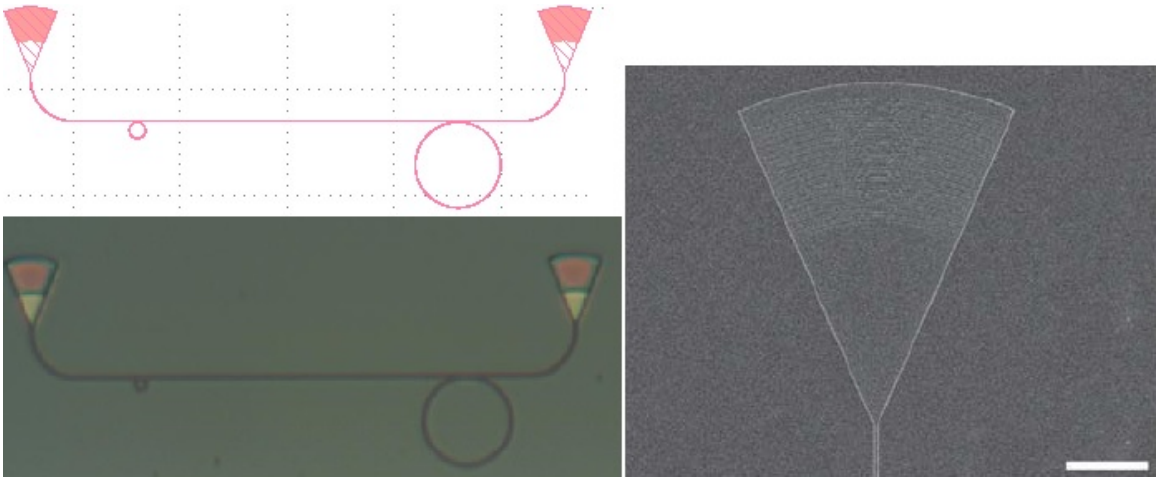

Fig. 4.13.: The layout and SEM photo of an all-pass micro-ring with Grating coupler

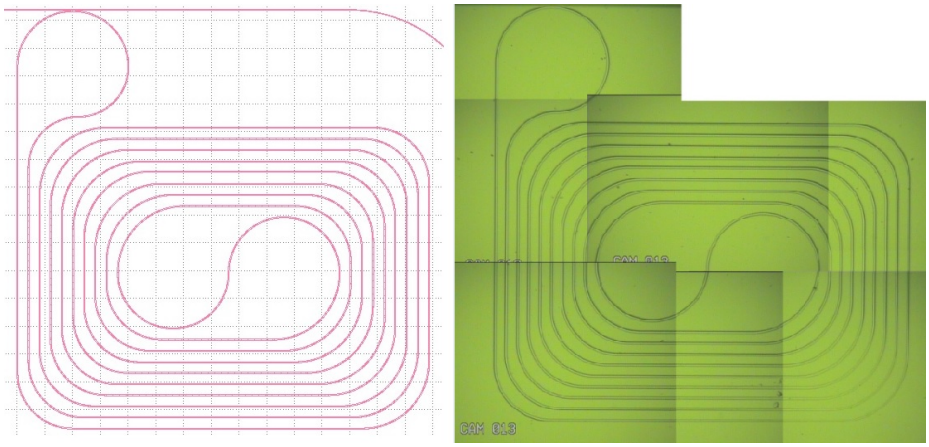

Fig. 4.14.: Spiral Ring Layout and Optical Microscopic Photo of a fabricated device

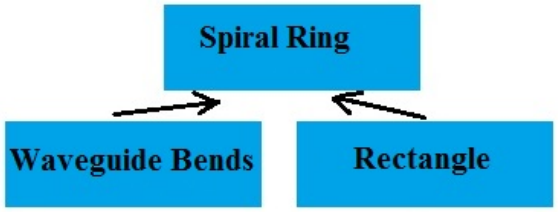

Fig. 4.15.: The program hierarchy for the spiral-shaped micro-ring layouts

all-optical logic [79]. Fig4.13 shows the layout and fabricated device of an all-pass micro-ring with grating couplers used for bio-sensing created by the program tool. This structure can be decomposed into micro-ring and grating coupler structures, both of which can in turn be created by polygon functions. Micro-rings with long circumference can have large device footprint. In order to reduce its size, a micro-ring with large circumference can be bent into a spiral shape [80]. Fig.4.14 is an example of a spiral ring designed by the program as well as its fabrication result.

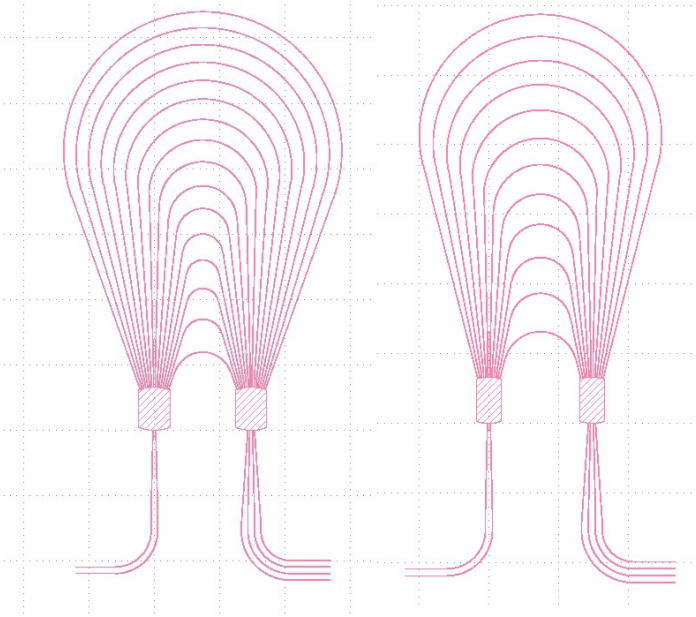

Fig. 4.16.: Layout of AWG

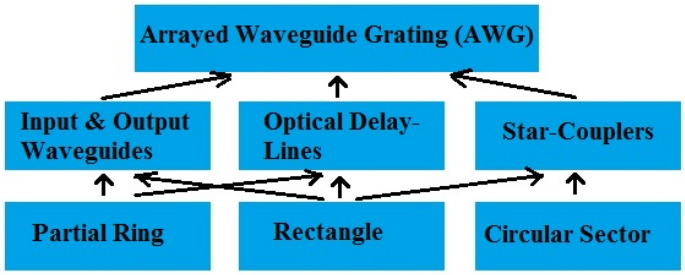

Fig. 4.17.: The program hierarchy for the arrayed waveguide grating (AWG) layouts

4.4 Complex Photonic Devices

4.4.1 Arrayed Waveguide Grating (AWG)

AWG, also know as phasar, are important multiplexing or demultiplexing devices in Wavelength-division multiplexing (WDM) applications [8, 9, 81–83]. The program decomposes the structure into input and output waveguides, star-couplers as well as optical delay lines, as shown in Fig.4.17. The detailed design algorithm is based on Ref. [81]. The program also enables efficient parameter variations. For example, by altering the value of only one parameter in the program, the number of optical delay-lines can be changed automatically, as shown in Fig.4.16.

4.4.2 Micro-Ring-Resonator(MRR)-based Optical Router(OR)

MRR-based ORs are important components for on-chip optical interconnects [84–88], which take advantage of the fact that MRR functions as narrow-band filter. Thus, depending on the wavelength and port of the input light, ideally it has only one certain path and output port. In the layout, micro-racetracks(RT) instead of microrings are used, enabling a longer coupling region. In practice, a fabricated microring is unlikely to have exactly the same dimension as designed, causing a resonant shift from preferred frequency. Thus thermal tuning [89, 90] is necessary to compensate this shift. Fig.4.19 illustrates the hierarchy of OR implemented in the program. Fig.4.18 shows the schematic, generated actual layout and fabrication result of an OR.

4.4.3 Radio-Frequency-Arbitrary-Waveform-Generator (RFAWG)

Modern electronics has reached signal speed in excess of tens of GHz. However, the intrinsic resistance-capacitance (RC) delay limits the future improvement in signal rate. Hence photonics has been used to generate microwave RF signals [91, 92], typically with the help of optical pulse shaping in free space [93, 94]. Then effort

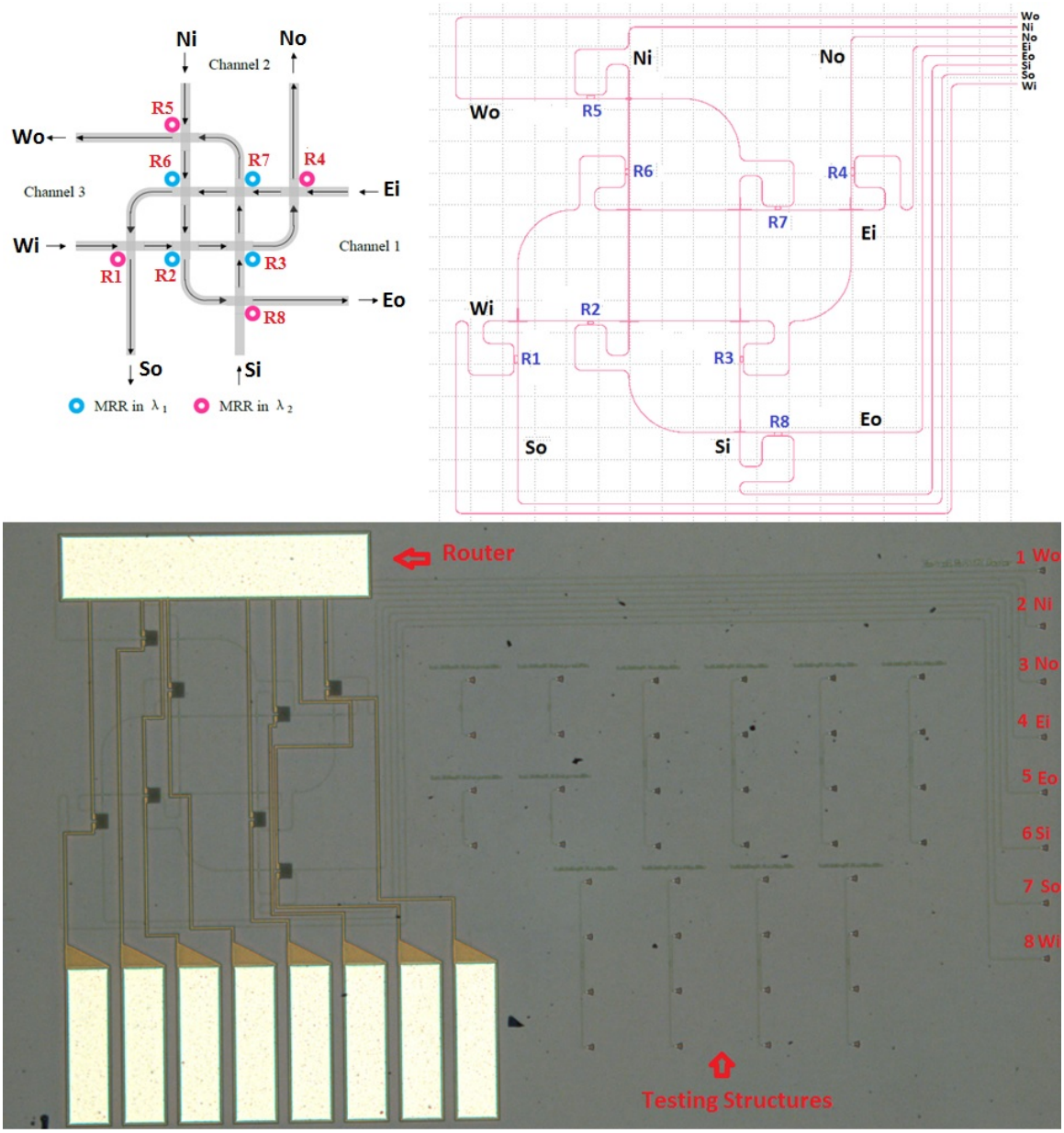

Fig. 4.18.: The schematic, layout and fabricated device of a MRR-based optical router

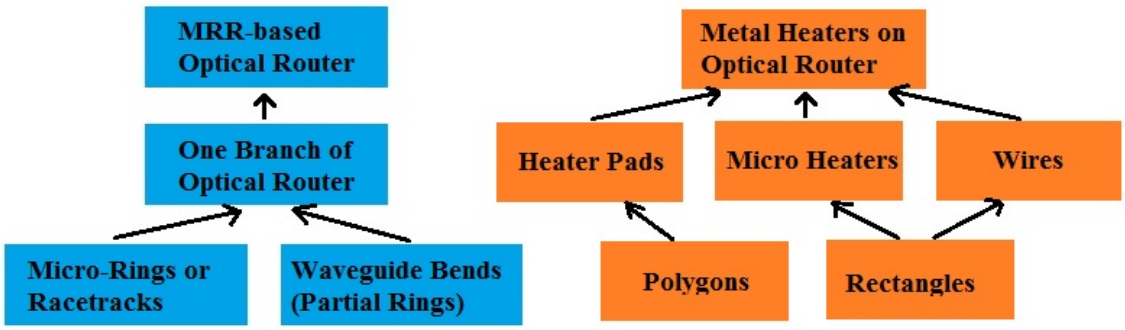

Fig. 4.19.: The program hierarchy for the arrayed waveguide grating (AWG) layouts

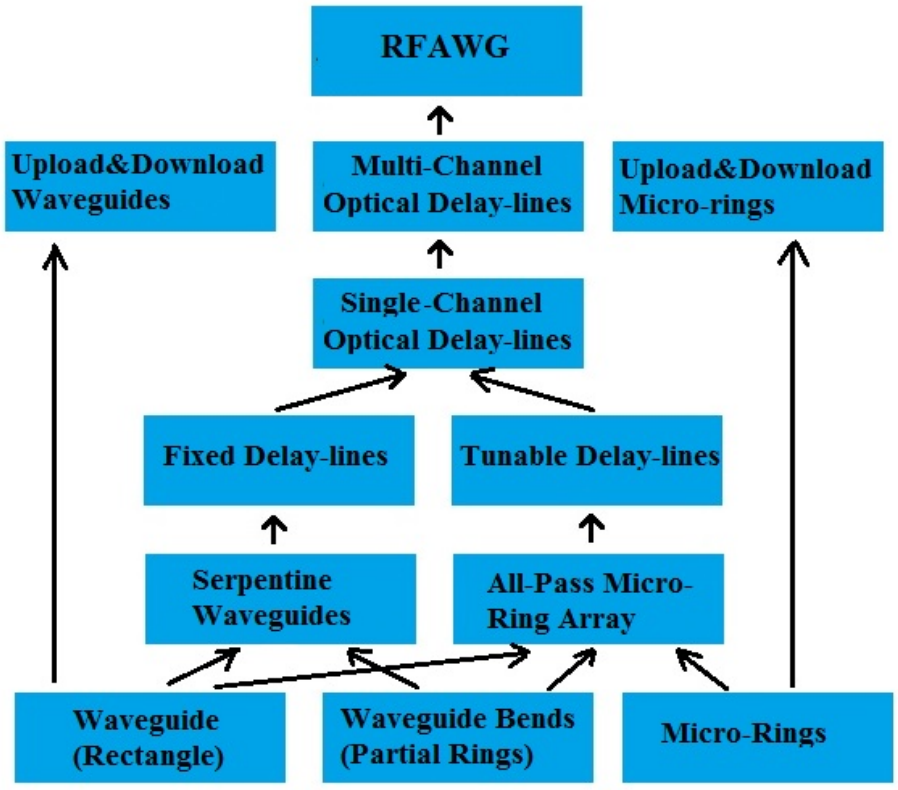

Fig. 4.20.: The program hierarchy for the RFAWG layouts

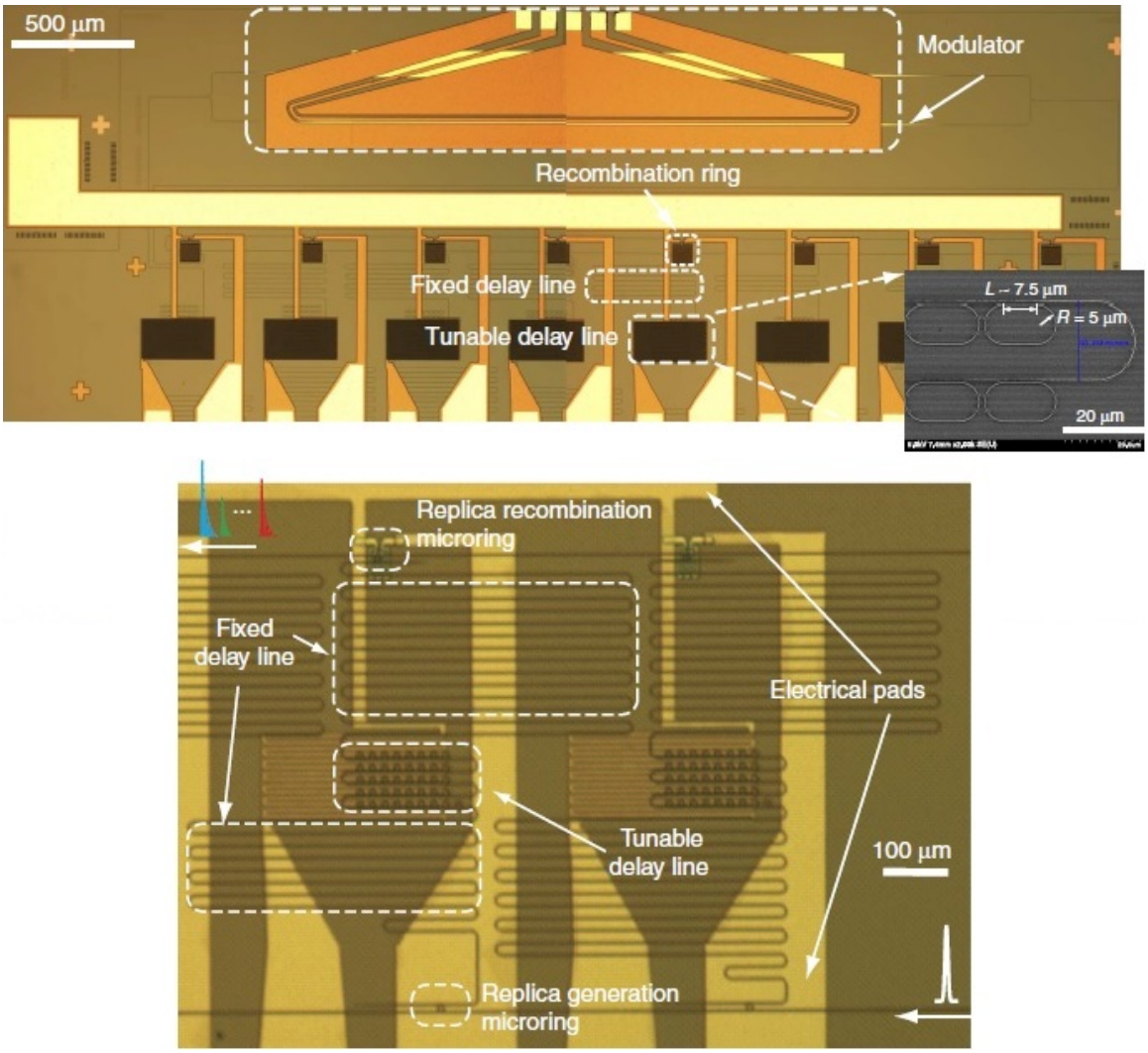

Fig. 4.21.: Optical Microscopic photo of RFAWG with Electro-optic Modulator

has been made to perform RF signals on-chip using silica PLC tecnology [95]. Finally a silicon photonic chip-based radio frequency arbirary waveguide generation is demonstrated [96]. However, it is not completely on-chip since optical fibers of several kilometers are required to perform frequency-to-time-mapping. Fig4.21 shows a completely on-chip silicon photonic RFAWG designed by the program tool and fabricatd in a commercial foundry. It contains 8 channels of integrated optical delay-lines. Each delay-line has different lengths, corresponding to different time delay. Each channel contains two part of delay-lines, fixed delay-line and tunable delay-line. The former is implemented by various length of silicon waveguides and The latter is composed of a number of thermally tuned all-pass microrings [97, 98]. Specifically, one of the channels incorporates a silicon photonic modulator capable of high speed modulation. The entire RFAWG device functions as this: A broadband pulse passes a series of microring resonator called download rings with different resonance frequency. Each downloaded frequency component then goes through different amplitude and phase shift. Eventually these modified frequency components are recombined via a series of upload rings to form a pulse with a new shape. The shape of the output pulse is determined by the amplitude and phase shift experienced by every frequency component respectively. In the same way each ring is equipped with a metal heater for thermal resonant frequency control. The result is published in Ref. [99] in Nature Communications.

The hierarchy of RFAWG is shown in Fig.4.20. From the perspective of layout, the RFAWG poses several challenges. First of all, it contains over 300 microrings. For example, the delay-line in each channel incorporate 41 microrings, with only 2nm difference in the radius of adjacent microrings. Every ring must have the exact same gap between bus waveguide and ring, making their center slightly shifted. This program tool is especially efficient in designing structures with only small variations since precise position and size control by manual drawing would be very cumbersome.

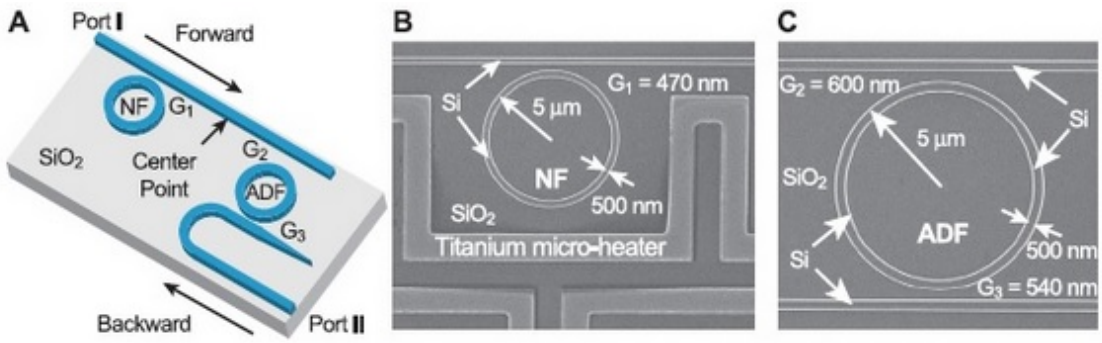

Fig. 4.22.: An all-silicon optical diode [100]

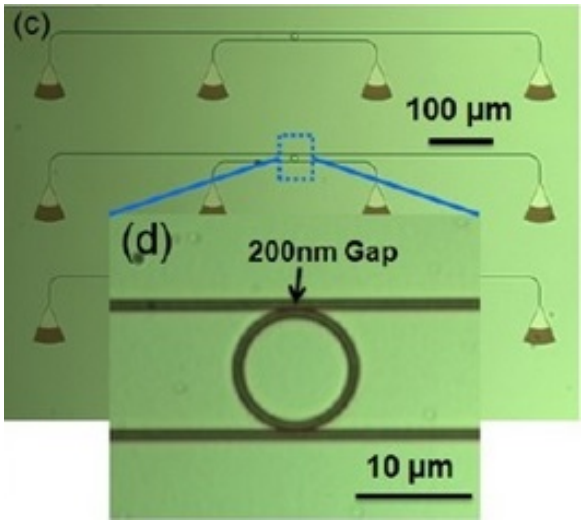

Fig. 4.23.: Silicon photonic devices on flexible substrate [101]

4.5 Other Layout Projects

In addition to the aforementioned work, the layout program also played an important role in the following projects: all-silicon optical diode [100], silicon photonic devices on flexible substrate [101], etc, as shown in Fig.4.22 and Fig.4.23. In addition, the program tool has also been expanded by others to create their own structures. For instance, 3D PhC-based cavity [102] as show in Fig.4.24.

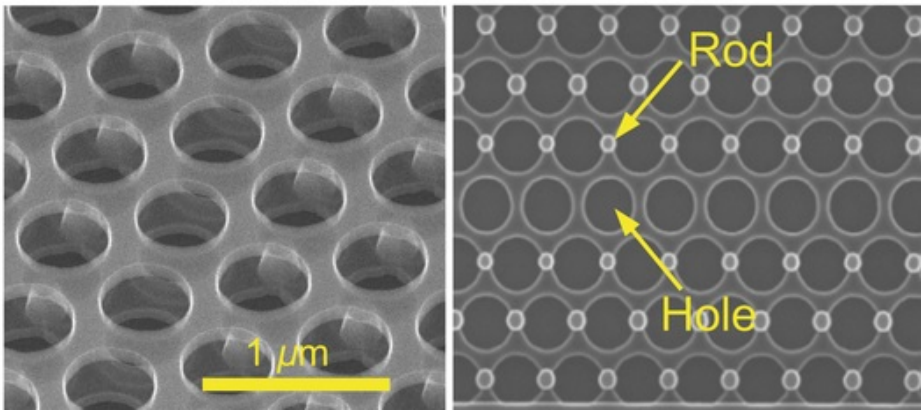

Fig. 4.24.: 3D photonic crystal based cavity [102]

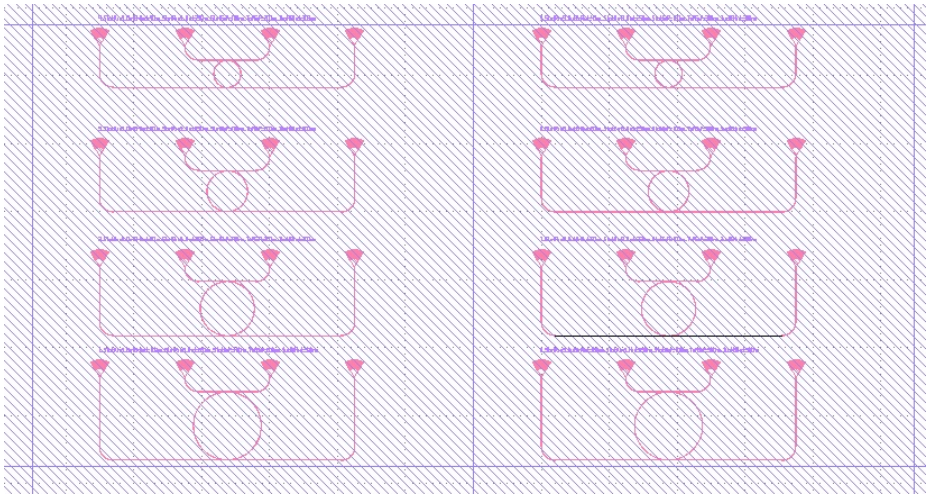

Fig. 4.25.: Parameter sweeping using the layout program

4.6 Advantages of the Layout Program Tool

The goal of this program tool is not just for the developer to use but also for other users. Several advantages of the tool enables this:

1. Although a complex structure may contain an extensive hierarchy from the top down to the basic functions, one is only required to interface with the top function without the need of knowing the underlying hierarchy.

2. The majority of the layouts can be achieved directly by running the program with little need for manual editing, potentially eliminating many human errors.

3. Regardless of its complexity, a structure always has its position defined by one absolute point. The position of every other part in this structure is automatically calculated, since the program internally specifies the relative positions of each component. For instance, in the case of AWG, the center of the left star-coupler may be used as a input position. Once this point is specified, the positions of the other star-coupler, input/output waveguides and optical delay-lines are automatically calculated based on their respective sizes. This potentially removes the errors of assembling complex structures.

4. In practice the same structure may be fabricated with many sets of geometric sizes. This is also known as parameter sweep. Since every geometry is defined in parameters not specific values, it is extremely efficient to do parameter sweep simply by invoking a loop. A simple example is shown in Fig.4.25, in which from top to bottom the radius of micro-rings changes and from left to right the period of grating couplers changes.

5. As shown in previous examples, the basic functions are used in many different structures. This proves the re-usability of its fundamental components, saving the time of manually redrawing the same geometries.

6. The program is open to additions of other structures designed by other users, provided they use the same underlying basic functions. Hence, it is easy to expand the program tool.

4.7 Future Improvement on Layout Programs

The layout program has proven itself capable in many different structures and designs. Nonetheless, although the majority of the layout can be generated automatically, the final layout check is still done manually. Therefore, the program tool can be further improved in the following ways:

1. Automatic parameter values checking: many parameters have practical limitations on their values. For instance, the number of grating teeth can only be a positive integer. Or the coupling gap between a micro-ring and its bus waveguide should be around hundreds of nanometers instead of hundreds of micrometers. The incorrect values will lead to mistakes in the layout, which take time to correct manually. Hence, automatic parameter checking should be implemented in the future.

2. Automatic design rule check(DRC): for instance, the smallest feature in any layout should be equal or larger than certain minimum value dictated by the fabrication process. Likewise, the distance between any features should also be no less than that minimum value. A built-in DRC will speed up the layout correction.

5. SUMMARY

To sum up, in this work various types of high-efficiency edge couplers are demonstrated. First, loss mechanisms of basic inverse taper couplers as well as cantilever-encapsulated inverse taper couplers are analyzed and experimentally verified. Then in order to couple efficiently with flat fibers with larger mode-field-diameter(MFD), a novel sub- wavelength grating based edge coupler is proposed and experimentally demonstrated to have 1.9dB/facet loss. To couple with flat fibers with even larger MFD, a silicon multi-section taper cladded with intermediate SU-8 waveguide is proposed and experimentally demostrated. Based on the result several suggestions are proposed for further improvement.

In order to explore novel materials with larger 3rd-order optical nonlinearity a novel nonlinear optical polymer termed PolyDDMEBT is experimentally characterized, including both its linear and nonlinear optical properties. The result shows that the material has a real part refractive index of 1.68 and negligible absorption in 1550nm, as well as negative thermo-optical coefficient. In addition, Z-scan measurement shows large Kerr-coefficient and no presence of TPA in this polymer. The results suggest that PolyDDMEBT may be potentially useful for 3rd-order optical nonlinear applications.

Finally a program tool for automatic on-chip photonics layout generation is demonstrated. This tool is proven capable of generating both simple and complex on-chip photonic layouts. And it enjoys several advantages over manual drawing in its efficiency in parameter sweeping, re-usability of components, flexibility in addition by other users etc.

LIST OF REFERENCES

LIST OF REFERENCES

[1] G. E. Moore, "Cramming more components onto integrated circuits, Reprinted from Electronics, volume 38, number 8, April 19, 1965, pp.114 ff.," *IEEE Solid-State Circuits Newsletter*, vol. 20, pp. 33–35, sep 1965.

[2] T. Miya, "Silica-based planar lightwave circuits: Passive and thermally active devices," *IEEE Journal on Selected Topics in Quantum Electronics*, 2000.

[3] C. R. Doerr and K. Okamoto, "Advances in Silica Planar Lightwave Circuits," *Journal of Lightwave Technology, Vol. 24, Issue 12, pp. 4763-4789*, vol. 24, no. 12, pp. 4763–4789, 2006.

[4] "Monolithic integration of a silica AWG and Ge photodiodes on Si photonic platform for one-chip WDM receiver," *Optics Express*, vol. 20, p. 9312, apr 2012.

[5] B. Jalali and S. Fathpour, "Silicon Photonics," *JOURNAL OF LIGHTWAVE TECHNOLOGY*, vol. 24, no. 12, 2006.

[6] R. Soref, "Silicon Photonics: A Review of Recent Literature," 2010.

[7] A. Dhiman, "Silicon Photonics: A Review," *IOSR Journal of Applied Physics*, vol. 3, no. 5, pp. 67–79, 2013.

[8] D. Dai, L. Liu, L. Wosinski, and S. He, "Design and fabrication of ultra-small overlapped AWG demultiplexer based on a-Si nanowire waveguides," 2006.

[9] D. Dai and J. E. Bowers, "Silicon-based on-chip multiplexing technologies and devices for Peta-bit optical interconnects," *Nanophotonics*, vol. 3, no. 45, pp. 283–311, 2014.

[10] J. Sun, E. Timurdogan, A. Yaacobi, E. S. Hosseini, and M. R. Watts, "Large-scale nanophotonic phased array," 2013.

[11] R. Chen, T.-T. D. Tran, K. W. Ng, W. S. Ko, L. C. Chuang, F. G. Sedgwick, and C. Chang-Hasnain, "Nanolasers grown on silicon," *Nature Photonics*, vol. 5, pp. 170–175, mar 2011.

[12] Q. Xu, B. Schmidt, S. Pradhan, and M. Lipson, "Micrometre-scale silicon electro-optic modulator," *Nature*, vol. 435, pp. 325–327, may 2005.

[13] "Silicon Nanophotonic Packaging." `http://researcher.watson.ibm.com/researcher/view_group.php?id=5517`.

[14] "Intel 100G Optical Transceiver Brief." `http://www.intel.com/content/www/us/en/architecture-and-technology/silicon-photonics/optical-transceiver-100g-cwdm4-qsfp28-brief.html`.

[15] "The American Institute for Manufacturing Integrated Photonics." http://www.aimphotonics.com/.

[16] "STREAMS EU PROJECT." http://www.ict-streams.eu/.

[17] C. Sun, M. T. Wade, Y. Lee, J. S. Orcutt, L. Alloatti, M. S. Georgas, A. S. Waterman, J. M. Shainline, R. R. Avizienis, S. Lin, B. R. Moss, R. Kumar, F. Pavanello, A. H. Atabaki, H. M. Cook, A. J. Ou, J. C. Leu, Y.-H. Chen, K. Asanović, R. J. Ram, M. A. Popović, and V. M. Stojanović, "Single-chip microprocessor that communicates directly using light," *Nature*, vol. 528, 2015.

[18] L. Stern, B. Desiatov, and et.al., "Nanoscale lightmatter interactions in atomic cladding waveguides," *Nat. Commun.*, vol. 4, p. 1548, mar 2013.

[19] Xuetao Gan, R.-J. Shiue, Yuanda Gao, S. Assefa, J. Hone, and D. Englund, "Controlled LightMatter Interaction in Graphene Electrooptic Devices Using Nanophotonic Cavities and Waveguides," *IEEE Journal of Selected Topics in Quantum Electronics*, vol. 20, pp. 95–105, jan 2014.

[20] J. S. Levy, A. Gondarenko, M. A. Foster, A. C. Turner-Foster, A. L. Gaeta, and M. Lipson, "CMOS-compatible multiple-wavelength oscillator for on-chip optical interconnects," 2010.

[21] T. J. Kippenberg, R. Holzwarth, and S. A. Diddams, "Microresonator-Based Optical Frequency Combs," *Science*, vol. 332, no. 6029, 2011.

[22] L. Razzari, D. Duchesne, and M. Ferrera, "CMOS-compatible integrated optical hyper-parametric oscillator," *Nature . . .*, vol. 4, no. December, pp. 41–45, 2009.

[23] R. Kumar, J. R. Ong, M. Savanier, and S. Mookherjea, "Controlling the spectrum of photons generated on a silicon nanophotonic chip," *Nature Communications*, vol. 5, 2014.

[24] J. W. Silverstone, D. Bonneau, K. Ohira, N. Suzuki, H. Yoshida, N. Iizuka, M. Ezaki, C. M. Natarajan, M. G. Tanner, R. H. Hadfield, V. Zwiller, G. D. Marshall, J. G. Rarity, J. L. O 'brien, and M. G. Thompson, "On-chip quantum interference between silicon photon-pair sources," 2014.

[25] C. Reimer, M. Kues, L. Caspani, B. Wetzel, P. Roztocki, M. Clerici, Y. Jestin, M. Ferrera, M. Peccianti, A. Pasquazi, B. E. Little, S. T. Chu, D. J. Moss, and R. Morandotti, "Cross-polarized photon-pair generation and bi-chromatically pumped optical parametric oscillation on a chip," 2015.

[26] T. van Leest and J. Caro, "Cavity-enhanced optical trapping of bacteria using a silicon photonic crystal," *Lab Chip*, vol. 13, no. 22, p. 4358, 2013.

[27] R. W. Boyd, *Nonlinear Optics Third Edition*. 2007.

[28] J. Leuthold, C. Koos, and W. Freude, "Nonlinear silicon photonics," *Nature Publishing Group*, vol. 4, 2010.

[29] B. Corcoran, C. Monat, C. Grillet, D. J. Moss, B. J. Eggleton, T. P. White, L. O'Faolain, and T. F. Krauss, "Green light emission in silicon through slow-light enhanced third-harmonic generation in photonic-crystal waveguides," *Nature Photonics*, vol. 3, pp. 206–210, apr 2009.

[30] "Apodized waveguide-to-fiber surface grating couplers." https://www.kth.se/en/ees/omskolan/organisation/avdelningar/mst/research/optics/apodized-waveguide-to-fiber-surface-grating-couplers-1.315473.

[31] V. R. Almeida, R. R. Panepucci, and M. Lipson, "Nanotaper for compact mode conversion," *Optics Letters*, vol. 28, p. 1302, aug 2003.

[32] S. McNab, N. Moll, and Y. Vlasov, "Ultra-low loss photonic integrated circuit with membrane-type photonic crystal waveguides," *Optics Express*, vol. 11, p. 2927, nov 2003.

[33] A. Khilo, M. A. Popović, M. Araghchini, and F. X. Kärtner, "Efficient planar fiber-to-chip coupler based on two-stage adiabatic evolution," *Optics Express*, vol. 18, p. 15790, jul 2010.

[34] G. Ren, S. Chen, Y. Cheng, and Y. Zhai, "Study on inverse taper based mode transformer for low loss coupling between silicon wire waveguide and lensed fiber," *Optics Communications*, vol. 284, no. 19, pp. 4782–4788, 2011.

[35] T. Shoji, T. Tsuchizawa, T. Watanabe, K. Yamada, and H. Morita, "Low loss mode size converter from 0.3[micro sign]m square Si wire waveguides to single-mode fibres," *Electronics Letters*, vol. 38, no. 25, p. 1669, 2002.

[36] M. Wood, P. Sun, and R. M. Reano, "Compact cantilever couplers for low-loss fiber coupling to silicon photonic integrated circuits," *Optics Express*, vol. 20, p. 164, jan 2012.

[37] N. Hatori, T. Shimizu, M. Okano, M. Ishizaka, T. Yamamoto, Y. Urino, M. Mori, T. Nakamura, and Y. Arakawa, "A novel spot size convertor for hybrid integrated light sources on photonics-electronics convergence system," in *IEEE Int. Conf. Gr. IV Photonics GFP*, 2012.

[38] P. Cheben, J. H. Schmid, S. Wang, D.-X. Xu, M. Vachon, S. Janz, J. Lapointe, Y. Painchaud, M.-J. Picard, . W. S. Zaoui, A. Kunze, W. Vogel, M. Berroth, J. Butschke, F. Letzkus, J. Burghartz, . R. Halir, P. Cheben, J. H. Schmid, R. Ma, D. Bedard, S. Janz, D.-X. Xu, A. Densmore, and J. Lapointe, "Broadband polarization independent nanophotonic coupler for silicon waveguides with ultra-high efficiency," *Opt. Express*, vol. 2323, no. 17, 2015.

[39] M. Nordström, D. A. Zauner, A. Boisen, and J. Hübner, "Single-mode waveguides with SU-8 polymer core and cladding for MOEMS applications," *J. Light. Technol.*, vol. 25, no. 5, pp. 1284–1289, 2007.

[40] J. Wang, Y. Xuan, C. Lee, B. Niu, L. Liu, G. N. Liu, and M. Qi, "Low-loss and misalignment-tolerant fiber-to-chip edge coupler based on double-tip inverse tapers - IEEE Xplore Document," in *Optical Fiber Communications Conference and Exhibition (OFC)*, Optical Fiber Communications Conference and Exhibition (OFC), 2016, 2016.

[41] O. Aso, M. Tadakuma, and S. Namiki, "Four-Wave Mixing in Optical Fibers and Its Applications," *Furukawa Review*, vol. 19, 2000.

[42] M. A. Foster, A. C. Turner, J. E. Sharping, B. S. Schmidt, M. Lipson, and A. L. Gaeta, "Broad-band optical parametric gain on a silicon photonic chip," *Nature*, vol. 441, pp. 960–963, jun 2006.

[43] R. Salem, M. a. Foster, A. C. Turner, D. F. Geraghty, M. Lipson, and A. L. Gaeta, "Signal regeneration using low-power four-wave mixing on silicon chip," *Nature Photonics*, vol. 2, pp. 35–38, dec 2007.

[44] Gert R. Strobl, *The Physics of Polymers: Concepts for Understanding Their Structures and Behavior*. Berlin, Heidelberg: Springer Berlin Heidelberg, 2007.

[45] L. Alloatti, R. Palmer, S. Diebold, K. P. Pahl, B. Chen, R. Dinu, M. Fournier, J.-M. Fedeli, T. Zwick, W. Freude, C. Koos, and J. Leuthold, "100 GHz Silicon-Organic Hybrid Modulator," *Light Sci Appl*, vol. 3, no. February, p. e173, 2014.

[46] L. Alloatti, D. Korn, R. Palmer, and D. Hillerkuss, "42.7 Gbit/s electro-optic modulator in silicon technology," *Optics ...*, vol. 19, no. 12, pp. 11841–11851, 2011.

[47] C. Koos, P. Vorreau, T. Vallaitis, and P. Dumon, "All-optical high-speed signal processing with silicon-organic hybrid slot waveguides," *Nature Photonics*, vol. 3, no. April, pp. 1–4, 2009.

[48] Y. Li and T. Michinobu, "Multi-coloration of polyurethane derivatives through click postfunctionalization, electrochemical oxidation, and Ag+ ion complexation," *Journal of Materials Chemistry*, vol. 22, no. 19, p. 9513, 2012.

[49] M. Sheik-bahae, A. A. Said, and E. W. Van Stryland, "High-sensitivity, single-beam n_2 measurements," *Opt. Lett.*, vol. 14, p. 955, sep 1989.

[50] M. Sheik-Bahae, A. A. Said, T.-H. Wei, D. J. Hagan, and E. W. Van Stryland, "Sensitive Measurement of Optical Nonlinearities Using a Single Beam," *IEEE JOURNAL OF QUANTUM ELECTRONICS*, vol. 26, no. 4, 1990.

[51] "Refractive indx of glass." `http://refractiveindex.info/?shelf=glass&book=BK7&page=SCHOTT`.

[52] D. J. Moss, R. Morandotti, A. L. Gaeta, and M. Lipson, "New CMOS-compatible platforms based on silicon nitride and Hydex for nonlinear optics," *Nat. Photonics*, vol. 7, pp. 597–607, jul 2013.

[53] J. W. Silverstone, D. Bonneau, J. L. O 'brien, and M. G. Thompson, "Silicon Quantum Photonics," *IEEE JOURNAL OF SELECTED TOPICS IN QUANTUM ELECTRONICS*, vol. 22, no. 6, 2016.

[54] S. Xiao, M. H. Khan, H. Shen, and M. Qi, "Compact silicon microring resonators with ultra-low propagation loss in the C band," *Optics Express*, vol. 15, no. 22, p. 14467, 2007.

[55] "Caltech Intermediate Format." `http://www.rulabinsky.com/cavd/text/chapb.html`.

[56] "GDS II Format." `http://www.rulabinsky.com/cavd/text/chapc.html`.

[57] E. Yablonovitch, "Inhibited Spontaneous Emission in Solid-State Physics and Electronics," *Physical Review Letters*, vol. 58, pp. 2059–2062, may 1987.

[58] J. D. Joannopoulos, P. R. Villeneuve, and S. Fan, "Photonic crystals: putting a new twist on light," *Nature*, vol. 386, pp. 143–149, mar 1997.

[59] A. J. Turberfield, M. Campbell, D. N. Sharp, M. T. Harrison, and R. G. Denning, "Fabrication of photonic crystals for the visible spectrum by holographic lithography," *Nature*, vol. 404, pp. 53–56, mar 2000.

[60] C. M. Soukoulis, "The history and a review of the modelling and fabrication of photonic crystals," *Nanotechnology*, vol. 13, p. 335, jun 2002.

[61] J. D. Joannopoulos, S. G. Johnson, J. N. Winn, and R. D. Meade, *Photonic Crystals: Molding the Flow of Light*. Princeton University Press, 2008.

[62] S. Y. Lin, J. G. Fleming, D. L. Hetherington, B. K. Smith, R. Biswas, K. M. Ho, M. M. Sigalas, W. Zubrzycki, S. R. Kurtz, and J. Bur, "A three-dimensional photonic crystal operating at infrared wavelengths," *Nature*, vol. 394, pp. 251–253, jul 1998.

[63] J. G. Fleming and S.-Y. Lin, "Three-dimensional photonic crystal with a stop band from 135 to 195???m," *Optics Letters*, vol. 24, p. 49, jan 1999.

[64] T. Katsuyama, K. Hosomi, H. Yamada, S. Goto, K. Aoki, and Y. Arakawa, "Woodpile photonic crystals composed of air columns," *Photonics and Nanostructures - Fundamentals and Applications*, vol. 4, no. 1, pp. 54–58, 2006.

[65] L. Wang, S. Zhang, Q. Wang, J. Chen, W. Jiang, and R. T. Chen, "Fabrication of three-dimensional (3D) woodpile structure photonic crystal with layer by layer e-beam lithography," *Applied Physics A*, vol. 95, pp. 329–334, may 2009.

[66] C. Mcguinness, R. L. Byer, E. Colby, B. M. Cowan, R. J. England, R. J. Noble, T. Plettner, C. M. Sears, R. Siemann, J. Spencer, and D. Waltz, "Woodpile Structure Fabrication for Photonic Crystal Laser Acceleration," 2008.

[67] L. T. Varghese, L. Fan, Y. Xuan, L. Zhao, and M. Qi, "3-D Woodpile Photonic Crystal Fabrication Using a One Step Scaffold Inversion Method," in *Integrated Photonics Research, Silicon and Nanophotonics and Photonics in Switching*, (Washington, D.C.), p. IWE5, OSA, 2010.

[68] S. Fan, P. R. Villeneuve, R. D. Meade, and J. D. Joannopoulos, "Design of three-dimensional photonic crystals at submicron lengthscales," *Applied Physics Letters*, vol. 65, no. 11, p. 1466, 1994.

[69] S. G. Johnson and J. D. Joannopoulos, "Three-dimensionally periodic dielectric layered structure with omnidirectional photonic band gap," *Applied Physics Letters*, vol. 77, no. 22, p. 3490, 2000.

[70] M. Qi, E. Lidorikis, P. T. Rakich, S. G. Johnson, J. D. Joannopoulos, E. P. Ippen, and H. I. Smith, "A three-dimensional optical photonic crystal with designed point defects," *Nature*, vol. 429, pp. 538–542, jun 2004.

[71] W. Bogaerts, P. De Heyn, T. Van Vaerenbergh, K. De Vos, S. Kumar Selvaraja, T. Claes, P. Dumon, P. Bienstman, D. Van Thourhout, and R. Baets, "Silicon microring resonators," *Laser & Photonics Reviews*, vol. 6, pp. 47–73, jan 2012.

[72] B. E. Little, S. T. Chu, H. A. Haus, J. Foresi, and J.-P. Laine, "Microring Resonator Channel Dropping Filters," *JOURNAL OF LIGHTWAVE TECHNOLOGY*, vol. 15, no. 6, 1997.

[73] T. Makino, T. Gotoh, R. Hasegawa, T. Arakawa, and Y. Kokubun, "Microring resonator wavelength tunable filter using five-layer asymmetric coupled quantum well," *Journal of Lightwave Technology*, 2011.

[74] Y. Ding, M. Pu, L. Liu, J. Xu, C. Peucheret, X. Zhang, D. Huang, and H. Ou, "Bandwidth and wavelength-tunable optical bandpass filter based on silicon microring-MZI structure," *Optics Express*, vol. 19, p. 6462, mar 2011.

[75] K. De Vos, I. Bartolozzi, E. Schacht, P. Bienstman, and R. Baets, "Silicon-on-Insulator microring resonator for sensitive and label-free biosensing," *Optics Express*, vol. 15, no. 12, p. 7610, 2007.

[76] A. Ramachandran, S. Wang, J. Clarke, S. Ja, D. Goad, L. Wald, E. Flood, E. Knobbe, J. Hryniewicz, S. Chu, D. Gill, W. Chen, O. King, and B. Little, "A universal biosensing platform based on optical micro-ring resonators," *Biosensors and Bioelectronics*, vol. 23, no. 7, pp. 939–944, 2008.

[77] J. T. Kindt and R. C. Bailey, "Biomolecular analysis with microring resonators: applications in multiplexed diagnostics and interaction screening.," *Current opinion in chemical biology*, vol. 17, pp. 818–26, oct 2013.

[78] V. R. Almeida, C. A. Barrios, R. R. Panepucci, and M. Lipson, "All-optical control of light on a silicon chip," *Nature*, vol. 431, pp. 1081–1084, oct 2004.

[79] Q. Xu and M. Lipson, "All-optical logic based on silicon micro-ring resonators," *Optics Express*, vol. 15, no. 3, p. 924, 2007.

[80] D.-X. Xu, A. Delâge, R. McKinnon, M. Vachon, R. Ma, J. Lapointe, A. Densmore, P. Cheben, S. Janz, and J. H. Schmid, "Archimedean spiral cavity ring resonators in silicon as ultra-compact optical comb filters," *Optics Express*, vol. 18, p. 1937, feb 2010.

[81] M. Amersfoort, *Phased-array wavelength demultiplexers and their integration with photodetectors*. PhD thesis, Delft University of Technology, 1994.

[82] M. Smit and C. Van Dam, "PHASAR-based WDM-devices: Principles, design and applications," *IEEE Journal of Selected Topics in Quantum Electronics*, vol. 2, pp. 236–250, jun 1996.

[83] J. F. Bauters, J. R. Adleman, M. J. R. Heck, and J. E. Bowers, "Design and characterization of arrayed waveguide gratings using ultra-low loss Si3N4 waveguides," *Applied Physics A*, vol. 116, pp. 427–432, aug 2014.

[84] R. Ji, L. Yang, L. Zhang, Y. Tian, J. Ding, H. Chen, Y. Lu, P. Zhou, and W. Zhu, "Microring-resonator-based four-port optical router for photonic networks-on-chip," *Optics Express*, vol. 19, p. 18945, sep 2011.

[85] R. Ji, L. Yang, L. Zhang, Y. Tian, J. Ding, H. Chen, Y. Lu, P. Zhou, and W. Zhu, "Five-port optical router for photonic networks-on-chip," *Optics Express*, vol. 19, p. 20258, oct 2011.

[86] T. Hu, H. Qiu, P. Yu, C. Qiu, W. Wang, X. Jiang, M. Yang, and J. Yang, "Wavelength-selective 44 nonblocking silicon optical router for networks-on-chip," *Optics Letters*, vol. 36, p. 4710, dec 2011.

[87] A. Bianco, D. Cuda, M. Garrich, G. G. Castillo, R. Gaudino, and P. Giaccone, "Optical Interconnection Networks Based on Microring Resonators," *Journal of Optical Communications and Networking*, vol. 4, p. 546, jul 2012.

[88] R. Min, R. Ji, Q. Chen, L. Zhang, and L. Yang, "A Universal Method for Constructing N-Port Nonblocking Optical Router for Photonic Networks-On-Chip," *Journal of Lightwave Technology, Vol. 30, Issue 23, pp. 3736-3741*, vol. 30, no. 23, pp. 3736–3741, 2012.

[89] X. Xue, Y. Xuan, C. Wang, P.-H. Wang, Y. Liu, B. Niu, D. E. Leaird, M. Qi, and A. M. Weiner, "Thermal tuning of Kerr frequency combs in silicon nitride microring resonators," *Optics Express*, vol. 24, p. 687, jan 2016.

[90] H. Jayatilleka, K. Murray, M. Á. Guillén-Torres, M. Caverley, R. Hu, N. A. F. Jaeger, L. Chrostowski, and S. Shekhar, "Wavelength tuning and stabilization of microring-based filters using silicon in-resonator photoconductive heaters," *Optics Express*, vol. 23, p. 25084, sep 2015.

[91] J. Chou, Y. Han, and B. Jalali, "Adaptive RF-Photonic Arbitrary Waveform Generator," *IEEE PHOTONICS TECHNOLOGY LETTERS*, vol. 15, no. 4, 2003.

[92] A. Rashidinejad, D. E. Leaird, and A. M. Weiner, "Ultrabroadband radio-frequency arbitrary waveform generation with high-speed phase and amplitude modulation capability," *Optics Express*, vol. 23, p. 12265, may 2015.

[93] A. M. Weiner, "FEMTOSECOND OPTICAL PULSE SHAPING AND PROCESSING," *Prog. Quantum Electron*, vol. 19, pp. 161–237, 1995.

[94] A. M. Weiner, "Ultrafast optical pulse shaping: A tutorial review," *OPTICS*, vol. 284, pp. 3669–3692, 2011.

[95] K. Takiguchi, K. Okamoto, T. Kominato, H. Takahashi, and T. Shibata, "Flexible pulse waveform generation using silica-waveguide-based spectrum synthesis circuit," *Electron. Lett.*, 2004.

[96] M. H. Khan, H. Shen, Y. Xuan, L. Zhao, S. Xiao, D. E. Leaird, A. M. Weiner, and M. Qi, "Ultrabroad-bandwidth arbitrary radiofrequency waveform generation with a silicon photonic chip-based spectral shaper," *Nature Photonics*, vol. 4, pp. 117–122, feb 2010.

[97] "Wide-bandwidth continuously tunable optical delay line using silicon microring resonators," *Optics Express*, vol. 18, p. 26525, dec 2010.

[98] "Continuously tunable slow-light device consisting of heater-controlled silicon microring array," *Optics Express*, vol. 19, p. 13557, jul 2011.

[99] J. Wang, H. Shen, L. Fan, R. Wu, B. Niu, L. T. Varghese, Y. Xuan, D. E. Leaird, X. Wang, F. Gan, A. M. Weiner, and M. Qi, "Reconfigurable radio-frequency arbitrary waveforms synthesized in a silicon photonic chip," *Nature Communications*, vol. 6, p. 5957, jan 2015.

[100] L. Fan, J. Wang, L. T. Varghese, H. Shen, B. Niu, Y. Xuan, A. M. Weiner, and M. Qi, "An All-Silicon Passive Optical Diode," *Science*, vol. 335, no. 6067, 2012.

[101] L. Fan, L. T. Varghese, Y. Xuan, J. Wang, B. Niu, and M. Qi, "Direct fabrication of silicon photonic devices on a flexible platform and its application for strain sensing," *Optics Express*, vol. 20, p. 20564, aug 2012.

[102] J. Wang, J. Ouyang, L. T. Varghese, L. Fan, Y. Xuan, and M. Qi, "A Hollow-Core Optical Cavity Built in a Three-Layer Silicon Photonic Crystal," *Advanced Optical Materials*, vol. 1, pp. 740–746, oct 2013.

VITA

VITA

Ben Niu was born in Xi'an China in 1986. He graduated from the high school affiliated with Xi'an Jiaotong University in 2004. In the same year he enrolled in the School of Electronics Engineering and Computer Science (EECS) at Beijing University (also known as Peking University). He majored in the field of microelectronics and obtained his Bachelor of Science degree in 2008. Subsequently he joined Professor Minghao Qi's group at Purdue University and researched in the field of on-chip silicon photonics as a PhD graduate student. During his PhD study, he also worked in Shanghai Institute of Microsystems and Information Technology (SIMIT), Chinese Academy of Science in a collaborated project from 2012 to 2013. In addition, he also worked with Futurewei Technologies (Huawei USA) in a research project from 2014 to 2016. He will obtain his PhD degree in 2016.